



# Polarisation du J/psi en collisions pp a $\sqrt{s} = 7$ TeV avec le spectromètre à muons d'ALICE au LHC

Livio Bianchi

## ► To cite this version:

Livio Bianchi. Polarisation du J/psi en collisions pp a  $\sqrt{s} = 7$  TeV avec le spectromètre à muons d'ALICE au LHC. Other [cond-mat.other]. Université Paris Sud - Paris XI; Università di Torino, 2012. English. NNT : 2012PA112037 . tel-00688321

**HAL Id: tel-00688321**

**<https://theses.hal.science/tel-00688321>**

Submitted on 17 Apr 2012

**HAL** is a multi-disciplinary open access archive for the deposit and dissemination of scientific research documents, whether they are published or not. The documents may come from teaching and research institutions in France or abroad, or from public or private research centers.

L'archive ouverte pluridisciplinaire **HAL**, est destinée au dépôt et à la diffusion de documents scientifiques de niveau recherche, publiés ou non, émanant des établissements d'enseignement et de recherche français ou étrangers, des laboratoires publics ou privés.



UNIVERSITÀ DEGLI STUDI DI TORINO  
DOTTORATO DI RICERCA IN SCIENZA E ALTA TEC-  
NOLOGIA - CICLO XXIV - SETTORE SCIENTIFICO-  
DISCIPLINARE DI AFFERENZA: FIS/04



UNIVERSITÉ PARIS-SUD 11  
ÉCOLE DOCTORALE 534 MIPEGE - MODÉLISATION  
ET INSTRUMENTATION EN PHYSIQUE, ÉNERGIES,  
GÉOSCIENCES ET ENVIRONNEMENT

---

Thesis submitted for the degree of  
Doctor of Philosophy in Physics

# $J/\psi$ polarization in $pp$ collisions at $\sqrt{s} = 7$ TeV with the ALICE muon spectrometer at the LHC

Defended on March 6th, 2012

**Candidate:**

Livio Bianchi

**Director:**

Ermanno Vercellin

**Co-Director:**

Bruno Espagnon

**Supervisor:**

Enrico Scomparin

**Co-Supervisor:**

Cynthia Hadjidakis

**External reviewers:**

Federico Antinori

François Vazeille



# Contents

<b>Introduction</b>	<b>1</b>
<b>1 Heavy quarkonia</b>	<b>5</b>
1.1 Discovery: from the $J/\psi$ to the $\chi_b(3P)$ . . . . .	5
1.2 $\psi$ and $\Upsilon$ states: decay and feed-down . . . . .	12
1.3 Theoretical description of quarkonia states . . . . .	15
1.4 Theoretical description of quarkonium production . . . . .	18
1.5 Experimental results on quarkonium production before the LHC era . .	24
1.6 The LHC era . . . . .	30
1.7 Recent theoretical results on quarkonium production . . . . .	38
1.8 Quarkonium in heavy ions collisions . . . . .	40
<b>2 Quarkonium polarization: theoretical concepts and experimental results</b>	<b>49</b>
2.1 Vector particle's polarization . . . . .	50
2.2 Two-body decay: angular distribution . . . . .	51
2.3 Reference frames . . . . .	56
2.4 Kinematical constraints . . . . .	57
2.5 Invariant quantities . . . . .	58
2.6 Quarkonium polarization: experimental issues . . . . .	60
2.7 Experimental results on quarkonium polarization and comparison with theory . . . . .	62
<b>3 The ALICE apparatus at the LHC</b>	<b>73</b>
3.1 The Large Hadron Collider at CERN . . . . .	74
3.2 ALICE layout . . . . .	75
3.3 The Forward Muon Spectrometer . . . . .	81

## CONTENTS

---

3.4	ALICE trigger and data acquisition . . . . .	89
3.5	The ALICE offline framework: AliRoot . . . . .	89
<b>4</b>	<b>J/<math>\psi</math> polarization study</b>	<b>93</b>
4.1	Analysis Strategy . . . . .	94
4.2	Data sample and run selection . . . . .	95
4.3	Analysis cuts . . . . .	98
4.4	Signal Extraction . . . . .	99
4.5	Acceptance and Efficiency correction: iterative procedure . . . . .	103
4.6	Fits to the $A \times \epsilon$ corrected spectra . . . . .	108
4.7	Systematic uncertainties . . . . .	109
4.8	Results . . . . .	112
4.9	The role of the $\lambda_{\theta\phi}$ parameter . . . . .	115
4.10	The role of the non-prompt component . . . . .	117
	<b>Conclusions</b>	<b>121</b>
	<b>A Analysis dimensionality and acceptance bias</b>	<b>123</b>
	<b>B Invariant mass Fits</b>	<b>125</b>
	<b>C Fits to the corrected spectra</b>	<b>133</b>
	<b>D Checks on the analysis procedure</b>	<b>135</b>
	<b>Acknowledgments</b>	<b>141</b>

# Introduction

The Standard Model of particle physics is the theory which describes elementary particle interactions and can be divided in electro-weak theory and quantum chromodynamics (QCD), the theory of strong interactions. The main feature of QCD (asymptotic freedom) allows accurate calculations only for processes occurring at very high momentum scales, while the description of hadron states is more difficult since it typically involves long distance interactions, where a perturbative approach is no longer valid. A typical example of this difficulty is the study of the production of particles known as heavy quarkonia.

Heavy quarkonia are meson states composed by a  $c$  or a  $b$  quark and its corresponding anti-quark and are also known as “charmonium” and “bottomonium” respectively. The history of these states, briefly skimmed through in the first part of Chapter 1, is tightly bound to the progress of theory in describing elementary particle interactions. The first appearance of the  $J/\psi$  in the experimental apparatus in 1974 supported the “fourth quark hypothesis”, first proposed by Bjorken and Glashow ten years before, while the  $\Upsilon$  discovery (1977) made the case of a third family of quarks.

Considering that  $c$  and  $b$  are heavy quarks, the production of charmonia and bottomonia states involves different energy scales: the formation of the quark-antiquark pair is a hard process and can be reliably described through perturbative QCD calculations, but the dynamics of the bound state formation and evolution are intrinsically non-relativistic and they involve soft energy scales. For this reason no full-QCD description of quarkonium production can be carried out and many theoretical models have been developed in the last forty years. Their ability in describing experimental observables reflects the level of understanding of QCD in its soft regime, which is crucial for the theoretical explanation of hadron properties.

The basic assumption of all these models is that the perturbative and the non-

perturbative effects involved in the quarkonium formation can be factorized, and the general framework for this factorization is provided by the nonrelativistic QCD (NRQCD), which is an effective field theory that reproduces QCD in its hard scale limit. The success of this theory in reproducing the  $p_t$  differential cross section for the production of many quarkonia states at the Tevatron led to the impression, in the nineties, that the puzzle of quarkonium production could be considered as solved. NRQCD at the leading order (LO) accuracy was then used to predict the behaviour of many other observables and, among them, the degree of polarization of the produced quarkonia was found to be the golden one since an unambiguous observation was expected: full transverse polarization at high  $p_t$ .

The results obtained by the CDF experiment on this observable for  $J/\psi$  hadroproduction ruled out the LO NRQCD prediction: not only the expected transverse polarization at high  $p_t$  was not observed, but also the trend with  $p_t$  observed in real data was opposite with respect to the theoretical curve.

Still today no theoretical approach is able to describe at the same time Tevatron results on cross section and polarization for heavy quarkonia. In this situation an analysis of polarization at the LHC energy is clearly extremely interesting and will be the main subject of this work.

From the experimental point of view the polarization of a vector meson is measured through the analysis of the angular distribution of its decay products. This kind of analysis is particularly statistics-demanding and detector acceptance issues can play a crucial role. Many aspects of this topic are discussed in Chapter 2.

ALICE, extensively described in Chapter 3, is the dedicated heavy-ion experiment at the LHC and its main goal is the study of the hot, extended and deconfined system of partons (Quark Gluon Plasma - QGP) that is formed in heavy ion collisions. Furthermore, the study of  $pp$  collisions allows to obtain reference data for QGP-related analysis, but, as will be done in this work, also to investigate open issues in elementary particle physics.

Thanks to its muon and electron detection capabilities, ALICE can measure quarkonium production over a large rapidity range and down to  $p_t = 0$  in both  $pp$  and  $PbPb$  collisions. During its first two years of data taking, ALICE has published results on  $J/\psi$  production in  $pp$  collisions at  $\sqrt{s} = 7$  TeV and  $\sqrt{s} = 2.76$  TeV, and on  $J/\psi$  suppression in  $PbPb$  collisions at  $\sqrt{s} = 2.76$  TeV/nucleon.

In this thesis the measurement of the polarization of inclusively produced  $J/\psi$  in  $pp$  collisions at  $\sqrt{s} = 7$  TeV is presented in Chapter 4. This analysis was carried out at forward rapidity ( $-4 < y < -2.5$ ), exploiting the muonic  $J/\psi$  decay channel and profiting of data collected during 2010. The future implementation of trigger strategies dedicated to the detection of rare events at midrapidity, in the  $e^+e^-$  decay channel, will probably allow to perform the same measurement for  $|y| < 0.9$ .

The results presented in this thesis represent the first measurement of  $J/\psi$  polarization at the LHC energy and they offer the possibility to test the theoretical models in a more than three times higher energy regime with respect to Tevatron. The comparison between the measured experimental points and some recent theoretical calculations at the NLO accuracy level is also shown at the end of Chapter 4.





# Chapter 1

## Heavy quarkonia

Heavy quarkonia are  $c\bar{c}$  and  $b\bar{b}$  bound states and represent an important testing ground for many aspects of Quantum Chromo-Dynamics (QCD). The history of these states is tightly bound to the progress of theory in describing elementary particle interactions. In this chapter a short description of the historical happenings that led to the discovery of these states is given in Section 1.1, while Section 1.2 is devoted to a brief discussion on their peculiarities from the experimental point of view. In Section 1.3 and 1.4 some details on theoretical aspects that are useful to describe the characteristics and the production rates of such resonances are given. An extensive review of the experimental results on this topic before (Section 1.5) and after (Section 1.6) the LHC startup is then carried out, while very recent theoretical developments are revised in Section 1.7. In the last section (1.8) the importance of heavy quarkonia in the study of the hot and dense matter produced in nucleus-nucleus collisions is briefly summarized.

### 1.1 Discovery: from the $J/\psi$ to the $\chi_b(3P)$

#### 1.1.1 The beginnings

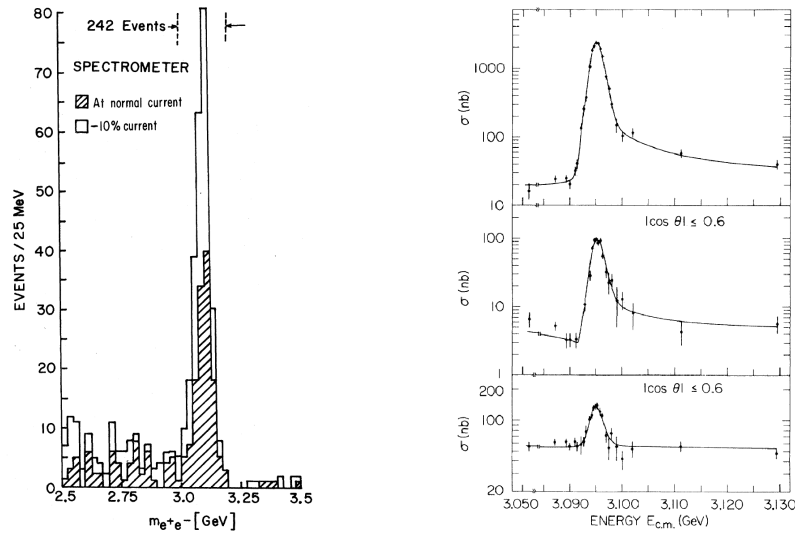
The history of heavy quarkonia dates back to November 1974, when two different groups discovered an unexpected bump corresponding to a mass of roughly  $3.1 \text{ GeV}/c^2$ . Ting *et al.* [1] were studying  $30 \text{ GeV}/c$  protons, accelerated by the AGS at BNL<sup>1</sup>, colliding on a fixed target and they observed a sharp peak in the electron-positron invariant mass spectrum, to which they gave the name “J”. The peak is shown in Figure 1.1(a). Richter *et al.* [2] found the same peak in  $e^+e^-$  annihilation at the electron-positron

---

<sup>1</sup>Alternating Gradient Synchrotron at Brookhaven National Laboratory

storage ring SPEAR at SLAC<sup>2</sup> (see Figure 1.1(b)). The center of mass energy in this case was tunable and the observed final states were many, such as  $e^+e^-$ ,  $\mu^+\mu^-$ ,  $\pi^+\pi^-$  etc. In this case the name “ $\psi$ ” was motivated by the topology of the  $e^+e^- \rightarrow \pi^+\pi^-$  decay.

In the following weeks the Frascati group (Bacci *et al.* [3]) confirmed the presence of



(a) Electron-positron invariant mass distribution from 20 GeV/c protons on fixed target [1]

(b) Pair particle production from  $e^+e^-$  collisions: hadrons (top),  $\pi^+\pi^-/\mu^+\mu^-/K^+K^-$  (middle),  $e^+e^-$  (bottom) [2]

Figure 1.1: First observations of the  $J/\psi$  peak.

this new particle and ten days later Richter’s group discovered another resonant state, at higher mass, which was called  $\psi'$  (also called  $\psi(2S)$ ).

In the two years after the discovery there was a very large echo in the scientific community and many experimental efforts were prompted in order to extract the basic characteristics of the 3.1 GeV/ $c^2$  particle. Further studies had revealed that the resonance had the same quantum numbers of the photon ( $1^{--}$ ) and, from the fact that the ratio

$$R = \frac{\text{cross section } e^+e^- \rightarrow \text{hadrons}}{\text{cross section } e^+e^- \rightarrow \mu^+\mu^-}$$

was much larger on-resonance than off, it was clear that the particle had a direct hadronic decay and it was therefore classified as an hadron. During 1975 and 1976

<sup>2</sup>Stanford Positron Electron Asymmetric Rings at the Stanford Linear Accelerator Center

other resonances with quantum numbers different from those of the photon were discovered (C-parity=+1) in the mass region between 3.4 and 3.6 GeV/ $c^2$ . The first to observe them was the DASP collaboration at DESY<sup>3</sup> [4] and the confirmation came again from SPEAR.

In 1976 Ting and Richter were awarded the Nobel prize for their first discovery and the name  $J/\psi$  was assigned to the particle, using a double name to pay tribute to the two simultaneous observations.

The reason for such a high interest in the discovery of the  $J/\psi$  can be understood

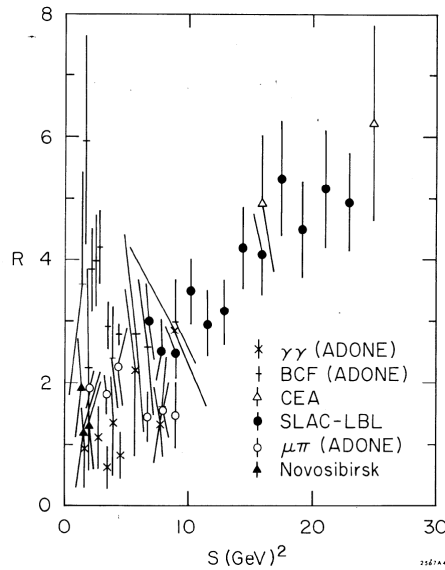


Figure 1.2: Experimental status on the  $R$  ratio study as of July 1974 (from [5]).

by thinking to the overall knowledge of particle physics at that time and by looking to the  $R$  ratio, shown in Figure 1.2, presented by Richter [5] at the XVII International Conference in High Energy Physics, held in London during July 1974.

In the framework of the Gell-Mann-Zweig quark model with three quarks, first proposed in 1963, a plateau in the  $R$  plot was expected with a value of  $2/3$  (or 2 if the quark was considered as coloured) and was not evident with the available data. Still the model was useful to interpret the zoo of light hadrons and the existence of a fourth quark, first proposed by Bjorken and Glashow in 1964 [6], was found to be necessary from the theoretical point of view (following the work of Glashow, Iliopoulos and Maiani [7]) in order to cancel the anomaly in the weak decays. The proposed name of this

<sup>3</sup>Deutsches Elektronen-SYnchrotron - Hamburg

fourth expected quark was “charm” ( $c$ ) and the electric charge had to be  $2/3$ . The  $J/\psi$  state began to be thought as the lightest  $c\bar{c}$  system and the term “charmonium” was introduced already in 1975, even if this interpretation was not obvious: the presence of the new quark would have led to a plateau in the  $R$  ratio distribution at the value of  $10/3$ , but this, again, was not evident in Figure 1.2. When, in 1976, the discovery of explicit<sup>4</sup> charmed mesons (the  $D$  family) [8] and barions (the  $\Lambda_c$ ) [9] was announced, the existence of the fourth quark was proved and the importance of the  $J/\psi$  discovery was then clear.

The history of heavy quarkonium was far from being at its twilight. The discovery at SLAC of a new lepton, the  $\tau$ , in 1975 [10] opened the doors to a new lepton family, the third one. As in the past, a third family of quarks was hypothesized and in 1977 a resonance similar to the  $J/\psi$  appeared in the dimuon mass spectrum at  $9.5 \text{ GeV}/c^2$  and it was called  $\Upsilon$  by the Herb *et al.* group which discovered it at FNAL<sup>5</sup> [11]. This particle was interpreted as the lowest mass vector  $b\bar{b}$  bound state, where  $b$ , standing for *bottom*, was the proposed name for the fifth quark. Again the first excited state (the  $\Upsilon(2S)$ ) was discovered in a short delay [12] and, just a bit after, also the  $\Upsilon(3S)$  was observed [13]. Explicit bottom was then observed by the CLEO detector at CESR<sup>6</sup> in the  $B$  meson [14] and by CERN in the  $\Lambda_b$  baryon [15].

The last quark, the *top* ( $t$ ), was discovered only in 1994 by the CDF collaboration at the Tevatron (Fermilab) [16]: due to its very short lifetime this quark doesn’t bind in a  $t\bar{t}$  system, so no *topponium* can be formed and the family of heavy quarkonia is closed to charmonia and bottomonia resonances.

### 1.1.2 Newer and newer states

The discoveries of the end of the seventies prompted many experimental efforts, aimed to new discoveries and to the determination of the characteristics of the already observed resonances. The first attempt was to scan the  $e^+e^-$  annihilation energy to search for higher mass  $\psi$  and  $\Upsilon$  resonances: the study of the  $R$  ratio and of the open-flavour final states lead to the discovery, already in the late seventies and beginning of eighties, of  $\psi(3770)$ ,  $\psi(4040)$ ,  $\psi(4160)$ ,  $\psi(4415)$ ,  $\Upsilon(4S)$ ,  $\Upsilon(10860)$  and  $\Upsilon(11020)$  (all above

---

<sup>4</sup>“explicit” refers to the fact that in these particles the charm quantum number is different from zero, in contrast with what happens for the “hidden” charm ( $c\bar{c}$  states).

<sup>5</sup>Fermi National Accelerator Laboratory, also called Fermilab

<sup>6</sup>Cornell Electron Storage Ring - Cornell University (New York)

threshold for open heavy flavour decay). All these observations were possible thanks to the new generation of experiments built just after the first discoveries and devoted to the charm and bottom physics (e.g. CLEO and CUSB at CESR).

The analysis of the radiative decays of the  $\psi$  and  $\Upsilon$  resonances was also fruitful since it led to the discovery of the 1P states ( $\chi_c$  and  $\chi_b$  families) and of the lightest  $c\bar{c}$  resonance (the  $\eta_c(1S)$ ), again all in the first half of the eighties.

A new improvement to the discovery of charmonia and bottomonia was given by the startup of the so-called B-factories,  $e^+e^-$  colliders (such as KEKB and PEP) devoted to the study of B-physics and to the CP-violation topic. The experiments running from 1998 to 2010 at these facilities, namely Belle and Babar, were able to collect a huge amount of events, very useful to perform delicate analysis, which allowed for the discovery of the  $\chi_{c2}(2P)$  (Belle - 2006) and of the  $\eta_b(1S)$  (BaBar - 2008), thus ending the long search of the lowest-mass  $b\bar{b}$  system.

In Table 1.1 all the observed “conventional” heavy quarkonia states are shown, where conventional means that all of them were theoretically expected and understood.

Table 1.1: Charmonia and bottomonia “conventional” states under the open-heavy flavour decay mass threshold. The  $\chi_b(3P)$  is not reported since needs experimental confirmation after ATLAS’ first observation (see Section 1.1.4).

$c\bar{c}$			$b\bar{b}$		
Name	Mass (MeV)	$J^{PC}$	Name	Mass (MeV)	$J^{PC}$
$\eta_c(1S)$	$2980.3 \pm 1.2$	$0^{-+}$	$\eta_b(1S)$	$9390.9 \pm 2.8$	$0^{-+}$
$J/\psi(1S)$	$3096.916 \pm 0.011$	$1^{--}$	$\Upsilon(1S)$	$9460.30 \pm 0.26$	$1^{--}$
$\chi_{c0}(1P)$	$3414.75 \pm 0.31$	$0^{++}$	$\chi_{b0}(1P)$	$9859.44 \pm 0.42 \pm 0.31$	$0^{++}$
$\chi_{c1}(1P)$	$3510.66 \pm 0.07$	$1^{++}$	$\chi_{b1}(1P)$	$9892.78 \pm 0.26 \pm 0.31$	$1^{++}$
$h_c(1P)$	$3525.41 \pm 0.16$	$1^{+-}$			
$\chi_{c2}(1P)$	$3556.20 \pm 0.09$	$2^{++}$	$\chi_{b2}(1P)$	$9912.21 \pm 0.26 \pm 0.31$	$2^{++}$
$\eta_c(2S)$	$3637 \pm 4$	$0^{-+}$			
$\psi(2S)$	$3686.09 \pm 0.04$	$1^{--}$	$\Upsilon(2S)$	$10023.26 \pm 0.31$	$1^{--}$
			$\Upsilon(1D)$	$10163.7 \pm 1.4$	$2^{--}$
			$\chi_{b0}(2P)$	$10232.5 \pm 0.4 \pm 0.5$	$0^{++}$
			$\chi_{b1}(2P)$	$10255.46 \pm 0.22 \pm 0.50$	$1^{++}$
			$\chi_{b2}(2P)$	$10268.65 \pm 0.22 \pm 0.50$	$2^{++}$
			$\Upsilon(3S)$	$10355.2 \pm 0.5$	$1^{--}$

### 1.1.3 From 2003 on: a plethora of new unexpected states

In fall 2003, while studying  $B^+ \rightarrow K^+ \pi^+ \pi^- J/\psi$ , the Belle collaboration discovered [17] an unexpected enhancement in the  $\pi^+ \pi^- J/\psi$  invariant mass spectrum near 3872 MeV/ $c^2$ : it was denoted as X(3872). This evidence of the X in B-decays was later confirmed by BaBar. The  $X \rightarrow \pi^+ \pi^- J/\psi$  decay was also observed in  $p\bar{p}$  collisions at the Tevatron by both CDF and D0 and, more recently, in  $pp$  collisions at the LHC by LHCb and CMS.

Table 1.2: New unexpected states in the  $c\bar{c}$  and  $b\bar{b}$  regions, ordered by mass. *Year* is the year of first observation by the bolded experiment; *Status* is OK for resonances observed by many experiments, NC for still not confirmed states. From [18].

Name	Mass	$J^{PC}$	Year	Experiment	Status
X(3872)	$3871.52 \pm 0.20$	$1^{++}/2^{-+}$	2003	<b>Belle</b> , BaBar, CDF, D0	OK
X(3915)	$3915.6 \pm 3.1$	$0/2^{?+}$	2004	<b>Belle</b> , BaBar	OK
X(3940)	$3942^{+9}_{-8}$	$?^{?+}$	2007	<b>Belle</b>	NC
G(3900)	$3943 \pm 21$	$1^{--}$	2007	<b>BaBar</b> , Belle	OK
Y(4008)	$3942^{+121}_{-49}$	$1^{--}$	2007	<b>Belle</b>	NC
Z <sub>1</sub> (4050)	$4051^{+24}_{-43}$	$?$	2008	<b>Belle</b>	NC
Y(4140)	$4143.4 \pm 3.0$	$?^{?+}$	2009	<b>CDF</b>	NC
X(4160)	$4156^{+29}_{-25}$	$?^{?+}$	2007	<b>Belle</b>	NC
Z <sub>2</sub> (4250) <sup>+</sup>	$4248^{+185}_{-45}$	$?$	2008	<b>Belle</b>	NC
Y(4260)	$4263 \pm 5$	$1^{--}$	2005	<b>BaBar</b> , CLEO, Belle	OK
Y(4274)	$4274.4^{+8.4}_{-6.7}$	$?^{?+}$	2010	<b>CDF</b>	NC
X(4350)	$4350.6^{+4.6}_{-5.1}$	$0/2^{++}$	2009	<b>Belle</b>	NC
Y(4360)	$4353 \pm 11$	$1^{--}$	2007	<b>BaBar</b> , Belle	OK
Z(4430) <sup>+</sup>	$4443^{+24}_{-18}$	$?$	2007	<b>Belle</b>	NC
X(4630)	$4634^{+9}_{-11}$	$1^{--}$	2007	<b>Belle</b>	NC
Y(4660)	$4664 \pm 12$	$1^{--}$	2007	<b>Belle</b>	NC
Y <sub>b</sub> (10888)	$10888.4 \pm 3.0$	$1^{--}$	2010	<b>Belle</b>	NC

Deeper studies devoted to the determination of the quantum numbers of such a resonance are pushing for a  $1^{++}$  state, with decay properties which do not comfortably fit those of any plausible charmonium state. Prominent decays to  $D^{*0} \bar{D}^0$  and proximity

to the  $D^{*0}\bar{D}^0$  mass threshold naturally lead to models which interpret the  $X(3872)$  as a weakly bound molecule of a  $D^{*0}$  and a  $\bar{D}^0$ . Other models try to explain the  $X$  existence as a tightly bound diquark-diantiquark system such as  $cu\bar{c}\bar{u}$ , but this would imply the presence of other states as  $cd\bar{c}\bar{d}$ ,  $cd\bar{c}\bar{s}$  and  $cu\bar{c}\bar{d}$  which have never been observed experimentally.

The  $X(3872)$  was only the first unexpected resonance to appear: it was followed by many others in the  $c\bar{c}$  region and also one in the  $b\bar{b}$  region (see Table 1.2 for the full compilation). Some of these resonances have been seen by different experiments, while others need confirmation; for all these states more experimental constraints and theoretical insight are needed.

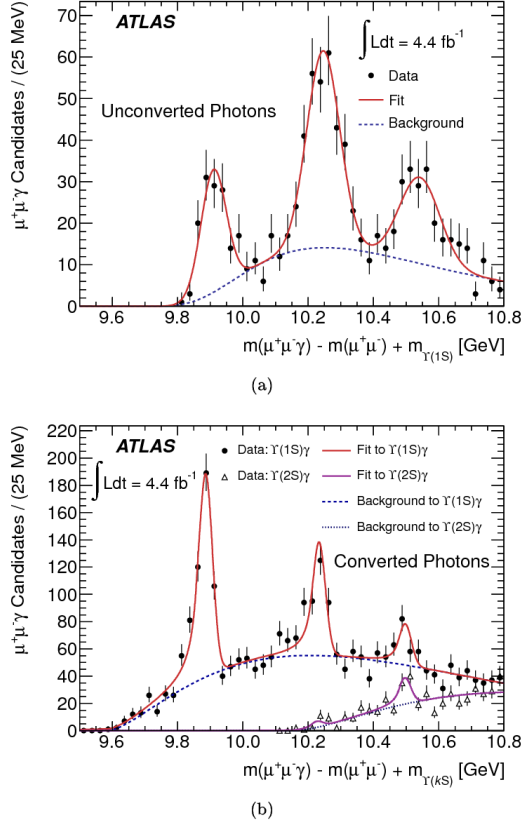


Figure 1.3: ATLAS' discovery of the  $\chi_b(3P)$ . (a) Mass distribution of  $\chi_b(3P) \rightarrow Y(1S)\gamma$  candidates for unconverted photons. (b) Mass distribution of  $\chi_b(3P) \rightarrow Y(kS)\gamma$  ( $k = 1, 2$ ) candidates for converted photons.



### 1.1.4 The latest discovery: the $\chi_b(3P)$

Very recently, in December 2011, the ATLAS collaboration reported [19] on the observation of a new conventional quarkonium state: the  $\chi_b(3P)$ .

$\chi_b$  candidates were reconstructed with the ATLAS detector through the radiative decay modes  $\chi_b(3P) \rightarrow \Upsilon(1S)\gamma$  and  $\chi_b(3P) \rightarrow \Upsilon(2S)\gamma$ , in which the  $\Upsilon$  decays in two muons and the photon was reconstructed either through conversion to  $e^+e^-$  or by direct calorimetry measurement. Previous experiments measured the  $\chi_b(1P)$  and  $\chi_b(2P)$ , but the  $\chi_b(3P)$  did never appear before, even if it was predicted and was supposed to have a mass of approximately 10.52 GeV. In Figure 1.3 the mass distribution for  $\chi_b \rightarrow \Upsilon(1S, 2S)\gamma$  candidates is shown in the case of converted and unconverted photons: the three peaks corresponding to the three states  $\chi_b(1P)$ ,  $\chi_b(2P)$  and  $\chi_b(3P)$  are well visible and the mass of the last resonance was found to be  $10541 \pm 11(\text{stat.}) \pm 30(\text{syst.}) \text{ GeV}/c^2$ , in very good agreement with the prediction.

## 1.2 $\psi$ and $\Upsilon$ states: decay and feed-down

The chronological overview carried out in the previous section gives an idea of the very fast discovery of the first quarkonia states and of the revolutionary power of such discoveries for the overall knowledge of elementary particle interactions.

The fact that the  $J/\psi$  and the other  $nS$  vector states were the first to be discovered is not an accident. In principle one could expect that the first to be discovered should have been the lowest mass charmonium state, *i.e.* the  $\eta_c(1S)$ . The difference between the scalar and the vector states is that the latter have a significant branching ratio for the double-lepton decay (BR=5.9% for  $J/\psi \rightarrow e^+e^-$  and the same for  $J/\psi \rightarrow \mu^+\mu^-$ ), while the former can only be detected through hadronic decay.

This rather high branching ratio into two leptons for the lower mass  $\psi$  and  $\Upsilon$  resonances is due to two reason. First of all these states are below the mass threshold for the decay in open heavy flavour hadrons ( $m_{J/\psi, \psi'} < 2m_D$  and  $m_{\Upsilon, \Upsilon', \Upsilon''} < 2m_B$ ). Secondly, the characteristics of colour interaction prevent these states to decay in a single gluon and quantum numbers conservation rules forbid the decay into two gluons: as a consequence the hadronic decay has to pass through three gluons emission and it is therefore suppressed. This is also the reason for having very narrow peaks: only 93 keV for the  $J/\psi$  and even less ( $\sim 54 \text{ keV}$ ) for the  $\Upsilon$ .

The aptitude of  $\psi$  and  $\Upsilon$  states to decay into leptons, especially into muons, is an incredible chance and is actually one of the most important characteristics of  $\psi$  and  $\Upsilon$

states. In high-energy hadron colliders, the number of background hadrons becomes large and complicates the detection of the signal under study. However this is not true for particles which decay into muons: these daughters are not stopped in the detectors they traverse (not even in hadronic calorimeters) and can be detected by dedicated spectrometers, leading to rather high Signal/Background ratios.

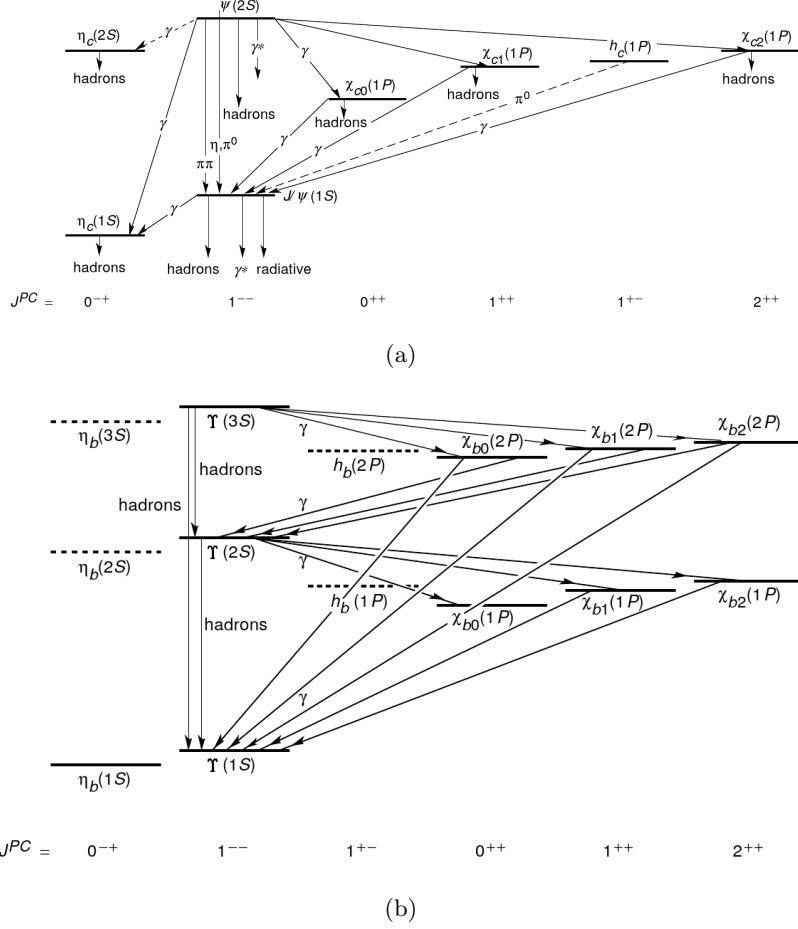


Figure 1.4: Charmonium (a) and Bottomonium (b) spectra for states under the open-heavy flavour pair production threshold. The radiative decay observed transitions are also shown as solid arrows.

Another important issue to be discussed about  $\psi$  and  $\Upsilon$  states concerns the feed-down from higher charmonia states and from open heavy flavours. First of all, radiative transitions from excited and 1P states are allowed. This means

that a  $J/\psi$  can come from the direct hadronization of a  $c\bar{c}$  pair or by the decay of a  $\psi(2S)$  or a  $\chi_{cn}(1P)$ : the first case is denoted as “direct”  $J/\psi$ , while the set of direct and radiative feeddown is called “prompt”  $J/\psi$  sample. The same thing is valid for the  $\Upsilon$ , with the difference that in this case many more states can decay into a  $\Upsilon(1S)$ . In Figure 1.4 all the states (with the exception of the newly discovered  $\chi_b(3P)$ ) of charmonia and bottomonia families are shown together with their radiative transitions into lower mass states.

This is all what concerns the  $\Upsilon$  family, but for the  $\psi$  another contribution has to be considered. Bottomed mesons ( $B^\pm, B^0, B_s^0$  and  $B_c^\pm$ ) can in fact weakly decay into  $J/\psi$  or  $\psi'$ , plus the formation of one or more hadrons. The result is the so-called non-prompt  $J/\psi$  (or  $\psi'$ ). Prompt + non-prompt  $J/\psi$  form an “inclusive” sample.

From the experimental point of view it is rather important to know how much of the inclusive yield comes from direct or prompt resonances, since theoretical predictions are hardly made for inclusive production and the feeddown, if significant, can make the comparison data-theory less meaningful.

For what concerns the non-prompt component, it is subtracted from the inclusive yield exploiting the fact that  $B \rightarrow J/\psi + X$  is a weak process and occurs with a  $c\tau \sim 0.5$  mm: the  $J/\psi$  daughter particles (e.g. two muons) will then point back to a different vertex with respect to the one corresponding to the primary collision. It is therefore sufficient to have a vertex detector with a good resolution in the determination of this “secondary vertex” to be able to subtract from the inclusive sample the non-prompt component. This is usually achieved with the silicon technology, as can be seen for the ALICE case in Chapter 3 Section 3.2.

In the case of the radiative decays the situation is more complicated since the transition occurs instantaneously (at the scale of the electromagnetic interaction) and no proper-time cut can be applied. The common way to proceed is to measure the cross-section for the production of the higher mass states and, through the branching ratio, to calculate the amount of lower states coming from the radiative decay. This is much more difficult with respect to the prompt component determination, since higher mass states are in general more difficult to be detected: the  $1S$  states can be studied in their di-lepton decay, but for the  $\chi$  case the hadronic channel has to be used, with much higher backgrounds.

The four LHC experiments have recently started publishing results on the feeddown fractions of the inclusive  $J/\psi$  yield for p-p collisions at  $\sqrt{s} = 7$  TeV and more details will be given in Section 1.6.

### 1.3 Theoretical description of quarkonia states

Quarkonia states are systems composed by two heavy quarks, each having mass  $m$  ( $m_c \simeq 1.3 \text{ GeV}/c^2$  and  $m_b \gtrsim 4.2 \text{ GeV}/c^2$ ) much larger than the QCD confinement scale  $\Lambda_{\text{QCD}}$  ( $\sim 217 \text{ MeV}$ ). The system is nonrelativistic and it is therefore characterized by the heavy-quark bound-state velocity,  $v \ll 1$ , ( $v^2 \sim 0.3$  for  $c\bar{c}$  and  $\sim 0.1$  for  $b\bar{b}$  in natural units<sup>7</sup>) and by a hierarchy of energy scales: the mass  $m$  (hard scale), the relative momentum  $p \sim mv$  (soft scale), and the binding energy  $E \sim mv^2$  (ultrasoft scale). For energy scales close to  $\Lambda_{\text{QCD}}$ , perturbation theory breaks down and one has to rely on nonperturbative methods.

Since  $m \gg \Lambda_{\text{QCD}}$ ,  $\alpha_s(m) \ll 1$  and phenomena occurring at the scale  $m$  can always be treated perturbatively. The coupling starts to be larger at the  $mv \sim p \sim 1/r$  scale for most of the quarkonia, with the exception of the lowest states: for the  $\Upsilon(1S)$  the radius is  $\sim 0.15 \text{ fm}$ , resulting in  $\alpha_s(mv) \sim 0.4$ , but already for the  $J/\psi$  ( $r \sim 0.25 \text{ fm}$ ) it becomes of the order of  $\sim 0.7$ . The ultrasoft scale has always to be considered as non-perturbative.

This hierarchy of nonrelativistic scales separates quarkonia from the other mesons and makes the theoretical description of quarkonium physics more complicated. All the scales get entangled in a typical amplitude involving a quarkonium observable: annihilation and production take place at the scale  $m$ , the binding at the scale  $mv$  and very low-energy gluons and light quarks emission at the scale  $mv^2$ .

For this reason, the characteristics of quarkonia states cannot be inferred from perturbative QCD calculations, but must be extracted starting from different approaches, such as non-relativistic effective field theories (NR EFTs), Lattice QCD (LQCD) or purely phenomenological models. It's out of the scope of this work to describe in details these methods, but a brief summary is given in the following.

#### 1.3.1 NR EFTs

The modern approach to heavy quarkonium is provided by NonRelativistic Effective Field Theories, which exploit the presence of the hierarchy of scales

$$m \gg p \sim 1/r \sim mv \gg E \sim mv^2$$

to describe physical observables at a given scale, by integrating out all the contributions at higher scales. If quarkonium production or annihilation, which happen at the scale

---

<sup>7</sup>Natural units are a convenient way to express physical quantities in particle physics. They are chosen in order to have:  $c = \hbar = k_B = 1$ .

$m$ , are under study, the suitable EFT is NonRelativisticQCD (NRQCD) [18, 20, 21], which follows from QCD by integrating out the scale  $m$ . On the contrary, if one is interested in quarkonium formation, whose typical scale is  $mv$ , the suitable EFT is the potential-NRQCD (pNRQCD) [22, 23], which follows from NRQCD by integrating out the scale  $mv$ . As underlined before, the  $mv$  scale can be higher or comparable to  $\Lambda_{\text{QCD}}$ : in the first case the so-called weakly-coupled pNRQCD theory is used (the matching between NRQCD and pNRQCD can be done in perturbation theory), while in the second case a strongly-coupled pNRQCD has to be adopted. More details on the NRQCD approach are given in Section 1.4, where the theoretical description of quarkonium production is considered.

### 1.3.2 LQCD

Lattice QCD [18] is a non-perturbative treatment of QCD, formulated on a discrete lattice of space-time coordinates. The discretization of the space-time continuum provides two main advantages. On the one hand, it acts as a non-perturbative regularization scheme since at finite values of the lattice spacing there are no ultraviolet infinities. On the other hand, it allows to calculate correlation functions and matrix elements through Monte-Carlo simulations. The only tunable input parameters in these simulations are the strong coupling constant and the bare masses of the quarks.

Numerical lattice QCD calculations using Monte Carlo methods can be extremely computationally demanding and require the use of large computer clusters devoted to this kind of studies: for this reason the spacing  $a$  and the total size of the lattice have to be chosen accurately. Ideally, lattice simulations are repeated at several values of the lattice spacing and the results then extrapolated to the continuum limit. Lattice artifacts become large if the physics under study are of the same order of the inverse of the lattice spacing. In this sense, the hard scale  $m$  of quarkonium becomes challenging since the spacing has to be chosen in order to have  $m \ll a^{-1}$ . To avoid these problems, two receipts are followed: integrate out the  $m$  scale and simulate NRQCD or integrate also the  $mv$  scale and simulate pNRQCD.

Despite the problems discussed, LQCD computation has started being more and more reliable, as can be seen in Figure 1.5 for the case of the calculation of the angular and energy splitting of bottomonia states with a lattice regularization of NRQCD [24].

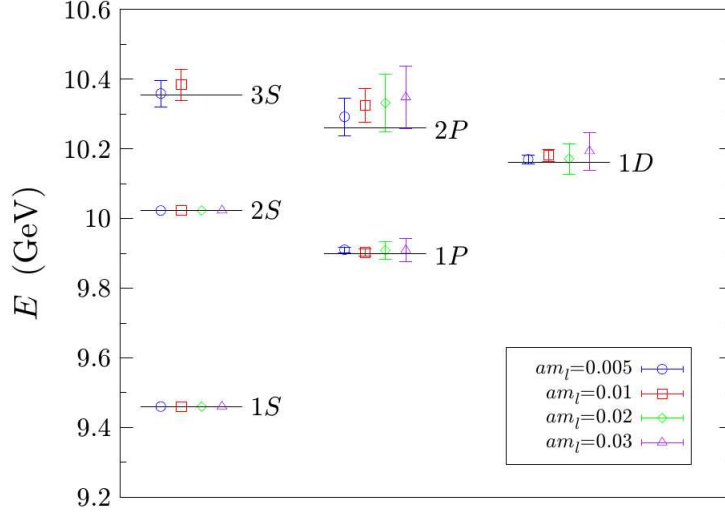


Figure 1.5: Radial and orbital energy splittings of bottomonium, as obtained by [24], compared to the experimental results (indicated by lines). The four sets of points correspond to four different assumptions on the light quarks ( $u$  and  $d$ ) masses. The 1S and 2S masses, for which no error bars are shown, are not an outcome of the lattice calculation, as these states were used as a reference.

### 1.3.3 Purely phenomenological models

An early, but still useful, technique uses an effective potential to calculate the masses of quarkonia states. In this technique, the fact that the motion of the quarks that comprise the quarkonium state is non-relativistic is exploited to assume that they move in a static potential, as in the case of non-relativistic models of the hydrogen atom. One of the most popular is the so-called Cornell potential, which can be written as:

$$V(r) = \frac{a}{r} + br, \quad (1.1)$$

where  $r$  is the effective radius of the quarkonium state and  $a$  and  $b$  are phenomenological parameters. This potential has two parts:

- the first part,  $a/r$ , corresponds to the potential induced by one-gluon exchange between the quark and its anti-quark, and is known as the Coulombic part of the potential, since its  $1/r$  form is identical to the well-known Coulombic potential induced by the electromagnetic force;

- The second part,  $br$ , is known as the confinement part of the potential, and parameterizes the non-perturbative effects.

Generally, when using this approach, a convenient form for the wave function of the quarks is taken, and then  $a$  and  $b$  are determined by fitting the results of the calculations to the masses of well-measured quarkonium states. Relativistic effects can be incorporated into this approach by adding extra terms to the potential, as it happens for the hydrogen atom in non-relativistic quantum mechanics.

This approach has no good theoretical motivation, but is popular because it allows for accurate predictions of the quarkonia parameters, without a lengthy lattice computation, and provides a separation between the short-distance Coulombic potential and the long-distance confinement effects that can be useful in understanding the mechanism of deconfinement (described in Section 1.8).

## 1.4 Theoretical description of quarkonium production

Many theoretical models have been developed from the eighties onwards to describe quarkonium production. The processes involved in the  $q\bar{q}$  creation and subsequent formation of the bound state strongly depend on the colliding particles [18]:

- in **hadroproduction** (two hadrons collision) the main characters are quarks and gluons. Past experiments ruled out the hypothesis of electromagnetic production via  $q\bar{q}$  annihilation, since it was shown that the production rate of  $J/\psi$  is identical in  $\pi^+ - N$  and  $\pi^- - N$  collisions (the difference in electric charge between the  $u$  and  $d$  quarks should suppress the production in  $\pi^+ - N$  collisions by a factor 4). Similarly, the hypothesis of  $q\bar{q}$  annihilation into a gluon as the main production process was rejected after the comparison between the production rate in  $p - p$  and in  $p - \bar{p}$  collisions, since the difference between the  $\bar{q}$  content in proton and anti-proton should lead to a suppression in  $p - p$  by a factor  $5 \div 10$ , which is not observed. The dominant processes are therefore gluon fusion and gluon fragmentation, as shown in Figure 1.6(a,b,c).
- in lepton-hadron collisions the process can either be **photoproduction** or **leptoproduction**: the Feynman diagrams in the two cases are rather similar and correspond to photon-gluon fusion (see Figure 1.6(d)). The difference between the two processes is the virtuality of the photon which, in case of leptoproduction is very high (DIS), while for photoproduction is almost zero.

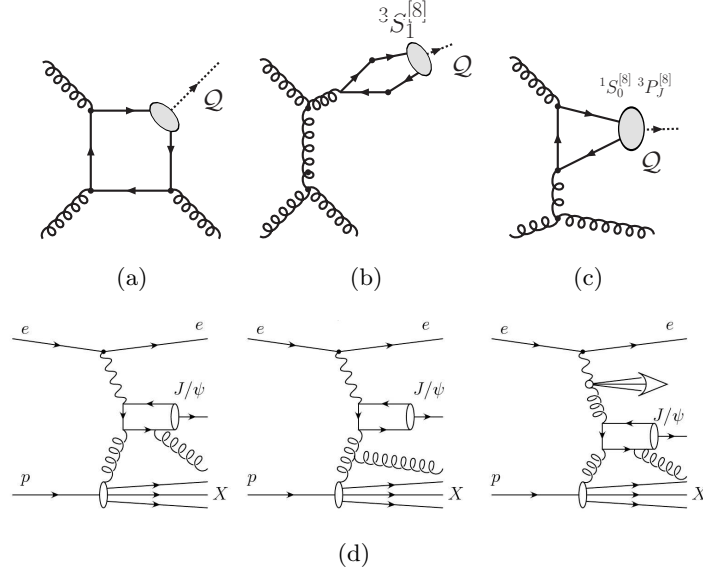


Figure 1.6: Feynman diagrams for  $J/\psi$  hadro- and photo-(lepto-)production. The LO color-singlet (a) and color-octet (b,c) contributions are shown for hadro-production. For photo-(lepto-)production (d) the first and the third diagrams can contribute in color-singlet or color-octet, while the second one can only be in octet state.

When the photon fluctuates in a  $q\bar{q}$  pair at long distance and the couple interacts with two gluons coming from the hadron, the process is called “**diffractive**” production and is characterized by a very low deviation of the colliding systems.

- in  $e^+e^-$ , quarkonium is produced from  $\gamma\gamma$  collisions, from decay of open bottomed mesons (in the case of charmonium) or from the decay of higher quarkonia states.

In the following we will mainly concentrate on hadroproduction, but some considerations on the other processes will also be done.

As already discussed in Section 1.3, a quarkonium system has three intrinsic energy scales:  $m$ ,  $mv$  and  $mv^2$ , where  $m$  is the mass of the constituent quarks and  $v$  the typical velocity of the heavy quark and anti-quark in the system’s rest frame. If a heavy quarkonium is produced in a hard-scattering process, then, in addition to the intrinsic scales of the system, the hard-scattering scale  $p$  enters into the description of the production process. In hadron-hadron and lepton-hadron collisions  $p$  corresponds



to the transverse momentum of the quarkonium system, while in  $e^+e^-$  processes it is taken as the quarkonium momentum in the  $e^+e^-$  center of mass frame  $p^*$ .

An intuitive expectation might be that the production process could be understood in terms of two distinct steps: the production of the  $q\bar{q}$  pair, occurring at the scale  $p$ , and the subsequent evolution into the quarkonium state, which would involve the softer scales  $mv$  and  $mv^2$ . The first step, corresponding to the so-called “short distance process”, would be calculable in an expansion in powers of  $\alpha_s(p)$ , while the second step would involve non-perturbative physics, also called “long distance” processes.

In order to establish that this intuitive picture of quarkonium production is actually a property of QCD, one must demonstrate that the short distance perturbative effects at the scale  $p$  can be separated from the long-distance non-perturbative dynamics. Such a separation is known as factorization and represents the basic assumption for all the models which aspire to a coherent description of quarkonium production. If it can be further demonstrated that the long distance part can be considered as universal, *i.e.* not dependent on the process under study, then the predictive power of such an approach becomes much higher.

Many models have been adopted to describe the non perturbative evolution of the  $q\bar{q}$  pair into a quarkonium system and currently the most used are the Color-Singlet Model (CSM), the Color-Evaporation Model (CEM) and the NonRelativistic QCD (NRQCD). In the following some details on each model are given.

#### 1.4.1 Color Singlet Model (CSM)

This model [18] was the first proposed shortly after the discovery of the  $J/\psi$  [25, 26, 27] and was applied, with some success, to predict production cross sections for low energy experiments, where the data extended to at most 6 GeV/ $c$  in transverse momentum. It was then applied to higher energy experiments up to Tevatron, when it was put aside since the predictions on the  $\psi$  states were orders of magnitude lower than the experimental results (see Section 1.5). Recently it has been revived, with the computation at higher orders in the  $\alpha_s$  expansion [28, 29, 30], since it was found to better accomodate polarization results from Tevatron with respect to NRQCD.

The model assumes factorization and the hard part of the cross-section is calculated via perturbative QCD. For the softer contributions, a basic assumptions is made: the color and the spin of the  $q\bar{q}$  pair do not change during the binding and, therefore, the hard scattering has to produce a colour singlet pair. Hence the name Color-Singlet

Model.

The greatest quality of this model resides in its very high predictive power as the only input required, a part from the PDF in case of hadronic collisions, is the absolute value of the color-singlet  $q\bar{q}$  wave function and its derivatives. These quantities can be determined from data of decay processes or by the application of potential models. Once these quantities are provided, the CSM has no free parameters.

### 1.4.2 Color Evaporation Model (CEM)

The Colour Evaporation Model [18] is the most phenomenological one and was first proposed in 1977 [31]. In the CEM, the cross-section for a quarkonium state  $H$  is some fraction  $F_H$  of the cross-section for producing  $q\bar{q}$  pairs with invariant mass below the  $M\bar{M}$  threshold, where  $M$  is the lowest mass meson containing the heavy quark  $q$ . This cross-section has an upper limit on the  $q\bar{q}$  pair mass but no constraints on the colour or spin of the final state. The  $q\bar{q}$  pair is assumed to neutralize its colour by interaction with the collision-induced colour field by “colour evaporation”. An important feature is that the fractions  $F_H$  are assumed to be universal so that, once they are determined by data, they can be used to predict the cross-sections in other processes and in other kinematical regions.

The leading-order calculation cannot describe the quarkonium  $p_t$  distribution, since the  $p_t$  of the  $q\bar{q}$  pair is zero at LO. At NLO in  $\alpha_s$  the subprocesses  $ij \rightarrow kq\bar{q}$  (where  $i, j$  and  $k$  are light quarks, antiquarks and gluons) produce  $q\bar{q}$  pairs with non-zero  $p_t$ . From complete NLO CEM calculations of quarkonium production in hadronic collisions the  $F_H$  values have been determined.

The most basic prediction of the CEM is that the ratio of the cross-sections for any two quarkonium states should be constant, independently from the process and the kinematical region. Some variations in these ratios have been observed: for example the ratio of the cross-sections for  $\chi_c$  and  $J/\psi$  are rather different in photoproduction and hadroproduction. Such variations represent a serious challenge to the status of the CEM as a quantitative phenomenological model for quarkonium production; nevertheless the model is still widely used as simulation benchmark since, once the  $F_H$  fractions are determined, it has a full predicting power.

### 1.4.3 Non Relativistic QCD (NRQCD)

One convenient way to carry out the separation between perturbative and non perturbative effects is through the use of Non Relativistic QCD (NRQCD), which was briefly introduced in Section 1.3 and is extensively reviewed in [18, 21, 32]. It is more than a phenomenological model since it reproduces full QCD accurately at momentum scales of order  $mv$  and smaller and, for this reason, deserves the rank of effective theory.

The inclusive cross-section for the direct production of the quarkonium state  $H$  at large transverse momentum ( $p \gtrsim m$ ) can be written as a sum of products of NRQCD matrix elements and short-distance coefficients:

$$\sigma[H] = \sum_i \sigma_n(\Lambda) \langle 0 | \mathcal{O}_n^H | 0 \rangle \quad (1.2)$$

where:

- $H$  is the quarkonium state to be produced;
- $n$  runs over all the quantum numbers of the  $q\bar{q}$  pair (colour, angular momentum, spin, ...);
- $\Lambda$  is the ultraviolet cutoff of the effective theory;
- $\sigma_n(\Lambda)$  are the short-distance coefficients;
- $\mathcal{O}_n^H$  are the four-fermion operators.

The short-distance coefficients  $\sigma_n(\Lambda)$  are essentially the process-dependent partonic cross-sections to produce a  $q\bar{q}$  pair, convolved with parton distribution functions if there are hadrons in the initial state. The  $q\bar{q}$  pair can be produced in a colour-singlet or color-octet state, its spin state can be singlet or triplet, and it also can have orbital angular momentum.

The four-fermion operators  $\mathcal{O}$  create a  $q\bar{q}$  pair in the NRQCD vacuum, project it into a state that in the asymptotic future consists of a heavy quarkonium plus anything, and then annihilate the  $q\bar{q}$  pair. The vacuum matrix element of such an operator is the probability for a  $q\bar{q}$  pair to form a quarkonium plus anything. These matrix elements are somewhat analogous to parton fragmentation functions: they contain all the non-perturbative physics associated with the evolution of the  $q\bar{q}$  pair into a quarkonium state.

Unlike the CSM and the CEM predictions for the production cross section, the NRQCD factorization formula for heavy-quarkonium production depends on an infinite number of unknown matrix elements. However, the sum in Eq. 1.2 can be organized as an expansion in powers of  $v$ : hence, the NRQCD factorization formula is a double expansion in powers of  $v$  and  $\alpha_s$ . In phenomenological applications, the sum in Eq. 1.2 is truncated at a fixed order in  $v$ , and typically only a few matrix elements enter into the phenomenology. The predictive power of the NRQCD factorization approach is based on the validity of such a truncation, as well as on the universality of the long-distance matrix elements.

Retaining in Eq. 1.2 only the color-singlet contributions of leading order in  $v$  for each quarkonium state, the CSM is obtained. Such a truncation leads to inconsistencies, because the omission of color-octet contributions results in uncanceled infrared divergences in the production rates of P-wave and high orbital angular momentum quarkonium states. If, on the other hand, some relationships between the NRQCD long-distance matrix elements are imposed, the CEM is obtained. These relationships are generally inconsistent with the scaling of the matrix elements with  $v$  that is predicted by NRQCD. The shortcomings of the CEM in describing the Fermilab Tevatron data (see Section 1.5) can be traced, at least in part, to these inconsistencies.

The NRQCD factorization approach has been applied successfully to many observables and the outcome of the comparison between experimental data and theory is reported in the following sections. Despite these successes, some open points still remain, both from the purely theoretical and from the phenomenological point of view. One of the crucial theoretical points is the validity of the factorization formula: it has been proven for the calculation of two exclusive amplitudes [33, 34] (exclusive production of quarkonium + light meson in B-meson decays and exclusive production of two quarkonium states in  $e^+e^-$  annihilation), but for the inclusive production no proof is available. Moreover, the NRQCD factorization formula is known to break down when an additional heavy quark is produced in close proximity to a  $q\bar{q}$  pair that evolves into a quarkonium: in this respect, experimental results on quarkonium + heavy-quark production would help in order to understand the magnitude of this process and to bolster or run down Eq. 1.2.

As a last remark, it is worth underlying that LO NRQCD had problems in describing polarization results on prompt  $J/\psi$  production at Tevatron and this was the reason for a revival of the CSM in the last years. More details on this point will be given in

Chapter 2 Section 2.7.1.

## 1.5 Experimental results on quarkonium production before the LHC era

Many experimental results have been accumulated on quarkonium production since the first discovery of the  $J/\psi$  in 1974. Most of the results obtained by the first experiments can now be considered as obsolete, since the higher quality of the more recent ones makes the comparison between theory and data more accurate. In this section the outcome of this comparison for lepton-lepton, lepton-hadron and hadron-hadron collisions is revised, referring to LEP and B-factories data for  $e^+e^-$ , to HERA-B for  $e-p$  and to Tevatron and RHIC for hadronic collisions. The LHC case will be considered in the next section.

### Results from Tevatron

In Run I of the Tevatron, the CDF collaboration measured the cross-section for the production of several charmonium states in  $p\bar{p}$  collisions at a center-of-mass energy of 1.8 TeV. The results are shown in Figure 1.7 for the production of direct  $J/\psi$ , prompt  $\psi(2S)$ ,  $J/\psi$  from  $\chi_c$  and inclusive  $\Upsilon(1S)$ . The observed cross sections were more than an order of magnitude greater than the calculated ones at leading order (LO) in  $\alpha_s$  in the CSM [35]. This fact decreed the crisis of CSM and triggered many theoretical studies on quarkonium hadroproduction, especially in the framework of NRQCD. All these studies lead to the work of Cho and Leibovich [36, 37], who succeeded, applying NRQCD at LO and including gluon fragmentation contributions at high  $p_t$ , to perfectly fit<sup>8</sup> CDF's results on  $\psi$  production (see Figure 1.7), opening the doors to the new approach in the interpretation of quarkonium production. The application of NRQCD at LO to the  $\Upsilon(1S)$  differential  $p_t$  cross-section lead to a satisfactory result from 8 GeV/ $c$  onwards, while at lower transverse momenta the theoretical curve diverges (NLO computation and resummation of multiple gluon radiation would probably help in approaching the data).

---

<sup>8</sup>for CSM we usually talk about “predictions” while for NRQCD of “fits”: this difference comes from the fact that, as explained in Section 1.4.1 and 1.4.3, the CSM only needs the  $q\bar{q}$  wave function as an input and than has no free parameters, while NRQCD calculations consist in fitting the experimental data in order to extract the non-perturbative matrix elements.

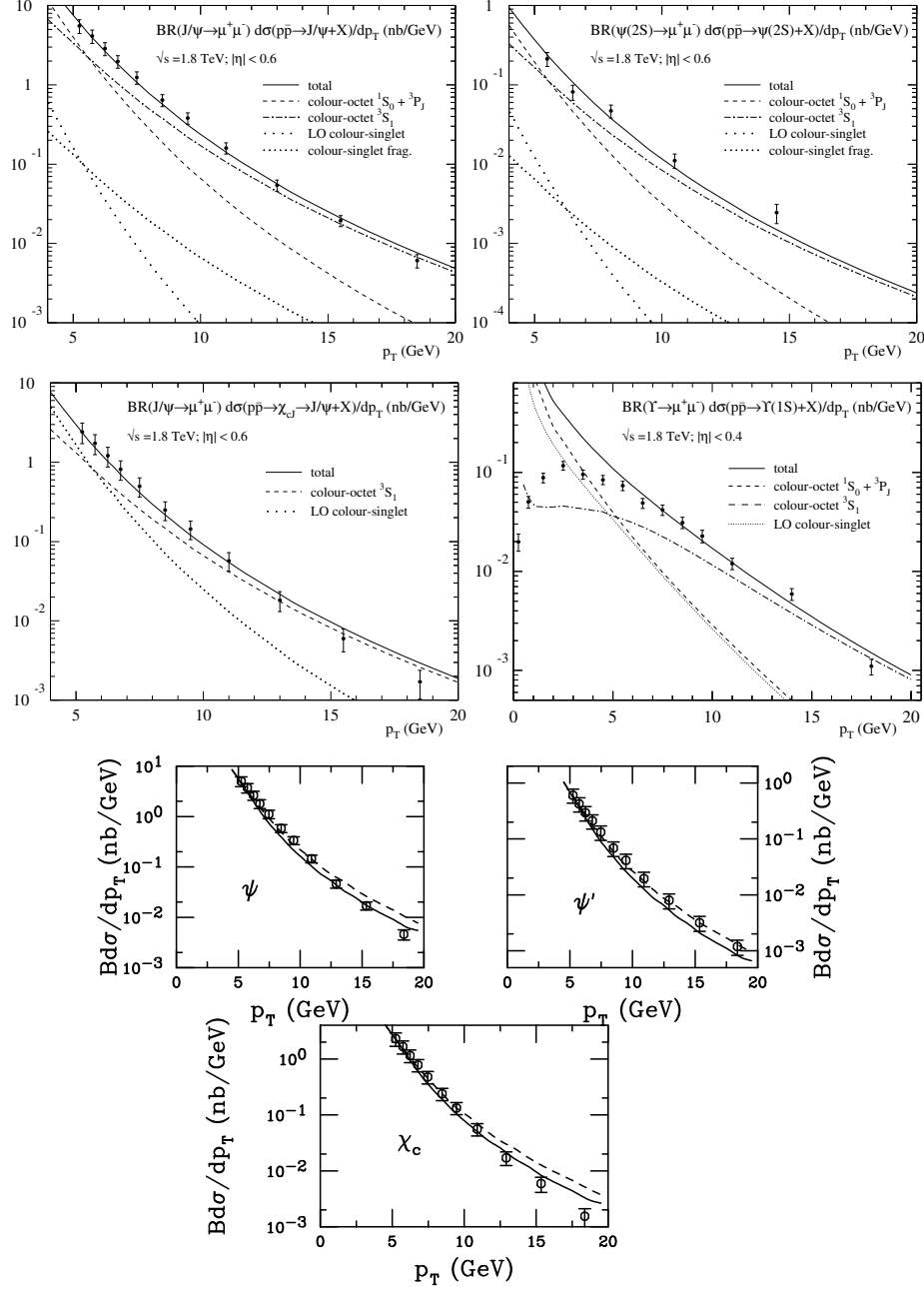


Figure 1.7: Cross section as a function of the transverse momentum for direct  $J/\psi$ , prompt  $\psi(2S)$ ,  $J/\psi$  from  $\chi_c$  and  $\Upsilon$  production at  $\sqrt{s} = 1.8$  TeV measured by the CDF experiment at Tevatron. Experimental data are compared to LO NRQCD and LO CSM and to NLO CEM. From [18].

Both normalization and shape of prompt charmonium and of bottomonium cross sections can be reasonably well described by the CEM when a proper  $k_t$  smearing<sup>9</sup> is applied, as can be seen in Figure 1.7.

Once the non-perturbative matrix elements were extracted from the fit to CDF's data, a theoretical estimation based on NRQCD was made for the degree of polarization of direct  $J/\psi$  and  $\Upsilon$  production. On this observable the disagreement between theory and CDF and D0 data revealed to be striking: more details on this aspect will be given in Chapter 2 Section 2.7.1.

This failure of NRQCD in describing polarization prompted new theoretical efforts from the CSM side. Calculations at higher order in  $\alpha_s$  were performed [28, 29, 30, 38] for  $\Upsilon(nS)$  at Tevatron Run I and for  $\psi(2S)$  at Tevatron Run II. The corrections were found to be quite important, especially at high  $p_t$ , leading to a better agreement of CSM with the experimental results for the  $p_t$  differential cross section, as can be appreciated in Figure 1.8. Also NLO corrections to the NRQCD fits were computed, resulting in very small differences with respect to the LO case.

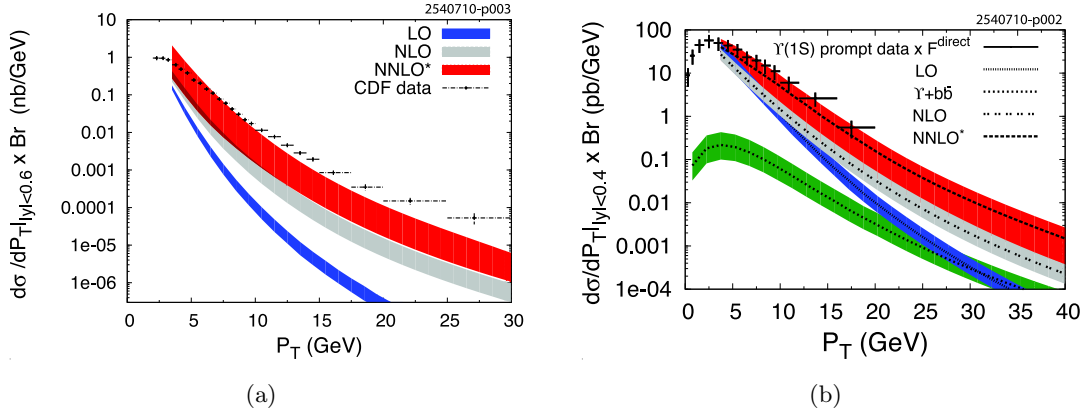


Figure 1.8: Cross section as a function of the transverse momentum for prompt  $\psi(2S)$  (a) and  $\Upsilon(1S)$  production as measured by the CDF experiment [39, 40]. Experimental data are compared to LO (green and blue bands), NLO (light blue bands) and NNLO\* (truncation of the full NNLO expansion - red bands) CSM calculations. From [30, 38].

The issue of the feeddown was also perused by CDF. Using data from Run I of the Tevatron, the fractions of prompt  $J/\psi$  that come from decays of  $\psi(2S)$  and  $\chi_c(1P)$

<sup>9</sup>In the  $k_t$  smearing approach the colliding partons are not collinear, but have a proper transverse momentum distribution. The advantage of this technique is that at lower orders in  $\alpha_s$  it contains contributions that appear at higher order in the usual collinear calculation

states and the fraction that are produced directly were extracted [41]. The measurements were made for  $J/\psi$  with transverse momentum  $p_t > 4$  GeV/ $c$  and pseudo-rapidity  $|\eta| < 0.6$ . The fraction of  $J/\psi$  that are directly produced is of the order of 64% and approximately constant over the range  $5 < p_t < 15$  GeV/ $c$ . The fraction from decays of  $\psi(2S)$  increases from  $\sim 7\%$  at  $p_t = 5$  GeV/ $c$  to  $\sim 15\%$  at  $p_t = 15$  GeV/ $c$ . The fraction from decays of  $\chi_c(1P)$  seems to decrease slowly over this range of  $p_T$  and is of the order of 30%. Such variations with  $p_t$  disagree with the predictions of the colour-evaporation model.

The CDF collaboration has also measured the ratio of the prompt  $\chi_{c1}$  and  $\chi_{c2}$  cross-sections at the Tevatron [42]. The measured value of the ratio  $R_{\chi_c}$  is

$$R_{\chi_c} = \frac{\sigma[\chi_{c1}]}{\sigma[\chi_{c2}]} = 1.04 \pm 0.29(\text{stat.}) \pm 0.12(\text{sys.}). \quad (1.3)$$

The colour-evaporation model predicts that this ratio should be close to the spin-counting ratio  $3/5$ , while the NRQCD factorization fit to the prompt  $\chi_c$  cross-section in the region  $p_t > 5$  GeV/ $c$  implies a ratio of  $0.9 \pm 0.2$ . The CDF result slightly favors the NRQCD factorization prediction.

## Results from RHIC

The PHENIX and STAR collaborations at RHIC have reported analysis of prompt  $J/\psi$  production for values of  $p_t$  up to 12 GeV/ $c$  [43, 44] in  $pp$  collisions at  $\sqrt{s_{NN}} = 200$  GeV.

In STAR's paper the measured production rate as a function of  $p_t$  was compared with predictions based on NRQCD factorization at LO [45] and the CSM up to NNLO\* accuracy [30]. The calculations did not include feeddown from the  $\psi(2S)$  and the  $\chi_c$  states. Data favored NRQCD over CSM, but no definite conclusions could be drawn because the effects of feeddown were not taken into account.

A calculation of prompt  $J/\psi$  production at RHIC, including feeddown from the  $\psi(2S)$  and the  $\chi_c$ , has been carried out recently [46] in the CSM and NRQCD factorization formalism at LO. In Figure 1.9(a) the comparison between these calculations and PHENIX's results for prompt  $J/\psi$  production is shown: again NRQCD at LO is favoured with respect to CSM at LO. Higher order corrections to the color-singlet contribution have been considered [47] and were found to be large: a comparison with the PHENIX and STAR prompt  $J/\psi$  cross-sections differential in  $p_t$  is shown in Figure 1.9(b). The color-singlet contributions through NLO agree with the PHENIX prompt  $J/\psi$  data for  $p_t$  in the range 1–2 GeV/ $c$ , but fall substantially below the



PHENIX and STAR data for larger values of  $p_t$ . The NNLO\* color-singlet contribution can be computed reliably only for  $p_t > 5$  GeV/ $c$ . The upper limit of the theoretical uncertainty band for the NNLO\* contribution is compatible with the PHENIX and STAR data, although the theoretical uncertainties are very large.

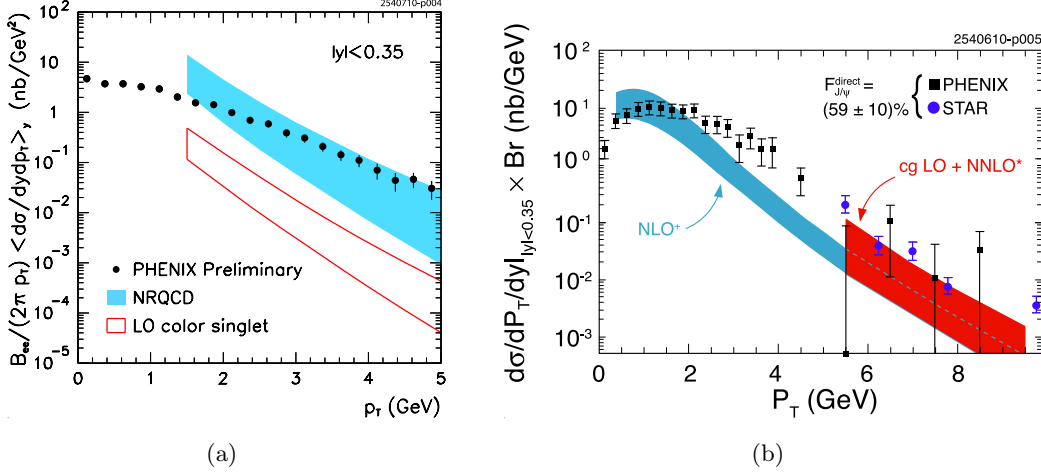


Figure 1.9:  $p_t$  dependence of the prompt  $J/\psi$  cross section as measured by PHENIX (a, b) and STAR (b) in  $pp$  collisions at  $\sqrt{s_{NN}} = 200$  GeV. In (a) the blue band corresponds to LO NRQCD [46] prediction, while the red line delimits the CSM LO prediction. In (b) blue and red bands show the CSM at NLO and NNLO\* respectively.

## Results from LEP and the B-factories

The inclusive cross section differential in  $p_t$  for the production of  $J/\psi$  in  $\gamma\gamma$  collisions at LEP has been measured by the DELPHI collaboration [48]. The same cross section has been calculated in the CSM and the NRQCD (using the non-perturbative matrix elements estimated from Tevatron's results) factorization approaches at LO in  $\alpha_s$  [49]. The comparison theory-data is shown in Figure 1.10. Data favour the NRQCD calculation, even if large NLO corrections to the color-singlet contribution are expected, in analogy to what seen for the hadroproduction.

A surprising result from the Belle Collaboration was that most of the  $J/\psi$  that are produced in  $e^+e^-$  annihilation at 10.6 GeV are accompanied by charmed hadrons [50]. The presence of a charmed hadron indicates the creation of a second  $c\bar{c}$  pair in addition to the pair that forms the  $J/\psi$ . A convenient measurement of the probability

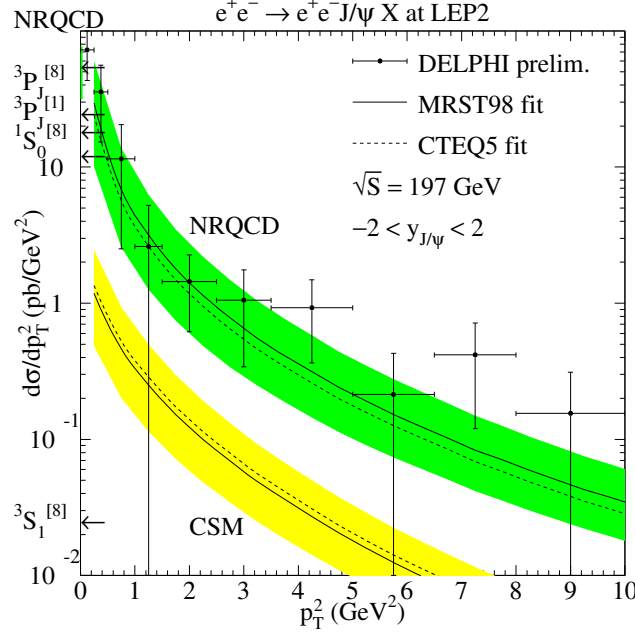


Figure 1.10: Differential cross-section for the process  $\gamma\gamma \rightarrow J/\psi$  as a function of  $p_T^2$  as measured by the DELPHI collaboration. The upper set of curves is NRQCD LO, the lower one is CSM LO. The solid and dashed curves correspond to different PDF inputs. From [49].

for creating the second  $c\bar{c}$  pair is the ratio

$$R_{\text{double}} = \frac{\sigma[e^+e^- \rightarrow J/\psi + X_{c\bar{c}}]}{\sigma[e^+e^- \rightarrow J/\psi + X]}. \quad (1.4)$$

Belle found that  $R \sim 0.6$  ( $R = 0.59_{-0.13}^{+0.15} \pm 0.12$ ), while the NRQCD factorization approach at LO led to the prediction  $R_{\text{double}} \approx 0.1$  [51], which clearly disagrees with the Belle result. Also the CSM at LO was found to underestimate the ratio, with a value between 0.1 and 0.3 [52]. The source of these discrepancies was found to arise primarily from the cross-section in the numerator of Eq. 1.4, *i.e.* from the difference between experimental data and theoretical predictions in the determination of the cross section for the production of a  $J/\psi$  plus a charmed meson.

Many efforts on the theoretical and experimental sides were made in the last years and a better agreement between data and NRQCD was obtained for the exclusive process  $e^+e^- \rightarrow J/\psi + \eta_c$ , which nevertheless counts for only  $\sim 6\%$  of the total  $e^+e^- \rightarrow J/\psi + X_{c\bar{c}}$  cross section. Other steps towards were done, very recently, with the computation of

the CSM prediction at NLO, which was found to introduce sizable corrections with respect to the LO case. As of today the discrepancy cannot be considered as solved, but the magnitude of the difference between theory and experimental results is not dramatic.

## Results from HERA

The ZEUS and H1 collaborations published several measurements of inelastic  $J/\psi$  and  $\psi(2S)$  production that are based on data from HERA Run I. A new measurement, making use of the full Run II data sample, was released recently by H1 [53], while ZEUS has published new results on the  $J/\psi$  decay angular distributions in inelastic photoproduction making use of the full data sample available, but this last measurement will be discussed in Chapter 2 Section 2.7.3.

$ep$  experiments usually measure cross-sections differentially in  $p_t$  (or  $p_t^2$ , as for *hadron–hadron* experiments) or in  $z$ , where  $z$  is the elasticity observable, defined as the fraction of energy of the incoming photon, in the proton rest frame, that is carried by the final-state quarkonium.

In Figure 1.11 the comparison between data from the H1 collaboration and calculations in the CSM and NRQCD factorization formalisms [54, 55] is shown. The contributions from resolved photoproduction (the  $\gamma$  interacts with the whole hadron and not directly with the quark), which are important in the low- $z$  region, and the contributions from diffractive production, which are important near  $z = 1$ , are not included in the NRQCD factorization prediction and lead to a bad agreement with the data (see Section 1.7 for news on this aspect). The non-perturbative matrix elements were obtained through a LO NRQCD fit to the Tevatron hadroproduction data, augmented by an approximate calculation of some higher-order corrections from multiple-gluon radiation. The NRQCD factorization approach at NLO accuracy in  $\alpha_s$  is in better agreement with the H1 data than the color-singlet contribution alone. However, the uncertainty bands for both the theoretical calculations are quite large.

## 1.6 The LHC era

The four LHC experiments (ALICE [56], ATLAS [57], CMS [58] and LHCb [59]) are taking data in  $pp$  collisions at  $\sqrt{s} = 7$  TeV since roughly 2 years. After this small amount of time they have already published many results on inclusive, prompt and non-prompt quarkonium cross sections, opening the doors of a new era in the under-

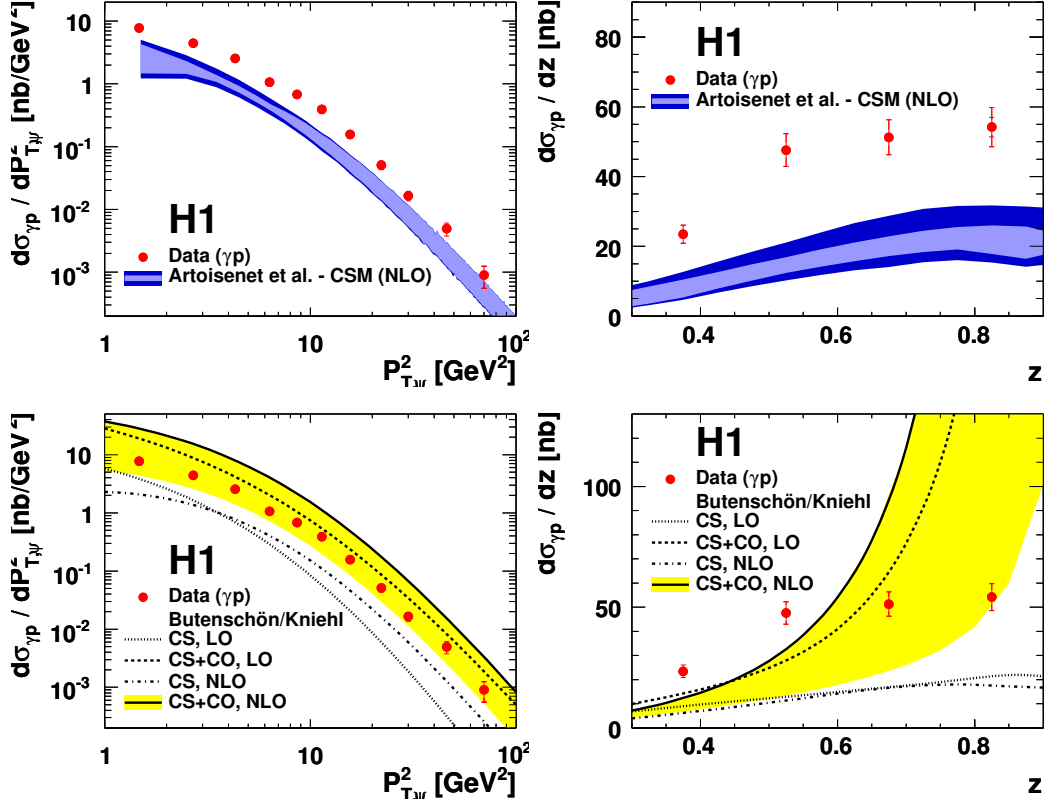


Figure 1.11:  $p_t^2$  and  $z$  differential cross section for  $J/\psi$  photoproduction at HERA as measured by the H1 experiment [53]. In the top(bottom) plots the comparison with NLO CSM (NLO CSM and NRQCD) predictions [54]([55]) is shown.

standing of quarkonium production in high energy hadronic collisions. Also collisions at  $\sqrt{s} = 2.76$  TeV have been delivered by the LHC and some preliminary results are also available at this energy.

The major results are here revised for each experiment separately.

### 1.6.1 ALICE

The ALICE collaboration has published in 2011 results on inclusive  $J/\psi$  production in a wide rapidity window (from -4 to +0.9) and down to  $p_t=0$  for  $pp$  collisions at  $\sqrt{s} = 7$  TeV [60] and has also presented preliminary results for collisions at  $\sqrt{s} = 2.76$  TeV.

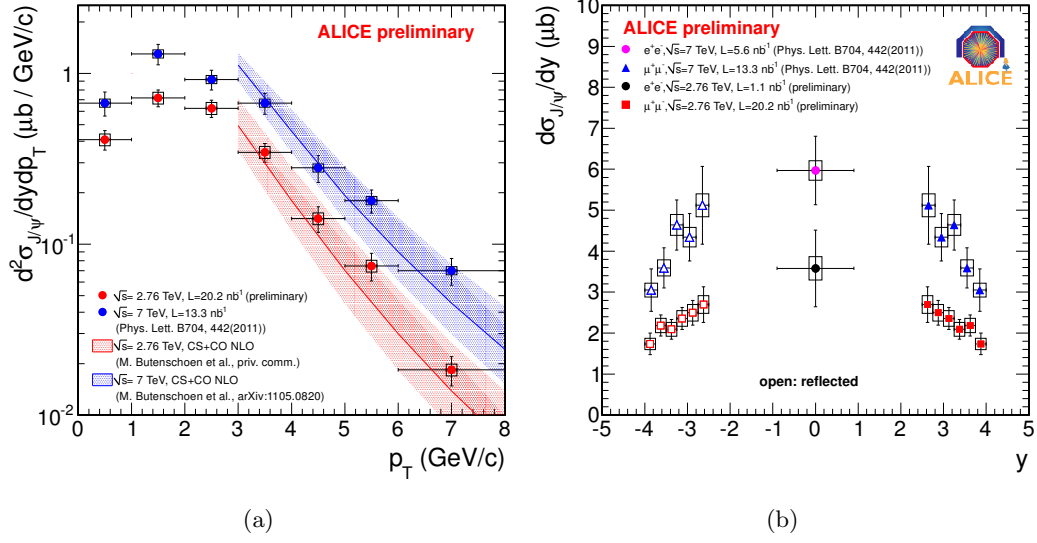


Figure 1.12:  $p_T$  and  $y$  differential cross sections for inclusive  $J/\psi$  production at  $\sqrt{s} = 7$  TeV and  $\sqrt{s} = 2.76$  TeV as measured by the ALICE experiment at the LHC. The red and blue bands in (a) show the NLO NRQCD global fit result (see Section 1.7 for more details).

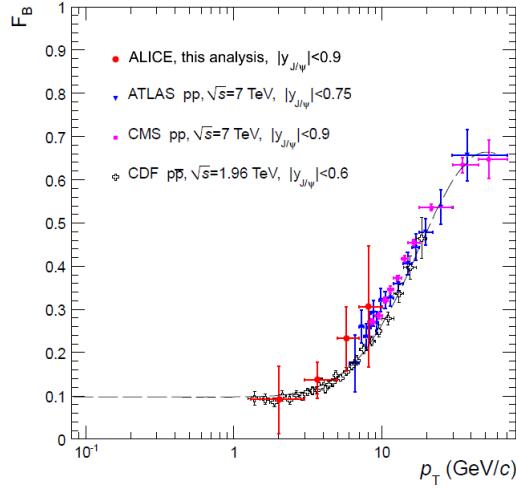


Figure 1.13:  $p_T$ -differential fraction of  $J/\psi$  coming from B-meson decays as measured by ALICE, ATLAS, CMS and CDF (Run II) at mid-rapidity. The rapidity intervals are slightly different in the four data sets. From [61].

These studies have been performed making use of a little fraction ( $\lesssim 20 \text{ nb}^{-1}$ ) of the integrated luminosity collected by the experiment.

The results are shown in Figure 1.12, together with the expectation for direct  $J/\psi$  production calculated through NRQCD computation at NLO (for more details on this theoretical result see Section 1.7): the agreement between data and theory is very good, even if the feeddown is not considered.

ALICE has also presented preliminary results on the  $p_t$ -differential fraction of  $J/\psi$  coming from B-meson decays at mid-rapidity ( $\eta < 0.9$ ). This is shown in Figure 1.13, together with the results from the other LHC experiments and from CDF at Tevatron. The agreement among the four LHC experiments is very good and the comparison with CDF data shows that this fraction is not strongly dependent on the center of mass energy of the collision, at least in the range between 1.8 and 7 TeV.

The first result at the LHC energy on  $J/\psi$  polarization was also published by the ALICE collaboration [62] and this is the main topic of this thesis: it will be deeply discussed in Chapter 4.

### 1.6.2 ATLAS

The ATLAS collaboration has studied inclusive, prompt and non-prompt  $J/\psi$  production [63] as well as inclusive  $\Upsilon$  production [64] at  $\sqrt{s} = 7 \text{ TeV}$ .

For the  $J/\psi$  case the  $p_t$  differential cross section have been compared with both CEM [65] and CSM [30] in four different rapidity bins. In Figure 1.14 the case of the most central rapidity bin is shown. The CEM prediction was made with  $k_T$  smearing and includes the radiative decays from higher charmonia states, so it is for prompt production and can be directly compared with data. The agreement between data and theory is very poor, in particular for what concerns the shape. The CSM prediction was calculated at NLO and NNLO\*: the second shows a significant improvement with respect to the first one both from the shape and from the normalization point of view. Nevertheless the agreement is only at low  $p_t$  and with the upper part of the theoretical uncertainty.

The fraction of  $J/\psi$  coming from the decay of B-mesons was studied in many bins of  $p_t$ , up to  $p_t = 70 \text{ GeV}/c$ , and in four bins of  $y$ . The result for the most central case is shown in Figure 1.13, together with the result from the other experiments.

The inclusive  $\Upsilon$  production cross section as a function of the transverse momentum and for two bins of rapidity was also published [64]. In this case the comparison with

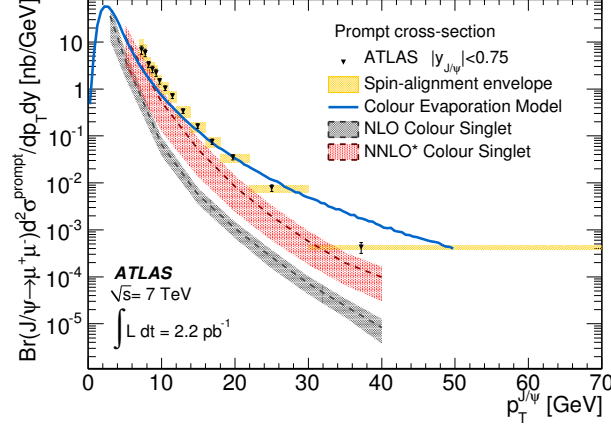


Figure 1.14:  $p_t$  differential cross section for prompt  $J/\psi$  production at  $\sqrt{s} = 7$  TeV measured by ATLAS at mid-rapidity. The grey and red bands are the CSM predictions at NLO and NNLO\* respectively, while the blue line is the CEM at NLO prediction.

the models is impossible since no theoretical calculation for  $\Upsilon$  production at the LHC was recently published.

### 1.6.3 CMS

The CMS experiment has shown very good performance in detecting muon pairs.

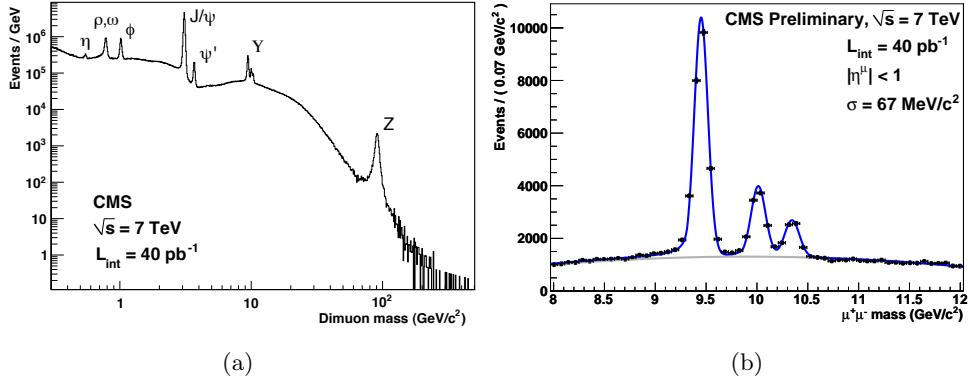


Figure 1.15: CMS quarkonia detection performance. Invariant mass unlike-sign muons in the 0-200  $\text{GeV}/c^2$  region (a) and in the 8-12  $\text{GeV}/c^2$  region (b).

In Figure 1.15(a) the dimuon invariant mass spectrum is shown for a little part of the statistics collected by the experiment at  $\sqrt{s} = 7$  TeV: all the resonances from the  $\eta$  to the  $Z$  are present and well separated in this textbook-like picture. In Figure 1.15(b) a zoom in the  $\Upsilon$  region allows to appreciate the separation capability among the three different peaks. These performances will allow the CMS collaboration to deliver very well detailed results both for charmonium and bottomonium.

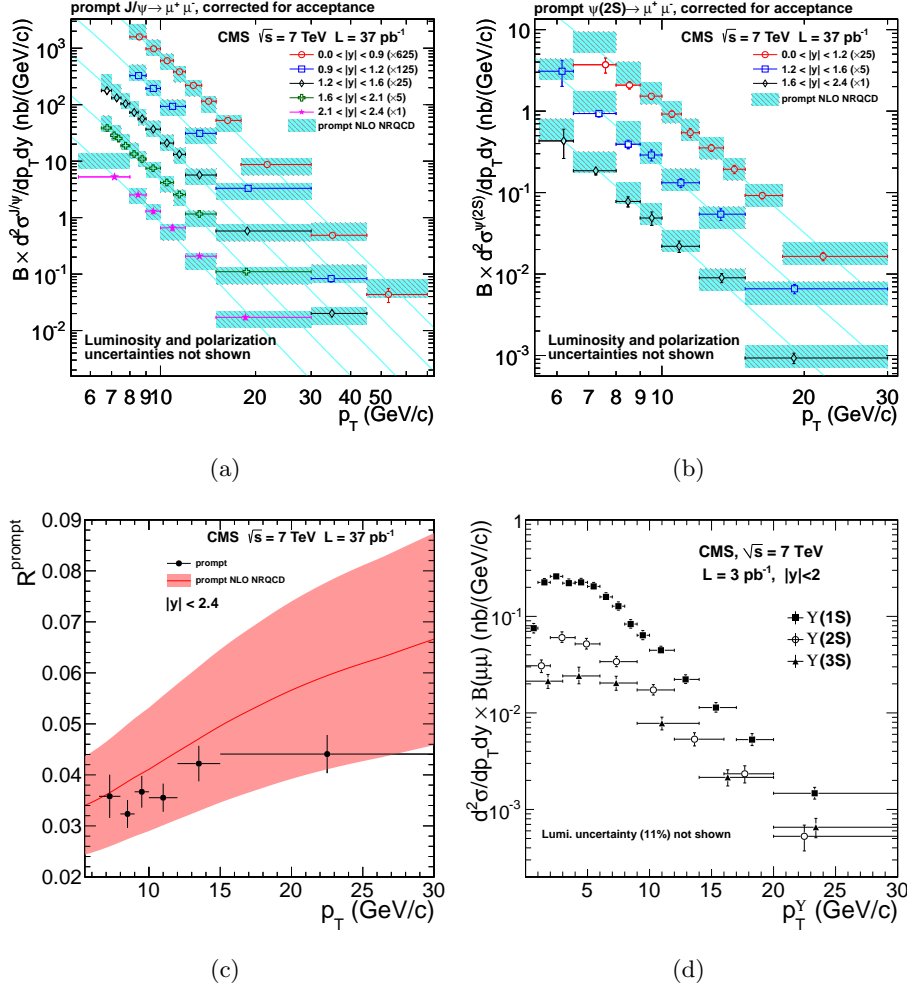


Figure 1.16: Quarkonia results from CMS: prompt  $J/\psi$  and  $\psi(2S)$   $p_T$ -differential cross sections (a,b), ratio of prompt  $\psi(2S)$  over prompt  $J/\psi$  as a function of  $p_T$  (c) and  $\Upsilon(nS)$   $p_T$ -differential cross sections (d). Light blue and red lines/bands correspond to NLO NRQCD calculations (see Section 1.7 for more details).



$J/\psi$  and  $\psi(2S)$  production in a wide  $p_t$  range (from 0.3 to 70 GeV/ $c$ ) and in five rapidity bins (from 0 to 2.4) has been studied and published [66]. The results were compared with prompt NLO NRQCD predictions for both the resonances and the outcome of this comparison is shown in Figure 1.16: the agreement is very good for all the rapidity bins and for the full  $p_t$  range explored.

The fraction of  $J/\psi$  and  $\psi(2S)$  coming from B was also extensively studied: preliminary results are shown in Figure 1.13, while updated values can be found in [66]. The CMS collaboration has also published the ratio between  $\psi(2S)$  and  $J/\psi$  in the case of prompt (see Figure 1.16(c)) and non-prompt production, finding values of the order of 3-5% and a very low dependence with  $p_t$  (in particular for the prompt case) in the region from 5 to 30 GeV/ $c$ . The agreement, for prompt production, with the NLO NRQCD prediction for this observable is good, but the huge theoretical uncertainty band doesn't allow a clear conclusion.

From the  $\Upsilon$  side the collaboration has published  $p_t$  differential cross sections for the three vector states separately in a range  $0 < p_t < 30$  GeV/ $c$  and in two rapidity bins [67]. This publication was based on  $\sim 3pb^{-1}$ , so a little fraction of the overall statistics collected by the experiment. The production cross sections for the three resonances are shown in Figure 1.16(d).

#### 1.6.4 LHCb

The LHCb experiment has measured inclusive, prompt and non-prompt  $J/\psi$  production at  $\sqrt{s} = 7$  TeV at forward rapidity ( $2 < y < 4.5$ ), down to  $p_t=0$  and up to  $p_t=15$  GeV/ $c$  [68]. The differential  $p_t$  cross section results were compared with NLO NRQCD calculations for direct and prompt production [69, 70, 71], with NLO and NNLO\* CSM for direct production [30, 38] and with NLO CEM predictions for prompt production [65]. The results of the comparison are shown in Figure 1.17.

The NRQCD is the favoured approach, even if higher order corrections to the CSM make the model to be not far from the data at high  $p_t$ .

In the same paper the fraction of  $J/\psi$  coming from B-hadrons was measured (see Figure 1.18): this result is by now the best estimate of this fraction for forward rapidities at the LHC and it will be used in Chapter 4 Section 4.10.

The LHCb collaboration has also reported on a very significant observation:  $J/\psi$  pair production in  $pp$  collisions at  $\sqrt{s} = 7$  TeV [72]. This process is considered as a good observable to discriminate among the CSM and the NRQCD since the predictions on the cross section for such a process are very different in the two approaches. The present statistical and systematical uncertainties on this measurement are too large to make any kind of conclusion, but with higher statistics this measurement will be extremely helpful in providing informations on the production mechanism.

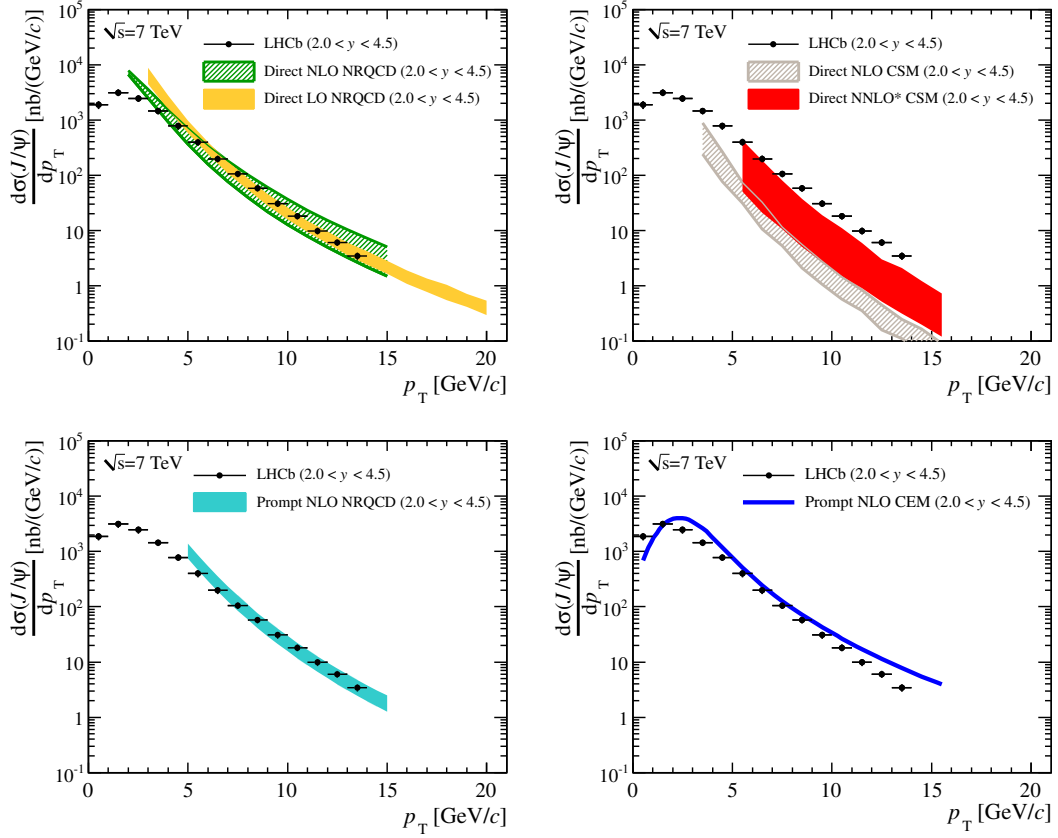


Figure 1.17:  $p_t$  differential cross section for prompt  $J/\psi$  at  $\sqrt{s} = 7$  TeV as measured by the LHCb experiment [68]. The comparison is made with (from top-left to bottom-right): LO [69] and NLO [70] direct NRQCD global fit, NLO and NNLO\* CSM predictions [30, 38], NLO prompt NRQCD global fit [71], NLO CEM prediction [65].

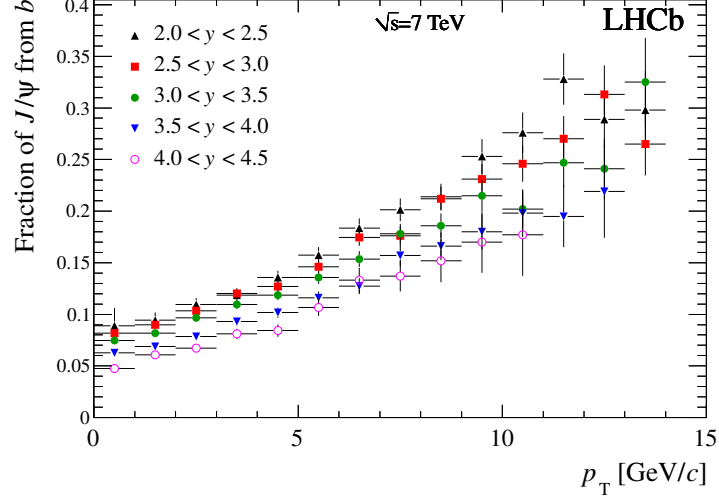


Figure 1.18:  $p_T$ - and  $y$ -differential fraction of  $J/\psi$  coming from B-meson decays as measured by the LHCb experiment [68].

## 1.7 Recent theoretical results on quarkonium production

In the last few years many theoretical efforts were meant to the calculation of the production cross section at higher order in  $\alpha_s$ . In the CSM the difference between predictions at LO and NLO proved to be very large and going at the NNLO\* level other big effects are introduced, putting the model in better agreement with data with respect to the LO case. For the NRQCD approach the differences between LO and NLO showed to be less important.

The new set of data put on the market by the LHC experiments offer new theoretical opportunities: before the LHC era the normal approach was to fit Tevatron results (the most accurate at that time), to extract the non-perturbative matrix elements and then apply these estimations for the prediction of different observables. With the high accuracy of the LHC data, a new global fit was performed very recently in order to estimate in a more accurate way the color octet matrix elements [73].

The result of this global fit is reported in Figure 1.19 and 1.20, together with the CSM prediction in all the cases. Data from LHC, Belle, Tevatron Run I and Run II, HERA Run I and Run II, RHIC and LEP II were used, for a total of 194 points. Experimental data are well described by NLO NRQCD, while NLO CSM predictions fail by 1-2 orders of magnitude for hadroproduction and even more for photoproduction. In the

case of photoproduction, the inclusion of resolved photons in the calculation reconciles HERA data with NRQCD (see the discrepancy for the case of LO in Section 1.5). Furthermore, the  $z \rightarrow 1$  crisis is reduced thanks to the strong cancelation between two newly calculated octet terms.

In contrast with the LO analysis reported in Section 1.5, DELPHI data tend to systematically overshoot the NLO NRQCD result.

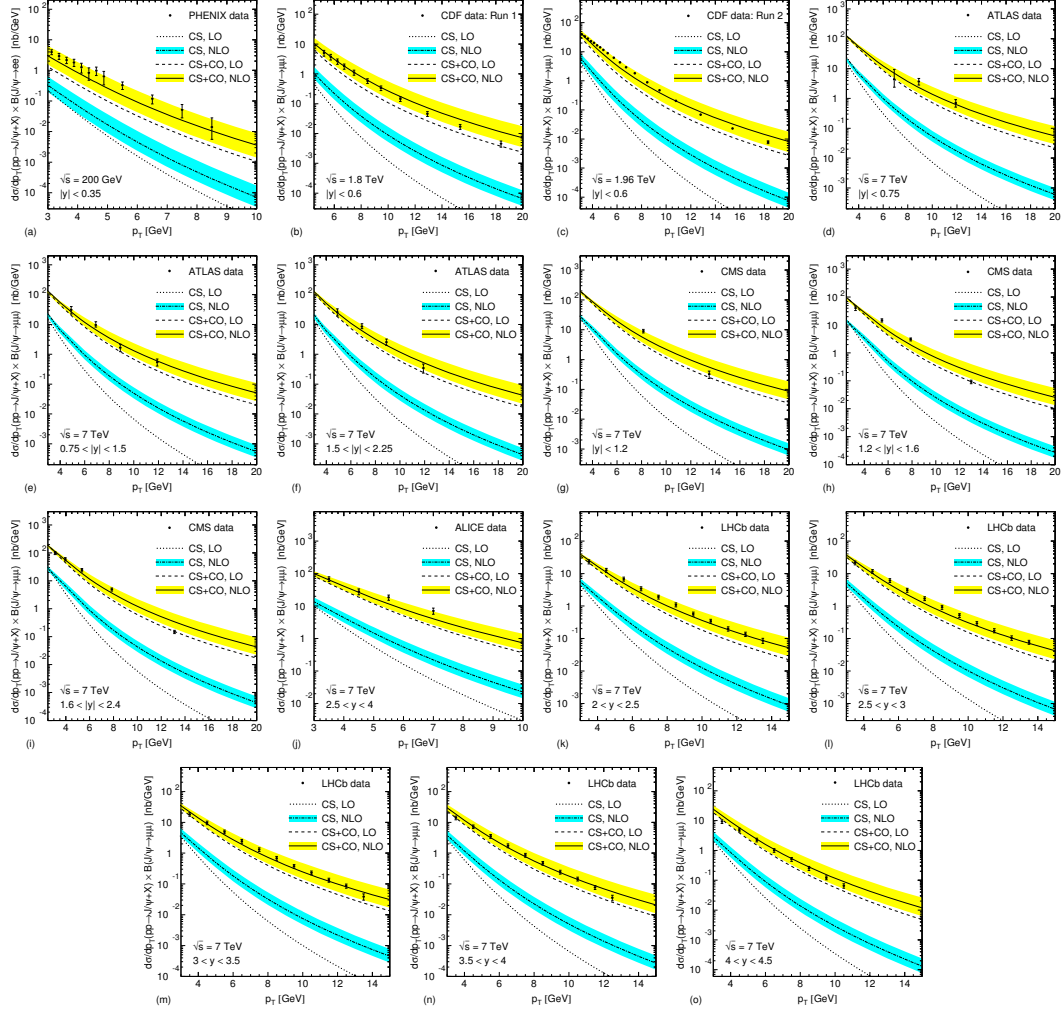


Figure 1.19: Global NLO NRQCD fit to the most accurate experimental data on  $J/\psi$  production. The comparison between LHC data and the theoretical calculations is shown.

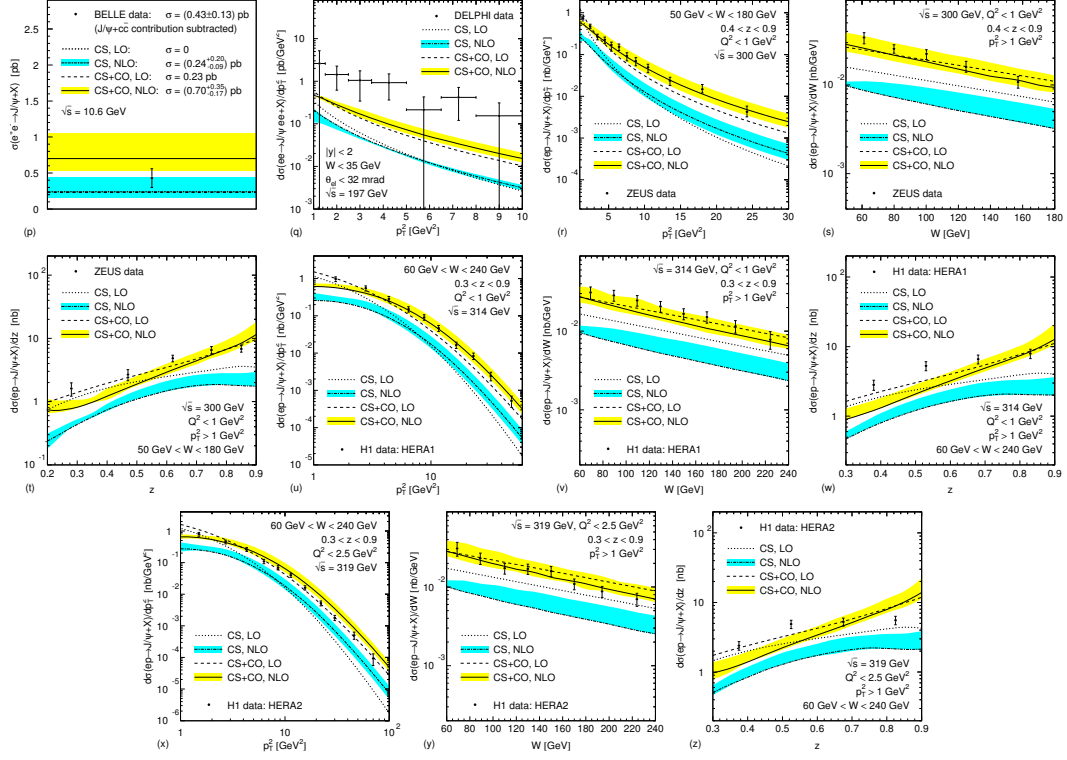


Figure 1.20: Global NLO NRQCD fit to the most accurate experimental data on  $J/\psi$  production. The comparison between non-LHC data and the theoretical calculations is shown.

## 1.8 Quarkonium in heavy ions collisions

As described so far, quarkonia are an important benchmark for QCD studies because they allow to explore all the QCD energy regimes. They are therefore studied in hadron-hadron, lepton-hadron and lepton-lepton collisions, offering a powerful tool for a deeper understanding of elementary particle interactions.

In addition to this, they are also one of the most important probes for the phase transition from hadronic matter to a plasma of free quarks and gluons, the quark-gluon plasma (QGP). This phase transition is experimentally studied through heavy ions collisions [74]. In this section a brief explanation of what is QGP, of why it is studied making use of heavy ions collisions and of the importance of quarkonia for this study is carried out.

### 1.8.1 Quark-Gluon Plasma

One of the most important features of strong interactions is confinement. Theoretical results from lattice gauge theory indicate that when their distance is comparable to the size of the hadron, the quarks interact with an effective strength which grows approximately linearly with the spatial distance: this is the origin of quarks confinement. However, in a large system with sufficiently high energy density ( $\sim 1 \text{ GeV/fm}^3$ ), the hadrons overlap and get squeezed so tightly that their constituents are free to roam the system without being confined inside baryons and mesons. Moreover, due to the asymptotic freedom, if the energy density becomes very large, the interaction between the elementary constituents becomes weak: the formed system of deconfined quarks and gluons is called Quark-Gluon Plasma [75].

The energy density conditions leading to the QGP formation are expected to have taken place in the early universe, few micro-seconds after the Big-Bang, as the system cooled down from the initial temperature of about  $10^{19} \text{ GeV}$  to the temperature of about  $200 \text{ MeV}$ , when the nuclei formation started. Nowadays, energy densities of the order of  $1 \text{ GeV/fm}^3$  could still be found in astrophysical objects, such as neutron stars, supernova explosions leading to neutron stars formation and collisions of black holes and neutron stars. For these reasons the study of the QGP is of great interest not only in particle physics, but also in astrophysics and cosmology.

### 1.8.2 Heavy ions collisions

The formation of the QGP requires extreme conditions of energy density, which can be re-created in laboratory through nucleus-nucleus collisions [75]. The process of multiple collisions occurring between the constituent nucleons allows in fact to deposit a large amount of energy in a small region, which is the fundamental requirement for the onset of deconfinement.

Soon after the collision of the two nuclei, the energy density may be sufficiently high to allow the formation of the QGP and, if the system reaches the thermal equilibrium, the subsequent evolution will follow the laws of hydrodynamics. As the system expands, its temperature drops down and the hadronization takes place: once below the freeze-out temperature, the hadrons do not interact anymore and stream out of the collision region.

The strong interactions among the partons and hadrons before freeze-out wipe out most of the informations about their original production processes. Extracting informations

about the hot and dense early collision stage thus requires to exploit features which are either established early and survive the rescattering and collective expansion or can be reliably back-extrapolated. Correspondingly, one classifies the observables into two classes: early and late signatures [75]. The abundances and spectra of hadrons made of light quarks ( $u$  and  $d$ ) belong to the latter category and can provide useful information on the hadronization and freeze-out of the collision. On the other hand, thermal photons produced in the plasma and heavy flavors and quarkonia constitute early probes of the medium.

### 1.8.3 Probing the QGP through quarkonium

The study of quarkonium production in heavy-ion collisions represents one of the most powerful methods to probe the nature of the medium [76]. The quark and anti-quark in the quarkonium states are bound by energies of the order of few hundred MeV, a value comparable to the mean energies of the plasma: this implies a large probability for quarkonium breakup.

When the quarkonium is immersed in the QGP, the presence of the quarks, anti-quarks and gluons affects the  $q\bar{q}$  system. On one hand, the quark matter alters the string tension  $b$  in Eq. 1.1 between  $q$  and  $\bar{q}$ , which vanishes at the onset of deconfinement. On the other hand, the presence of quark matter leads to the rearrangement of the densities of quarks, antiquarks and gluons around the heavy quark pair, which results in a screening of the Coulombic part of the potential. The effect of this screening is to modify the long-range interaction into a short-range Yukawa type one, with the range given by the Debye screening length  $\lambda_D$ , which decreases when the temperature increases.

At high temperatures, the range of the attractive interaction becomes so small as to make it impossible for the  $q\bar{q}$  pair to form a bound state. When this happens, the  $q\bar{q}$  system dissociates into a separate  $q$  and  $\bar{q}$  in the plasma, which subsequently hadronize by combining with light quarks.

Since the binding energy and the corresponding dimensions are different for different resonances, it is expected that the less tightly bound states melt at lower temperatures. In particular, the present understanding is that while the excited states are dissociated just above the critical temperature  $T_c$ , the fundamental 1S states melt far above that value [77], as shown in Table 1.3 (although it is worth noting that the uncertainties are large and previous calculations predict lower values). The dissociation of specific resonances can thus be used as a measurement of the QGP temperature.

State	$J/\psi(1S)$	$\chi_c(1P)$	$\psi(2S)$	$\Upsilon(1S)$	$\chi_b(1P)$	$\Upsilon(2S)$	$\chi_b(2P)$	$\Upsilon(3S)$
$T_d/T_c$	2.10	1.16	1.12	$> 4$	1.76	1.60	1.19	1.17

Table 1.3: Quarkonium dissociation temperatures in the screening theory framework. From [77].

The description of quarkonia dissociation has been improved by finite temperature lattice studies, which allow a direct spectral analysis. The results, until now indicative since they depend on the model simulated on the lattice (see Section 1.3.2), support the sequential suppression scenario and the late dissociation of the 1S states, as can be seen in Figure 1.21.

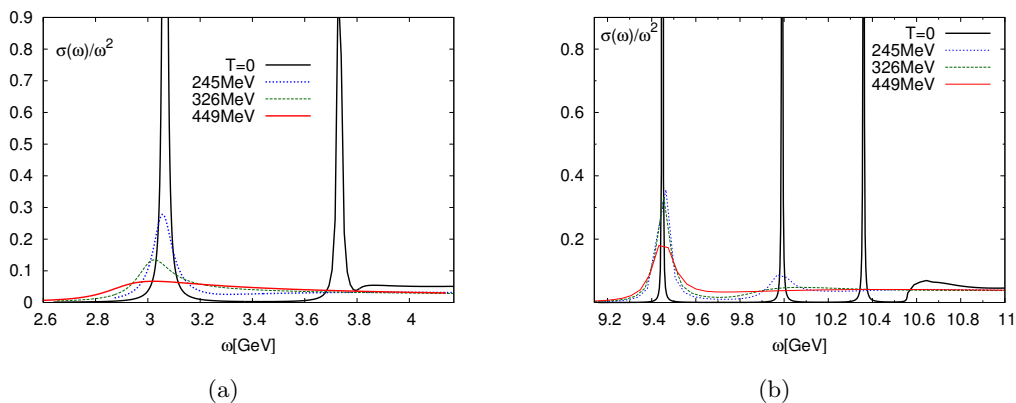


Figure 1.21: Charmonium (a) and bottomonium (b) spectral functions for different temperatures of the QGP calculated with a complex potential model simulated on lattice (from [78])

## Experimental results

Experimentally, the information on the suppression mechanism can be extracted from the distribution of quarkonium yields as a function of the collision centrality: the yields are in fact expected to drop in central collisions, when the number of interacting nucleons is high enough to reach temperatures above the threshold for deconfinement. This information is quantified through the estimation of the so-called nuclear modification factor ( $R_{AA}$ ) which is the ratio of the yield collected in nucleus-nucleus collisions normalized with a reference yield obtained in no-QGP conditions (e.g. in case of hadron-hadron collisions). Another indicator used is the  $R_{CP}$  (central to peripheral nuclear



modification factor), that is similar to the  $R_{AA}$ , but with the normalization to the yield measured in peripheral collisions (which are not expected to lead to deconfinement). Quarkonia suppression in a hot and dense medium relies on rather solid theoretical basis, but the direct comparison of theory with data is complicated by the presence of concurrent or alternative mechanisms which can blur the picture, such as:

- cold nuclear matter effects affecting the quarkonia yield in both the initial state (e.g. shadowing of the Parton Distribution Functions in the nucleus) and the final state (nuclear absorption); these effects can be studied in nucleon-nucleus collisions, where the deconfined phase is not expected to be formed, and properly taken into account in the analysis of data;
- quarkonia suppression in a pure hadronic medium, by the so-called hadronic comovers;
- quarkonia regeneration phenomena due to the statistical recombination of  $q\bar{q}$  pairs emerging from the medium (expected to be more and more important when the center of mass energy of the collision increases since more and more heavy quarks are produced).

The status of charmonium suppression studies before the advent of the LHC startup is summarized in Figure 1.22. The fixed target experiments NA50 and NA60 at the SPS have studied  $J/\psi$  suppression in Pb-Pb and In-In collisions at  $\sqrt{s_{NN}} = 19$  GeV [79, 80], while the PHENIX experiment at the Relativistic Heavy Ion Collider (RHIC) have exploited, with the same purpose, Au-Au collisions at  $\sqrt{s_{NN}} = 200$  GeV [81].

The situation before 2010 could be summarized as follows:

- anomalous suppression (*i.e.* above the Cold Nuclear Matter effects) is observed in central Pb-Pb collisions at SPS and Au-Au collisions at RHIC;
- the magnitude of the anomalous suppression is surprisingly system- and  $\sqrt{s}$ -independent when expressed as a function of  $dN_{ch}/d\eta|_{\eta=0}$
- PHENIX finds more suppression (not corrected for CNM) at forward rapidity with respect to mid-rapidity [81].

A possible explanation of the second item involves “coalescence” or “recombination” models: due to the high number of  $c\bar{c}$  pairs ( $\gtrsim 10$ ) produced in a single central collision at RHIC, the quark of one pair can combine with the anti-quark of another in order to re-form a  $J/\psi$ . Qualitatively, this also could explain the lower suppression at

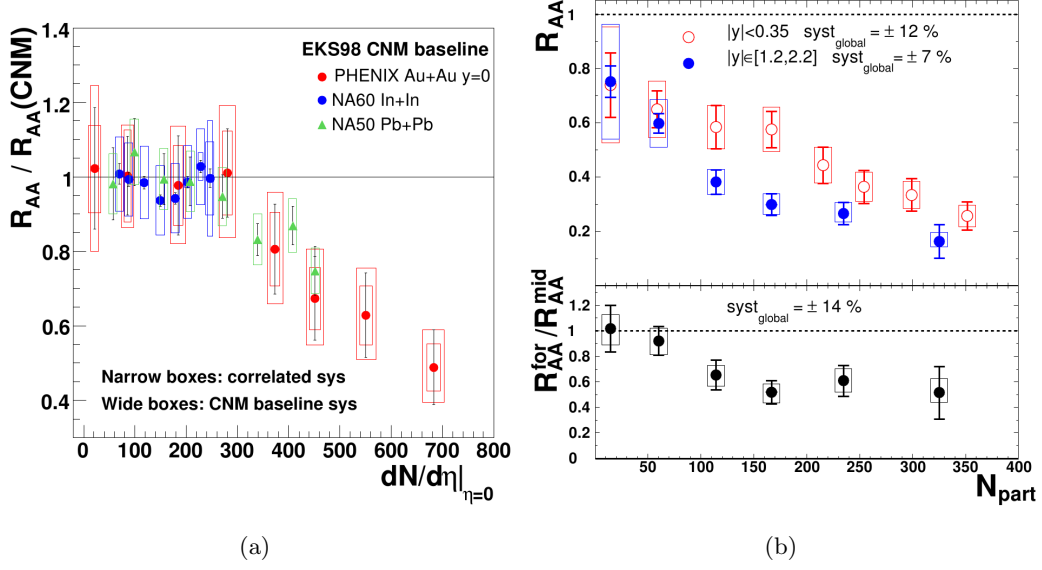


Figure 1.22:  $J/\psi$  suppression pattern before the LHC startup. (a)  $R_{AA}$  factor (above cold nuclear matter effects) as a function of the particle multiplicity for NA50 [79], NA60 [80] and PHENIX [81]. (b)  $R_{AA}$  factor as a function of the number of participant from PHENIX at mid- and forward-rapidity.

mid-rapidity, where the number of  $c\bar{c}$  pairs is higher. Alternatively, the higher suppression at forward rapidity could be due to cold nuclear matter effects: gluon shadowing parameterizations are in fact poorly constrained by data and further saturation effects are not excluded.

The start of the LHC heavy ions program took place by fall 2010, when the first Pb-Pb collisions at the unprecedented energy of  $\sqrt{s_{NN}} = 2.76$  TeV were delivered to the three experiments participating to the data taking: ALICE, ATLAS and CMS. A new run was then provided one year later at the same energy, but with higher luminosity. Results on quarkonium suppression were presented by the beginning of spring 2011 [82, 83, 84].

Again three points emerge from the results obtained so-far:

- the magnitude of the  $J/\psi$  suppression is less important at LHC with respect to RHIC at forward rapidity, while at mid-rapidity the situation seems to be the opposite. The first conclusion is clear by looking at Figure 1.23(a) where the comparison of ALICE's and PHENIX's results at forward rapidity is shown. The

second conclusion can be inferred from Figure 1.23(c), where the comparison between CMS and PHENIX at mid-rapidity is shown: in this case it is important to underline that the  $J/\psi$  sample collected by CMS has a transverse momentum higher than 6.5 GeV/ $c$  and so a direct comparison of the results of the two experiments is not straightforward;

- as a consequence at the LHC the results show a more important suppression at mid-rapidity than at forward, as also shown in Figure 1.23(b), where the comparison of ALICE and ATLAS results is shown. Again in this case, a different  $p_t$  is assessed by the two experiment and a direct comparison is not completely correct;
- the 2S and 3S resonances of bottomonium are significantly suppressed at the LHC, as the CMS study shown in Figure 1.23(d) testify.

After the first run of heavy ions at the LHC the overall picture about quarkonium suppression is even more confused than what was the case after RHIC results. More and more data are needed to achieve better measurement and p-Pb collisions are needed to assess cold nuclear matter effects.

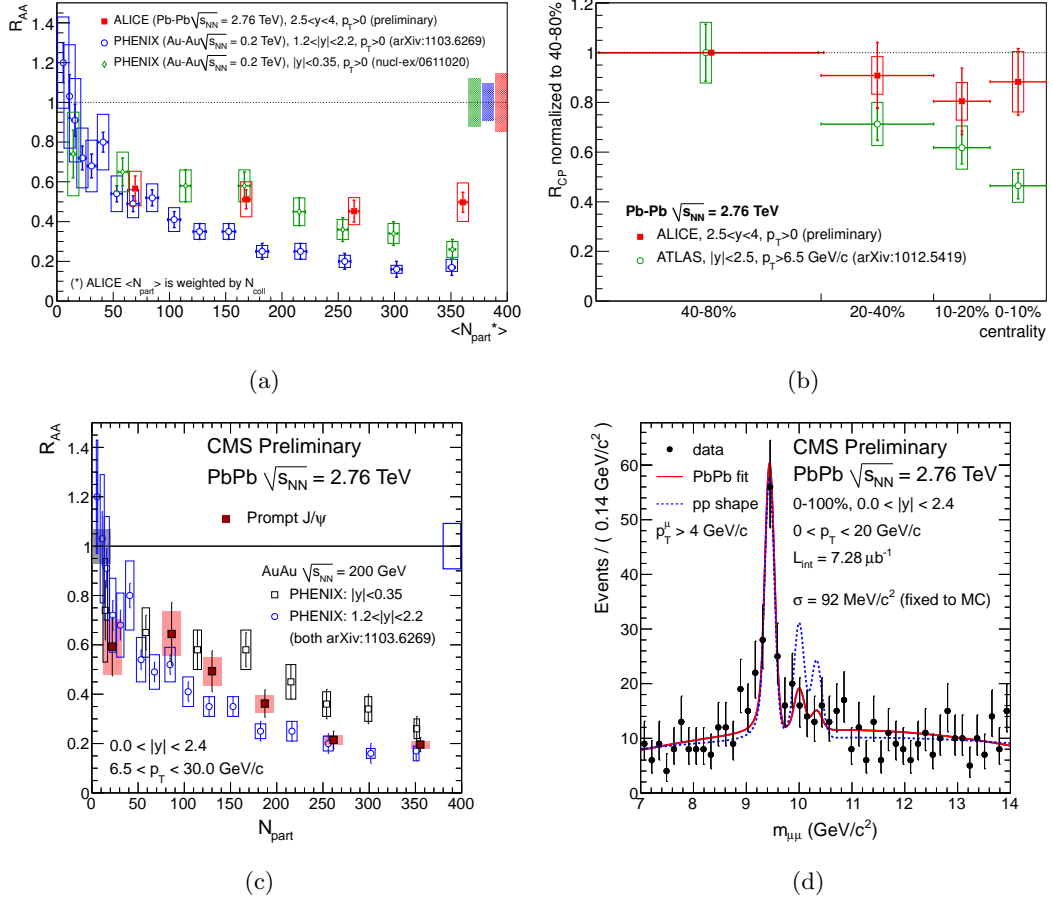


Figure 1.23: LHC first results on quarkonium suppression. (a)  $J/\psi$   $R_{AA}$  at forward rapidity from ALICE compared to PHENIX measurements at forward and midrapidity. (b)  $J/\psi$   $R_{CP}$  from ALICE compared with ATLAS' result. (c)  $J/\psi$   $R_{AA}$  at midrapidity from CMS compared to PHENIX. (d) 2S and 3S bottomonium states' suppression: the two peaks in the invariant mass for  $pp$  collisions normalized to the PbPb yield are suppressed in the invariant mass plot for PbPb collisions.



## Chapter 2

# Quarkonium polarization: theoretical concepts and experimental results

Polarization is one of the most interesting aspects of quarkonium production: the rather simple prediction on this observable provided by NRQCD at LO was ruled out by the results of CDF and this failure prompted many theoretical efforts in the last ten years. CSM at higher orders in  $\alpha_s$  proved to accomodate better Tevatron results on polarization, but still suffers when trying to describe the production cross sections, especially at low  $p_t$ . Very recently, the inclusion of higher order corrections in the NRQCD approach tend to mitigate the striking discrepancy observed at LO and the awaited new experimental results from LHC, as the one described in this thesis, are expected to solve this long-standing dilemma.

In order to give the necessary background for the comprehension of polarization studies, Section 2.1 provides a brief introduction to the concept of spin, while in Section 2.2 the angular distribution of dileptons coming from the decay of a quarkonium state is calculated by first principles, to motivate why the study of this distribution gives informations about the degree of polarization of the mother particle. In the following Section 2.3 a definition of the reference frames used for such studies is given, while in Section 2.4 the polarization parameters' phase-space is discussed. The identification of frame-invariant polarization quantities is reported in Section 2.5 and some experimental aspects of the quarkonium polarization study are discussed in Section 2.6. The last Section 2.7 is devoted to the comparison between past experimental results and

theoretical predictions.

The content of this chapter is a personal and partial adaptation of the topics elaborated in [32, 85, 86, 87] and references therein.

## 2.1 Vector particle's polarization

The polarization measures the degree to which the spin of a given particle is aligned with respect to a chosen axis. It is therefore a characteristic of the particle and of the particular process responsible for its production.

The spin is an intrinsic quantum number of each particle, and can be specified in terms of the total spin number ( $s$ ) and of its third component with respect to a given  $z$ -axis ( $s_z$ ); the algebra of the spin is analog to that of the orbital angular momentum so that one can depict the spin as a vector in the usual 3D space and  $s_z$  like its projection (quantized) along the  $z$ -axis. Moreover, since the algebra is the same, one can define the “total” angular momentum operator  $\vec{J}$  as:

$$\vec{J} = \vec{L} + \vec{S}$$

where  $\vec{L}$  and  $\vec{S}$  are the corresponding orbital angular momentum and spin operators. Its eigenvalues  $j$  define the possible total angular momentum states and can assume all the integer-spaced values in the range:

$$|l - s| < j < l + s$$

where  $l$  are the eigenvalues of the  $\vec{L}$  operator.

Vector mesons are spin-1 states and their mass different from zero allows three possible values for the third component of the spin: +1,0,-1. In the following we will consider the case of the  $\psi$  and  $\Upsilon$  states which have  $l=0$  and, therefore,  $j=1$ . From the angular momentum point of view a quarkonium system can thus be specified with the notation:

$$|\Psi\rangle = |j, j_z\rangle = |1, j_z\rangle.$$

and, considering the three possible  $j_z$  values, the expansion in the angular momentum basis can be written as:

$$|\Psi\rangle = b_{+1} |1, +1\rangle + b_0 |1, 0\rangle + b_{-1} |1, -1\rangle, \quad (2.1)$$

where  $b$  are the eigenvalues corresponding to each magnetic sub-state.

If  $j_z = \pm 1$  the particle is defined “*transversely* polarized”, while if  $j_z = 0$  the polariza-

tion is “*longitudinal*”<sup>1</sup>.

If the spin-alignment measurement is carried out on a large number of particles, the result will be that  $\xi_L$  of them are longitudinally polarized and  $\xi_T$  are transversely polarized, where:

$$\xi_L = \frac{\sigma_L}{\sigma_{TOT}} \quad \xi_T = 1 - \xi_L = \frac{\sigma_T}{\sigma_{TOT}}. \quad (2.2)$$

From the experimental point of view, the polarization of a particle  $|\Psi\rangle$  is extracted by measuring the angular distribution of its decay products, since the spin state of  $|\Psi\rangle$  affects this distribution. More details on this aspect are given in the following section, examining the case of a two-body decay which is the simplest from the mathematical point of view and the most interesting from the point of view of quarkonia.

## 2.2 Two-body decay: angular distribution

The angular distribution of the particles coming from the decay of a mother  $|\Psi\rangle$  can be expressed in terms of the eigenvalues  $b$  in Eq. 2.1. Therefore the study of the angular asymmetries of the decay products can give informations on the polarization of  $|\Psi\rangle$ .

Let’s start from a process which produces a  $|\Psi\rangle$  state as in Eq. 2.1. The momentum of the  $\Psi$  in the collision rest frame defines<sup>2</sup> the direction  $z$  and, in the  $\Psi$  rest frame, the two daughter particles (from now onwards two muons,  $\mu^+$  and  $\mu^-$ ) back-to-back momenta define the  $z'$  axis. The total angular momentum state can be defined in the following way:

- $|\Psi : 1, m\rangle$  before the decay and with respect to the  $z$  axis;
- $|\mu^+ \mu^- : 1, l = m\rangle$  after the decay and with respect to the  $z$  axis.  $l = m$  because of total angular momentum conservation;
- $|\mu^+ \mu^- : 1, l' = \pm 1\rangle$  after the decay and with respect to the  $z'$  axis.  $l' = \pm 1$  because the helicity conservation for massless fermions<sup>3</sup> in the QED process  $\Psi \rightarrow \gamma^* \rightarrow \mu^+ \mu^-$  forces the di-muon system to be, as the photon, transversely polarized.

---

<sup>1</sup>The reason for such a denomination has to be found in QED, where the photon properties (massless vector particle with  $s_z = \pm 1$ ) imply the transversality of the electro-magnetic wave.

<sup>2</sup>This definition of the  $z$ -axis corresponds to the “helicity” frame (see Section 2.3), but the derivation holds for every definition.

<sup>3</sup>Here the  $\mu$  are not massless, but their mass is negligible with respect to that of the  $\Psi$  state and, therefore, to the virtuality of the  $\gamma^*$ .



The notation is also shown in Figure 2.1.

The target of this calculation is to express the known  $|\mu^+\mu^- : 1, l' = \pm 1\rangle$  state as a

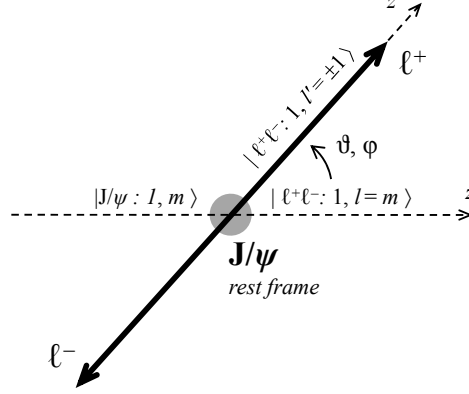


Figure 2.1: Schematic picture of the quarkonium decay into two leptons. The angular notation used in the text is also reported with the ket notation. The  $J/\psi$  case is shown, but exactly the same kinematics are valid for all the vector  $nS$  quarkonium states.

superposition of eigenstates  $|\mu^+\mu^- : 1, l\rangle$  of the operator  $J_z$ . This is feasible exploiting the rotation operator, commonly used in angular momentum theory.

A generic rotation in three dimensions from a set of axes  $(x, y, z)$  to another set  $(x', y', z')$  can be indicated with  $R(\alpha, \beta, \gamma)$ , where  $\alpha$ ,  $\beta$  and  $\gamma$  are the Euler angles. An eigenstate  $|J, M'\rangle$  of  $J_{z'}$  can then be expressed as a superposition of eigenstates  $|J, M\rangle$  of  $J_z$  through the transformation:

$$|J, M'\rangle = \sum_{M=-J}^J \mathcal{D}_{MM'}^J(R) |J, M\rangle. \quad (2.3)$$

The complex rotation matrix elements  $\mathcal{D}_{MM'}^J$  can be expressed in terms of the real reduced matrix elements  $d_{MM'}^J(\beta)$ :

$$\mathcal{D}_{MM'}^J(\alpha, \beta, \gamma) = e^{-iM\alpha} d_{MM'}^J(\beta) e^{iM'\gamma}, \quad (2.4)$$

where

$$d_{MM'}^J(\beta) = \sum_{t=\max(0, M-M')}^{\min(J+M, J-M')} (-1)^t \cdot \mathcal{K}(t) \cdot \left(\cos \frac{\beta}{2}\right)^{2J+M-M'-2t} \cdot \left(\sin \frac{\beta}{2}\right)^{2t-M+M'} \quad (2.5)$$

$$\text{and } \mathcal{K}(t) = \frac{\sqrt{(J+M)! (J-M)! (J+M')! (J-M')!}}{(J+M-t)! (J-M'-t)! t! (t-M+M')!}.$$

Eq. 2.4 and 2.5 are not straightforward, but they are a general result of the quantistic angular momentum treatment: more details and the derivation of the expressions can be found in [87].

In the specific case under study, the transformation has to rotate the axis  $z$  to coincide with  $z'$ : this can be achieved parametrizing the rotation with just one angle, but, in order to be general, the matrix in Eq. 2.4 can be used with the substitutions  $\beta = \theta$  and  $\alpha = -\gamma = \phi$ . In this way we can express the angular di-lepton state in the following way:

$$|\mu^+\mu^- : 1, l'\rangle = \sum_{l=0,\pm 1} \mathcal{D}_{ll'}^1(\phi, \theta, -\phi) |\mu^+\mu^- : 1, l\rangle. \quad (2.6)$$

The amplitude of the process  $\Psi(m) \rightarrow \mu^+\mu^-(l')$  is then obtained by making the bracket (i.e. projecting) of the final state in Eq. 2.6 with the initial  $|\Psi : 1, m\rangle$ , after the action of a transition operator  $\mathcal{B}$ :

$$B_{ml'} = \sum_{l=0,\pm 1} \mathcal{D}_{ll'}^{1*}(\phi, \theta, -\phi) \langle \mu^+\mu^- : 1, l | \mathcal{B} | \Psi : 1, m \rangle. \quad (2.7)$$

The  $\mathcal{B}$  operator embeds the dynamics of the transition. From the angular momentum point of view the only constraint to the operator is that it has to conserve its third component in the transition: its action on the  $|\Psi : 1, m\rangle$  state has therefore to be:

$$\langle \mu^+\mu^- : 1, l | \mathcal{B} | \Psi : 1, m \rangle = B\delta_{ml} \quad (2.8)$$

and Eq. 2.7 can be simplified as:

$$B_{ml'} = B\mathcal{D}_{ml'}^{1*}(\phi, \theta, -\phi). \quad (2.9)$$

If now all the possible  $m$  values in the initial state are considered by substituting  $|\Psi : 1, m\rangle$  with the expression in Eq. 2.1, the total  $\Psi \rightarrow \mu^+\mu^-(l')$  amplitude can be obtained:

$$B_{l'} = \sum_{m=0,\pm 1} b_m B\mathcal{D}_{ml'}^{1*}(\phi, \theta, -\phi) = \sum_{m=0,\pm 1} a_m \mathcal{D}_{ml'}^{1*}(\phi, \theta, -\phi). \quad (2.10)$$

The transition probability is obtained by squaring Eq. 2.10 and summing over the unobserved spin alignments ( $l' = \pm 1$ ) of the dilepton system:

$$W(\cos \theta, \phi) \propto \sum_{l'=\pm 1} |B_{l'}|^2. \quad (2.11)$$

To perform this calculation the expressions in Eq. 2.4 and 2.5 have to be used in Eq. 2.10. In particular, with the angles definition adopted, the  $d$  elements can be written as:

$$d_{0,\pm 1}^1 = \pm \sin \theta / \sqrt{2} \quad d_{\pm,\pm 1}^1 = (1 + \cos \theta) / 2 \quad d_{\mp,\pm 1}^1 = (1 - \cos \theta) / 2$$

and Eq. 2.11, with some algebra, assumes the rather simple form:

$$W(\cos \theta, \phi) \propto \frac{\mathcal{N}}{3 + \lambda_\theta} \cdot ( \quad 1 + \lambda_\theta \cos^2 \theta \\ + \lambda_\phi \sin^2 \theta \cos 2\phi + \lambda_{\theta\phi} \sin 2\theta \cos \phi \\ + \lambda_\phi^\perp \sin^2 \theta \sin 2\phi + \lambda_{\theta\phi}^\perp \sin 2\theta \sin \phi ), \quad (2.12)$$

where the different parameters are combinations of the complex numbers  $a_m$ :

$$\begin{aligned} \mathcal{N} &= |a_0|^2 + |a_{+1}|^2 + |a_{-1}|^2, \\ \lambda_\theta &= \frac{\mathcal{N} - 3|a_0|^2}{\mathcal{N} + |a_0|^2}, \\ \lambda_\phi &= \frac{2\text{Re}[a_{+1}^* a_{-1}]}{\mathcal{N} + |a_0|^2}, \\ \lambda_{\theta\phi} &= \frac{\sqrt{2}\text{Re}[a_0^*(a_{+1} - a_{-1})]}{\mathcal{N} + |a_0|^2}, \\ \lambda_\phi^\perp &= \frac{2\text{Im}[a_{+1}^* a_{-1}]}{\mathcal{N} + |a_0|^2}, \\ \lambda_{\theta\phi}^\perp &= \frac{-\sqrt{2}\text{Im}[a_0^*(a_{+1} + a_{-1})]}{\mathcal{N} + |a_0|^2}. \end{aligned} \quad (2.13)$$

Eq. 2.12 is the most general decay distribution, but can be further simplified taking into account that the last two terms are unobservable in quarkonium hadroproduction. These terms introduce an asymmetry with respect to the reaction plane, identified by the beam axis and by the  $\Psi$  direction in the collision rest frame ( $z$ ). The asymmetry can be observed when the  $z$  axis is well defined event-by-event, but in hadroproduction it should be referred not to the colliding hadron direction, but to the colliding parton direction, which of course is unobservable. In this sense the last two terms in Eq. 2.12 are averaged when the  $\Psi$  state is produced from hadron-hadron collisions and, therefore, they vanish.

As discussed in the previous section, the polarization depends on the particle and on the production process. Different processes can have different quantization axis for the spin and, therefore, the angular distribution referred to a fixed  $z$ -axis is the weighted sum of the angular distributions relative to each production process. To translate this into formulae:

$$W(\cos \theta, \phi) = \sum_{i=1}^n f^{(i)} W^{(i)}(\cos \theta, \phi) \quad (2.14)$$

where  $W(\cos \theta, \phi)$  is now the observed angular distribution,  $i$  runs over the  $n$  subprocesses contributing to the inclusive production, the numbers  $f^{(i)}$  weight each contribution and  $W^{(i)}(\cos \theta, \phi)$  are the angular distributions for each sub-process (written as in Eq. 2.12). Ordering the terms of the sum in Eq. 2.14, one can define the new polarization parameters  $X = \lambda_\theta, \lambda_\phi$  and  $\lambda_{\theta\phi}$  as the weighted average of those relative to a specific process:

$$X = \sum_{i=1}^n \frac{f^{(i)} \mathcal{N}^{(i)}}{3 + \lambda_\theta^i} X^{(i)} \bigg/ \frac{f^{(i)} \mathcal{N}^{(i)}}{3 + \lambda_\theta^i} \quad (2.15)$$

and, finally, to obtain the observable angular distribution:

$$W(\cos \theta, \phi) \propto \frac{1}{3 + \lambda_\theta} \cdot (1 + \lambda_\theta \cos^2 \theta + \lambda_\phi \sin^2 \theta \cos 2\phi + \lambda_{\theta\phi} \sin 2\theta \cos \phi). \quad (2.16)$$

The last expression, together with the definitions in Eq. 2.13, represents the main result of the calculation carried out so far, because it shows that the spin alignment of the mother particle  $\Psi$  affects the angular distribution of the two-body decay products. This influence is embedded in the  $\lambda$  parameters, which can be expressed in terms of the coefficients in Eq. 2.1 that define the spin state of the mother particle.

To better understand this point, one can make some examples, assuming for simplicity that only one process contributes to the inclusive production. If the  $\Psi$  is longitudinally polarized, then:

$$b_0 = 1 \quad b_{\pm 1} = 0$$

and the polarization parameters (calculated as in Eq 2.13) are:

$$\lambda_\theta = -1 \quad \lambda_\phi = 0 \quad \lambda_{\theta\phi} = 0.$$

If, on the contrary, the  $\Psi$  is a pure transversely polarized state, one has:

$$b_{0,-1} = 0 \quad b_{+1} = 1 \quad (\text{or, alternatively, } b_{0,+1} = 0, b_{-1} = 1)$$

and the polarization parameters are:

$$\lambda_\theta = +1 \quad \lambda_\phi = 0 \quad \lambda_{\theta\phi} = 0.$$

## 2.3 Reference frames

As discussed in the previous section, the extraction of the polarization parameters  $\lambda$  starts from the definition of two axis:  $z$  and  $z'$ .

The second one is automatically defined by the direction of the  $\mu$  in the quarkonium rest frame, with an orientation that can be conventionally chosen as the versus of the momentum of the positively-charged muon.

The first one can be defined in different ways: in the calculation of the previous chapter it was chosen as the direction of the quarkonium in the collision center of mass frame, but the whole reasoning would have held also with another definition.

As already underlined, the angular distribution in Eq. 2.16 is a weighted average of those corresponding to each sub-process responsible for the formation of the quarkonium; each different sub-processes can favor specific spin-alignment configurations. This means that the measurement of the parameters  $\lambda$  for different definitions of the axis  $z$  can give rather different values which, however, give the same information on the system. From the experimental point of view it is very important to repeat the measurement for different reference systems since the comparison of the results is a powerful way to investigate possible sources of systematical errors.

Three different definitions of the  $z$  axis were adopted in the past for the study of quarkonium hadroproduction:

- **helicity**: it is the one described in the previous section and corresponds to the quarkonium momentum direction in the collision reference frame. It is the most used both in collider and fixed-target experiments;
- **Collins-Soper**: it is defined as the bisector of the angle between the momentum of the first colliding object (e.g. the incoming proton) and the opposite of the momentum of the second colliding object as seen from the quarkonium rest frame [88].
- **Gottfried-Jackson**: it is the direction of the beam in the quarkonium rest frame [89]. This is mostly used in fixed-target experiments, where the beam is only one and the definition is unambiguous.

In Figure 2.2 the three reference frames are shown: the notation reported here will be used for the following considerations.

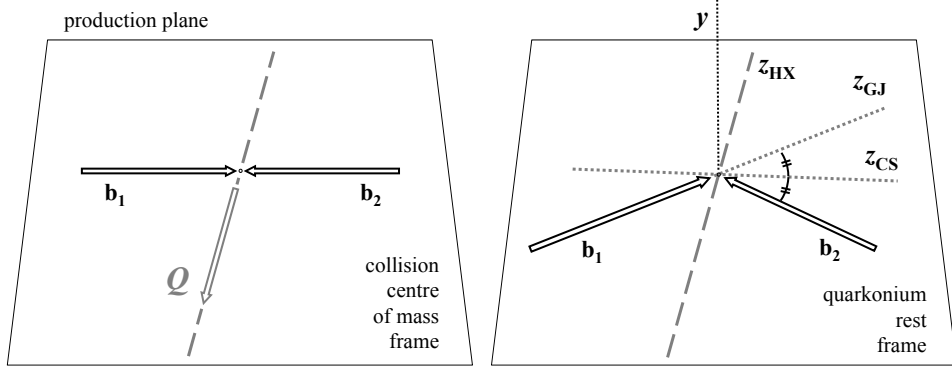


Figure 2.2: Definition of three reference frames, all referred to the production plane (left picture): helicity (HX), Gottfried-Jackson (GJ) and Collins-Soper (CS). The  $x$  axis completes the right-handed frame definition.

## 2.4 Kinematical constraints

It is possible to determine some constraints for the three polarization parameters  $\lambda_\theta$ ,  $\lambda_\phi$  and  $\lambda_{\theta\phi}$ .

From Eq. 2.13, with some simple algebra, the following equalities and inequalities can be derived:

$$\begin{aligned}
 1 \pm \lambda_\phi &= (|a_{+1} \pm a_{-1}|^2 + 2|a_0|^2)/(\mathcal{N} + |a_0|^2) \\
 \lambda_\theta \pm \lambda_\phi &= (|a_{+1} \pm a_{-1}|^2 - 2|a_0|^2)/(\mathcal{N} + |a_0|^2) \\
 |\lambda_{\theta\phi}| &\leq \sqrt{2}|a_0||a_{+1} - a_{-1}|/(\mathcal{N} + |a_0|^2) \\
 |\lambda_{\theta\phi}^\perp| &\leq \sqrt{2}|a_0||a_{+1} + a_{-1}|/(\mathcal{N} + |a_0|^2)
 \end{aligned} \tag{2.17}$$

which imply the following relations among the coefficients:

$$\begin{aligned}
 (1 - \lambda_\phi)^2 - (\lambda_\theta - \lambda_\phi)^2 &\geq 4\lambda_{\theta\phi}^2 \\
 (1 + \lambda_\phi)^2 - (\lambda_\theta + \lambda_\phi)^2 &\geq 4\lambda_{\theta\phi}^{\perp 2}.
 \end{aligned} \tag{2.18}$$

Adding the further condition that the  $\lambda_\theta$  must not exceed 1 in any reference frame, the result is the following set of inequalities:

$$\begin{aligned}
 |\lambda_\phi| &\leq \frac{1}{2}(1 + \lambda_\theta), \\
 \lambda_\theta^2 + 2\lambda_{\theta\phi}^2 &\leq 1, \\
 |\lambda_{\theta\phi}| &\leq \frac{1}{2}(1 - \lambda_\phi), \\
 (1 + 2\lambda_\phi)^2 + 2\lambda_{\theta\phi}^2 &\leq 1 \quad \text{for } \lambda_\phi < -1/3.
 \end{aligned} \tag{2.19}$$

These conditions define an allowed region in the 3D parameters space  $[\lambda_\theta, \lambda_\phi, \lambda_{\theta\phi}]$ : outside this region the angular distribution in Eq. 2.16 becomes negative for some values of  $\cos\theta$  and  $\phi$ , leading to a clearly unphysical result.

The projections of this 3-dimensional allowed region in the 2-dimensional  $[\lambda_\theta, \lambda_\phi]$ ,  $[\lambda_\theta, \lambda_{\theta\phi}]$  and  $[\lambda_\phi, \lambda_{\theta\phi}]$  spaces are shown in Figure 2.3.

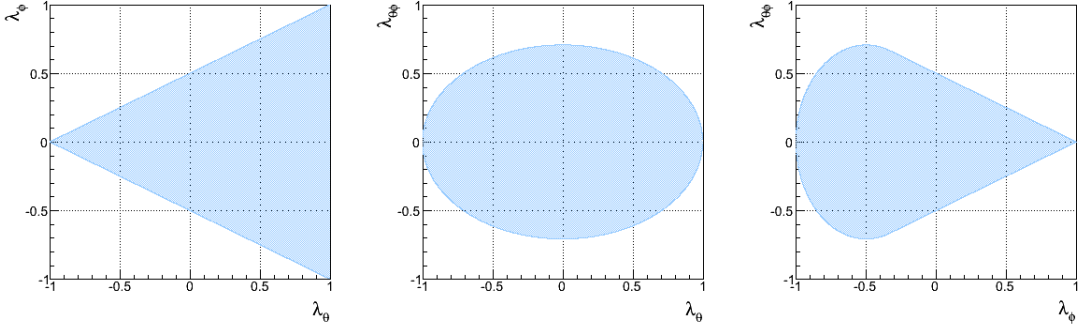


Figure 2.3: Kinematically allowed region for the  $\lambda_\theta$ ,  $\lambda_\phi$  and  $\lambda_{\theta\phi}$  parameters projected in the  $[\lambda_\theta, \lambda_\phi]$  (left),  $[\lambda_\theta, \lambda_{\theta\phi}]$  (middle) and  $[\lambda_\phi, \lambda_{\theta\phi}]$  (right) spaces.

## 2.5 Invariant quantities

All the possible polarization axis are related to the definition of the production plane. It is therefore possible to parametrize the transformation from one reference to another one with a single angle which describes a rotation around the  $y$  axis. The rotation

matrix can be therefore written as:

$$R_y(\delta) = \begin{pmatrix} \cos \delta & 0 & -\sin \delta \\ 0 & 1 & 0 \\ \sin \delta & 0 & \cos \delta \end{pmatrix}, \quad (2.20)$$

where the  $\delta$  angle is the angle between the two polarization axis and, generally, depends on the quarkonium production kinematics<sup>4</sup>.

If this rotation is applied directly to the angular distribution in Eq. 2.16 referred to a certain  $z$  axis, the new distribution referred to the  $\hat{z}$  axis can be obtained. To achieve this change of coordinates it is sufficient to express the unit vector  $\bar{r}$  in the old reference as a function of the new reference:

$$\begin{aligned} \bar{r} &= R_y^{-1}(\delta) \hat{r} \\ &\Downarrow \\ \begin{pmatrix} \sin \theta \cos \phi \\ \sin \theta \sin \phi \\ \cos \theta \end{pmatrix} &= \begin{pmatrix} \cos \delta & 0 & -\sin \delta \\ 0 & 1 & 0 \\ \sin \delta & 0 & \cos \delta \end{pmatrix}^{-1} \begin{pmatrix} \sin \hat{\theta} \cos \hat{\phi} \\ \sin \hat{\theta} \sin \hat{\phi} \\ \cos \hat{\theta} \end{pmatrix}. \end{aligned} \quad (2.21)$$

Solving the system of equations, all the ingredients needed to perform the change of coordinates in the angular distribution are available and the new expression turns out to be:

$$W(\cos \hat{\theta}, \hat{\phi}) \propto \frac{1}{3 + \hat{\lambda}_\theta} \cdot (1 + \hat{\lambda}_\theta \cos^2 \hat{\theta} + \hat{\lambda}_\phi \sin^2 \hat{\theta} \cos 2\hat{\phi} + \hat{\lambda}_{\theta\phi} \sin 2\hat{\theta} \cos \hat{\phi}), \quad (2.22)$$

---

<sup>4</sup>If the rotation is between the helicity and the Collins-Soper axis, the  $\delta$  parameter depends on the momentum of the considered quarkonium system. This dependence can be simply seen through a Lorentz transformation between the two frames and the result turns out to be:

$$\delta_{he \rightarrow CS} = \arccos \frac{mp_L}{m_T p} \Rightarrow \sin 2\delta_{he \rightarrow CS} = \frac{2mp_T p_L E}{p^2 m_T^2},$$

where  $m$ ,  $m_T$ ,  $p_L$ ,  $p_T$  and  $E$  are respectively the mass, the transverse mass ( $m_T = \sqrt{m^2 + p_T^2}$ ), the longitudinal and transverse momenta and the energy of the quarkonium system.



where

$$\begin{aligned}
 \hat{\lambda}_\theta &= \frac{\lambda_\theta - 3\Lambda}{1 + \Lambda} \\
 \hat{\lambda}_\phi &= \frac{\lambda_\phi + \Lambda}{1 + \Lambda} \\
 \hat{\lambda}_{\theta\phi} &= \frac{\lambda_{\theta\phi} \cos 2\delta - 0.5(\lambda_\theta - \lambda_\phi) \sin 2\delta}{1 + \Lambda} \\
 \Lambda &= \frac{1}{2}(\lambda_\theta - \lambda_\phi) \sin^2 \delta - \frac{1}{2}\lambda_{\theta\phi} \sin 2\delta.
 \end{aligned} \tag{2.23}$$

From the last expressions it is straightforward to verify that the quantity

$$\mathcal{F}_{c_1, c_2, c_3} = \frac{(3 + \lambda_\theta) + c_1(1 - \lambda_\phi)}{c_2(3 + \lambda_\theta) + c_3(1 - \lambda_\phi)}, \tag{2.24}$$

where  $c_n$  are real numbers, represents an invariant under every axis transformation. This relation has a key importance from the experimental point of view: if the polarization parameters are determined in more than one frame, then a compatibility check can be performed calculating the invariant quantity for the two frames and verifying if the result turns out to be the same.

## 2.6 Quarkonium polarization: experimental issues

The interest in studying quarkonium polarization is motivated by the need to understand what is the main production process: the available theoretical models make different predictions for this observable (for more details on this point see the next section).

From the experimental point of view, there is another important reason to perform such a measurement. When the integrated and differential cross sections are measured from data, the usual assumption is that quarkonia are not polarized : the Monte Carlo (MC) sample used to extract the detector acceptance is, in fact, obtained simulating unpolarized resonances. If a polarization measurement reveals that the  $\lambda$  parameters are sensibly different from zero, then the assumption made in the MC is not justified and the cross section measurement can be biased. This point will be discussed in more detail in Chapter 4 and is also addressed in Appendix A.

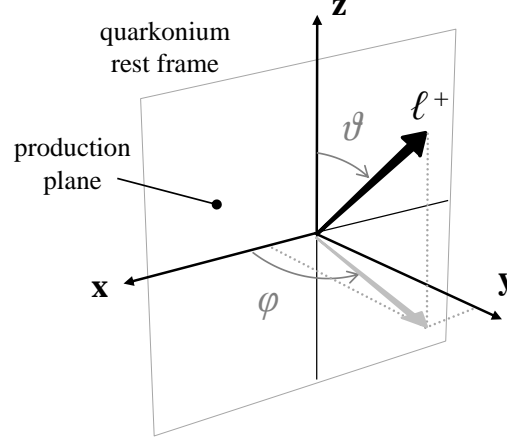


Figure 2.4:  $\theta$  and  $\phi$  angles definition of the positive lepton coming from the quarkonium decay in the  $(x,y,z)$  reference frame.

Despite their crucial importance, the extraction of the  $\lambda$  parameters is not straightforward.

On the one hand, the analysis is intrinsically multi-dimensional, since the two angular variables ( $\theta$  and  $\phi$ ) are usually studied as a function of the quarkonium transverse momentum and sometimes also of its rapidity. This asks for high statistics samples in order to be able to extract the signal (usually from a di-electron or di-muon mass spectrum) in many bins of the different kinematical variables (angular,  $p_t$ , rapidity, etc.). In order to reduce the number of dimensions, many experiments analyzed only part of the full angular distribution in Eq. 2.16: this is possible integrating it over  $\phi$  and studying only the  $\propto (1 + \lambda_\theta \cos \theta)$  part. This approach is in principle correct since it retains the part of the distribution that is directly related to the alignment of the third component of the spin. Nevertheless the extraction of the full angular distribution is more safe, since allows to make checks on different reference frames and makes the comparison between the results from different experiments simpler.

On the other hand, the detector acceptance is a key issue for such an analysis. The definition of the  $z$  axis is related to the quarkonium momentum in the collision rest frame and, as pointed out previously, the production plane is the only one observable in hadroproduction. From Figure 2.4 it is clear that high- $\cos \theta$  values correspond to the kinematical configuration in which the two leptons are aligned with the  $z$  axis. If  $z$  is defined as the quarkonium momentum direction in the collision reference frame (helicity axis), this means that one of the two leptons follows this direction (we call it

$l^\uparrow$ ), while the other one flies in the opposite way (we call it  $l^\downarrow$ ). If the kinematical situation is observed from the laboratory reference frame (corresponding to the collision one in collider experiments), then the  $l^\uparrow$  will have very high momentum (acquired from the mass of the quarkonium and from the boost given by its momentum), while the  $l^\downarrow$  will have quite low momentum (the mass and the boost part contribute here with opposite directions). For a quarkonium with a momentum of roughly  $1.5 \text{ GeV}/c$ , one of the two decaying leptons will have zero momentum and will be therefore undetectable: this means that, for low momentum quarkonium systems, the acceptance will be very low for high values of  $\cos\theta$ . This is clear for the helicity frame, but is also valid for the Collins-Soper one since, as it was discussed in the previous section, the angle between the two frames definition tends to vanish at low  $p_t$  and is zero at zero momentum.

## 2.7 Experimental results on quarkonium polarization and comparison with theory

The NRQCD LO approach was able, in the nineties, to reproduce the  $p_t$  differential cross section for  $J/\psi$ ,  $\psi(2S)$  and  $\Upsilon$ , which were underestimated by CSM at LO by some orders of magnitude. This was possible by including in the production amplitude, on top of the color octet contributions, some Feynman diagrams corresponding to gluon fragmentation (see Figure 1.6(b)), expected to be important for high transverse momenta of the produced quarkonium.

In this processes the fragmenting gluon is expected to be almost on-shell: a massless spin-1 particle is always transversely polarized and, therefore, for parity conservation the produced  $c\bar{c}$  pair will also be transversely polarized. Moreover the long distance terms (see Chapter 1 Section 1.4.3) were not expected to dilute the polarization and, therefore, the simple prediction was that at high  $p_t$  the  $\lambda_\theta$  parameter had to approach +1.

This prediction triggered many experimental works and the comparison between theory and data is a crucial issue in quarkonium physics. In this section the most recent results on  $\psi$  and  $\Upsilon$  polarization are shown, together with the comparison with theoretical predictions at LO and higher. The very last subsection will be devoted to recent theoretical developments, the same described in Chapter 1 Section 1.7, but here seen from the polarization point of view.

### 2.7.1 Results from Tevatron

Data from Tevatron Run I and Run II were used to extract the polarization parameter  $\lambda_\theta$  (also called  $\alpha$ ) as a function of  $p_t$  for prompt  $J/\psi$  and  $\psi(2S)$  production. While for  $\psi(2S)$  errors are too large to draw any clear conclusion, in the  $J/\psi$  case the statistics were sufficient to trigger some interest from the theoretical side.

The CDF collaboration was able to perform the analysis in  $\sqrt{s} = 1.8$  and 1.96 TeV  $p\bar{p}$  collisions at mid-rapidity ( $|y| < 0.6$ ) [90, 91]. The results, obtained for prompt  $J/\psi$  in

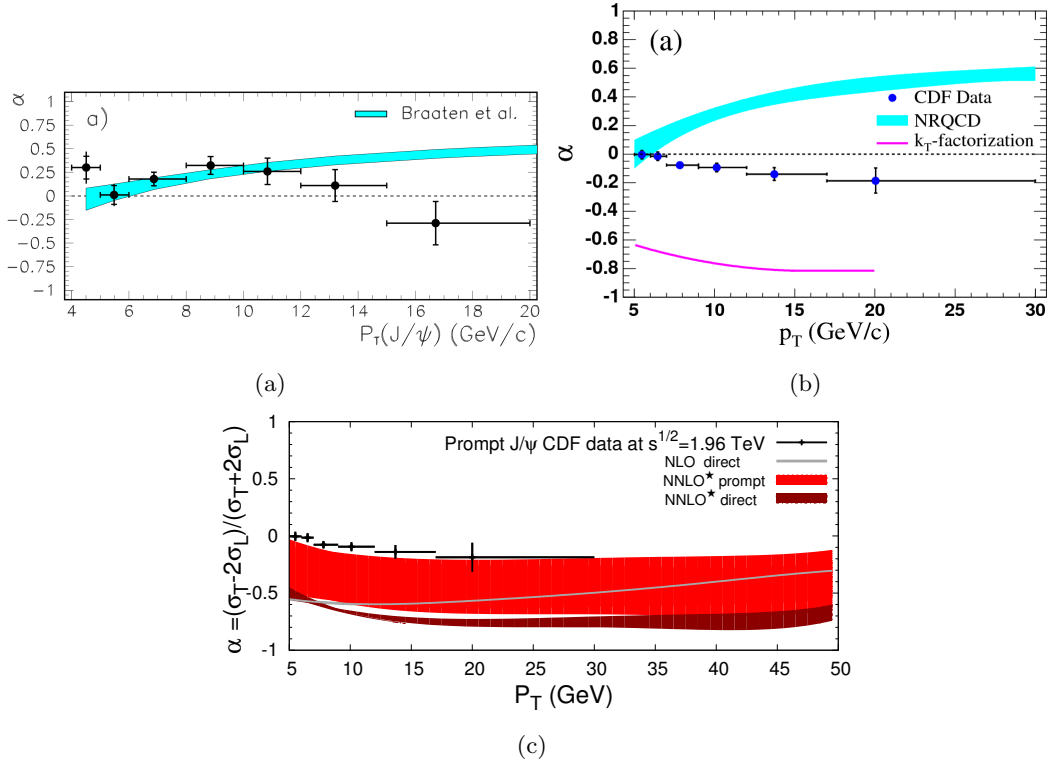


Figure 2.5: Polarization parameter  $\alpha = \lambda_\theta$  in the helicity reference frame as measured by the CDF collaboration for prompt  $J/\psi$  production in  $p\bar{p}$  collisions at  $\sqrt{s} = 1.8$  TeV (a) and  $\sqrt{s} = 1.96$  TeV (b,c) [90, 91]. Light-blue bands are the theoretical LO NRQCD predictions [92], while the purple line corresponds to CSM +  $k_t$ -factorization [93]. The grey line and the red bands in (c) are the CSM NLO and NNLO\* predictions [94].

the helicity reference frame, are shown in Figure 2.5(a) and (b). What is immediately clear is that there is no agreement between the two measurements and, even if they come from slightly different collision energies, this is still a puzzling outcome.

Both results were compared with NRQCD at LO [92] and, in the case of the higher-energy one, also with CSM with  $k_t$ -factorization approach [93]: the data rule out both the predictions at high  $p_t$ , even if the second one has no theoretical uncertainties.

This comparison represented a turning point in the  $J/\psi$  production topic: the apparent failure of NRQCD at LO prompted many theoretical efforts from the CSM side, with the inclusion of NLO and NNLO\* contributions (see also Section 1.5), which proved, despite the very large theoretical uncertainties, to better accommodate the real data, as can be appreciated in Figure 2.5(c).

CDF published also the polarization for  $J/\psi$  coming from the decay of B-mesons [91]. The study was carried out referring the  $z$ -axis to the collision reference frame, since the momentum of the B was not reconstructed. The values are compatible with zero in all the explored  $p_t$  range (from 5 to 30 GeV/c).

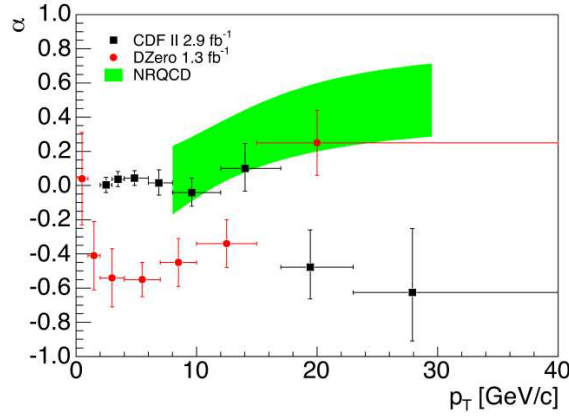


Figure 2.6: Polarization parameter  $\alpha = \lambda_\theta$  in the helicity reference frame as measured by the CDF and D0 collaborations for  $\Upsilon(1S)$  production in  $p\bar{p}$  collisions at  $\sqrt{s} = 1.96$  TeV [40, 95] compared with LO NRQCD [96] (green band).

Both CDF and D0 were also able to extract the  $\lambda_\theta$  parameter for inclusive  $\Upsilon(1S)$  production at  $\sqrt{s} = 1.96$  TeV at mid-rapidity ( $|y_{J/\psi}^{CDF}| < 0.6$  and  $|y_{J/\psi}^{D0}| < 0.4$ ) [40, 95]. The comparison between the two experiments and with LO NRQCD is shown in Figure 2.6. A discrepancy is observed: the trends seen by the two experiments using data collected at the same energy are somehow opposite. Also in this case there is still no clear explanation for such a contradictory result and the outcome of the comparison with theory depends on the set of data considered. The D0 result tends to show a

value of  $\lambda_\theta$  which increases with  $p_t$  and this behaviour is somehow the one expected by LO NRQCD; on the contrary, CDF data tend to favour a decreasing  $\lambda_\theta$  parameter, in agreement with what seen for the  $J/\psi$  case and in strong disagreement with the NRQCD band. In any case a meaningful comparison with theory must rely on more solid experimental results.

The D0 collaboration has also measured  $\Upsilon(2S)$  polarization [95], but the error bands are in this case too large to make any comparison conclusive.

### 2.7.2 Results from RHIC

At RHIC prompt- $J/\psi$  polarization in  $pp$  collisions at  $\sqrt{s} = 200$  GeV was studied by the PHENIX collaboration in two reference frames: helicity and Gottfried-Jackson [43]. Only the  $\lambda_\theta$  parameter was extracted and the result is shown in Figure 2.7. The values are compatible with zero in the whole explored  $p_t$  range, with a hint for a decrease at high  $p_t$ .

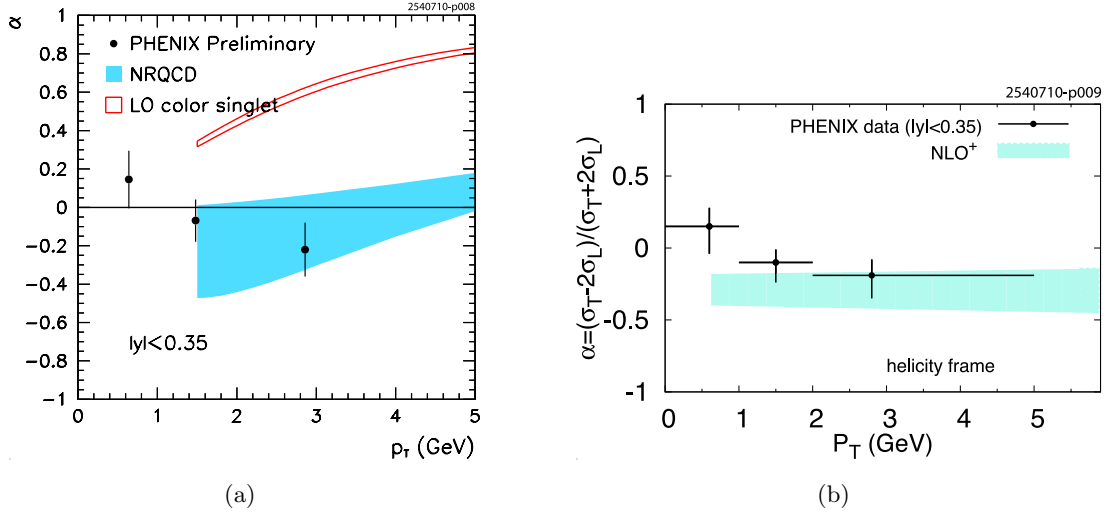


Figure 2.7: Helicity polarization parameter  $\alpha = \lambda_\theta$  as measured by the PHENIX experiment at mid-rapidity in  $pp$  collisions at  $\sqrt{s} = 200$  GeV [43]. (a) comparison with LO CSM and NRQCD for prompt  $J/\psi$  production [46]. (b) comparison with NLO CSM for direct  $J/\psi$  production [47].

The experimental points were compared with LO NRQCD predictions for prompt

$J/\psi$  [46] and with LO and NLO CSM calculations for direct production [46, 47] (also CSM for prompt production was tried, but the uncertainty gets much larger). At LO the NRQCD approach is clearly favoured, while the NLO computation of the CSM shows a rather good agreement with data. The theoretical uncertainty bands are quite large and, moreover, PHENIX data are placed at very low  $p_t$ , where the theoretical calculations start to be difficult because of divergencies.

Very recently the STAR collaboration has shown preliminary results on prompt  $J/\psi$  polarization. The result slightly extends the  $p_t$  reach of the PHENIX data and, despite the big error bands, confirms the trend observed at RHIC.

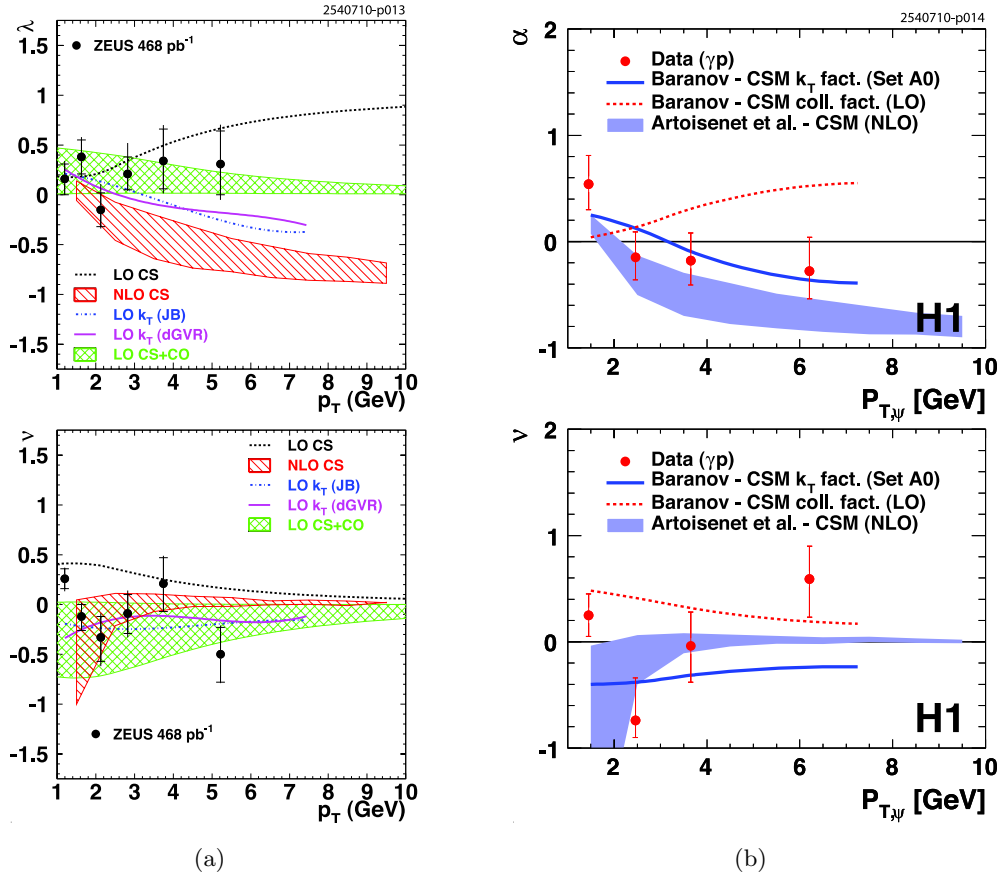


Figure 2.8:  $J/\psi$  polarization measured by ZEUS (a) and H1 (b) in the target and helicity reference frames [97, 53]. The notation is  $\lambda = \alpha = \lambda_\theta$  and  $\nu = \lambda_\phi$ . Experimental data from ZEUS are compared with LO and NLO CSM (lines and red band) and with LO NRQCD (green band) [54, 98]. H1 data are compared with LO and NLO CSM [54].

### 2.7.3 Results from collider experiments at HERA

Both the ZEUS and H1 collaborations published results on photo-produced  $J/\psi$  polarization making use of a large fraction of the collected data: 469 and 165  $pb^{-1}$  respectively [97, 53]. These two experiments have measured two ( $\lambda_\theta$  and  $\lambda_\phi$ ) of the three parameters which enter in the angular distribution, assuming the third one to be zero. ZEUS considered the so-called target frame (equivalent, for the  $z$ -axis, to the Gottfried-Jackson one), while H1 the helicity and the Collins-Soper frames.

The results, shown in Figure 2.8, are affected by quite large statistical uncertainties and show a  $\lambda_\theta$  value that is not far from zero.

The comparison of ZEUS data with several CSM (LO and NLO [54, 98]) predictions and LO NRQCD [98] seem to favour NRQCD at  $p_t$  of the order of 5 GeV/ $c$ . H1 data were only compared with CSM predictions at LO (with collinear or  $k_T$  factorization) and NLO accuracy [54, 98]. The experimental error bars are too large to draw any clear conclusion on photo-produced  $J/\psi$  polarization.

### 2.7.4 Results from the B-factories

The BaBar collaboration has studied the helicity distribution of  $J/\psi$  coming from the decay of B-mesons and of those coming from the radiative decay of higher charmonia states [99]. The  $z$ -axis was defined with respect to the laboratory reference frame, since the B momentum was not reconstructed. The results on the  $\lambda_\theta$  parameter (the only one extracted) are shown in Figure 2.9 and point to a significantly different from zero polarization. The value found for  $J/\psi$  coming from B decay ( $-0.46 \pm 0.06$ ) is in partial disagreement with an old NRQCD calculation [100], which was expecting something in the range  $-0.33 \div 0.05$ . The experimental value is also incompatible with the measurement carried out by CDF (see Section 2.7.1) for the same quantity, but the very different kinematical conditions do not allow to make a real comparison.

Also the Belle experiment has studied the helicity distribution of prompt  $J/\psi$  production as a function of the  $J/\psi$  transverse momentum [101]. In this case the studied  $p_t$  values range from 2 to 4.9 GeV/ $c$ . A constant longitudinal polarization (of the order of  $-0.4 \pm 0.1$ ) is observed, in better agreement with pure CSM predictions [102] than with calculations including also color octet terms [103]. In any case, the very low momentum region probed by the Belle experiment is the most difficult to assess from the theoretical point of view.



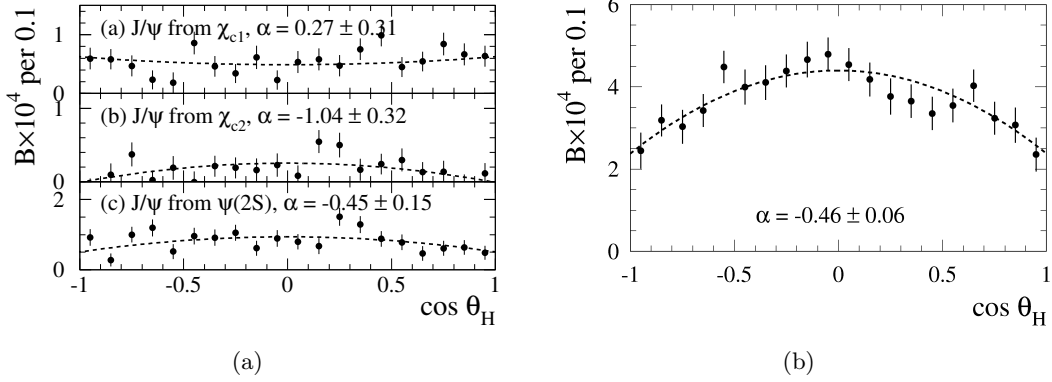


Figure 2.9:  $\alpha$  ( $= \lambda_\theta$ ) parameter in the helicity frame measured by the BaBar collaboration [99]. (a)  $J/\psi$  coming from the radiative decay of higher mass charmonia states. (b)  $J/\psi$  coming from the decay of B-mesons. The helicity axis is defined with respect to the collision center of mass frame.

### 2.7.5 Fixed target experiments

Some fixed target experiments have studied charmonium and bottomonium polarization. Even if theoretical calculations are not yet available for these results, it is worth to sketch the main outcomes.

#### E866

The E866 experiment at Fermilab studied  $J/\psi$  and  $\Upsilon(nS)$  polarization in collisions of 800 GeV protons with a copper target ( $\sqrt{s} = 38.8$  GeV) [104, 105]. The reference frame used for these analysis was the Collins-Soper one.

For what concerns the  $J/\psi$  [104], the  $\lambda_\theta$  parameter was found to be not much dependent on the  $p_t$  and a slightly decreasing trend with  $x_F$  was observed. The values were all placed inside a window ranging from -0.2 and +0.2. The result is shown in Figure 2.10(a).

An intriguing observation of the E866 collaboration concerns the  $\Upsilon(nS)$   $\lambda_\theta$  parameter [105]. The result is shown in Figure 2.10(b): the parameter is approximately zero at low  $p_t$  for the 1S resonance and increases going to  $p_t = 2-3$  GeV/c; for the 2S+3S states, on the contrary, it is equal to +1 in the full  $p_t$  range, as observed for Drell-Yan processes. The clear outcome, also allowed by the very small statistical error of the data points, bring much interest in the study of the 2S and 3S states in hadronic colli-

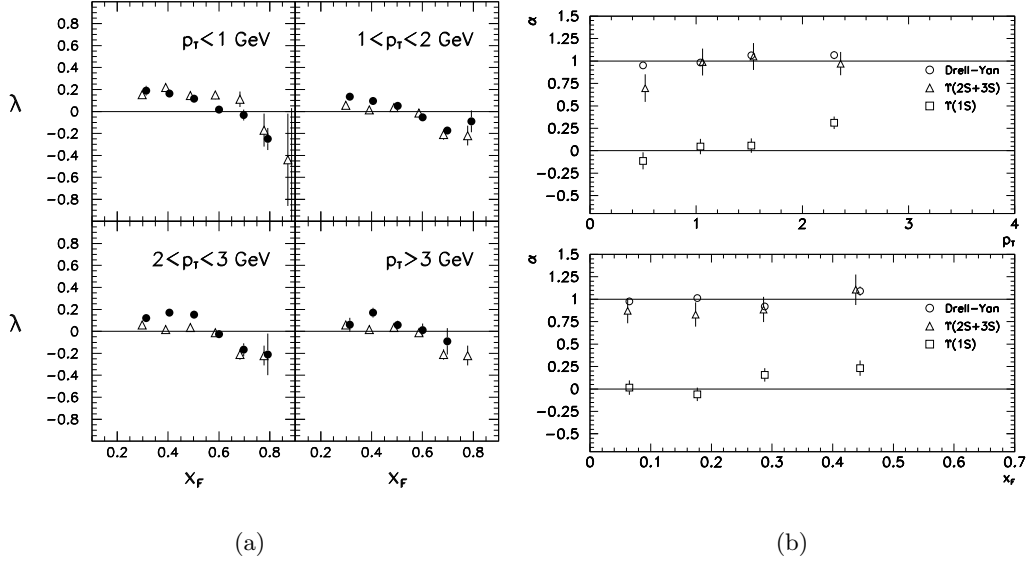


Figure 2.10:  $\alpha$  ( $= \lambda_\theta$ ) parameter in the Collins-Soper frame measured by the E866 collaboration for  $J/\psi$  (a) [104] and  $\Upsilon(nS)$  (b) [105] production. Full circles and open triangles in (a) refer to results obtained with different configurations of the experimental apparatus (magnet's current).

sions at higher  $p_t$ . This will probably be possible at the LHC, but for the moment no new results on this topic have been shown.

## NA60

The NA60 experiment at SPS has also studied  $J/\psi$  polarization in p-In collisions at 158 and 400 GeV [106]. The parameters extracted were  $\lambda_\theta$  and  $\lambda_\phi$ , imposing the  $\lambda_{\theta\phi}=0$  condition, in the helicity and Collins-Soper reference frames. The result is that the parameters are consistent with zero in all the  $p_t$  range explored (from 0 up to 2.5 GeV/c) and for both the frames. Moreover, the same study performed on In-In collisions at 158 GeV confirms this observation and doesn't show a clear dependence on the centrality of the collision.

## HERA-B

The HERA-B result on  $J/\psi$  polarization can be taken as an example (the first one) of a full angular analysis [107]. The  $\lambda_\theta$ ,  $\lambda_\phi$  and  $\lambda_{\theta\phi}$  parameters were extracted for  $J/\psi$  produced in p-C and p-W collisions at  $\sqrt{s} = 41.6$  GeV in three reference frames: helicity, Collins-Soper and Gottfried-Jackson.

The result is shown in Figure 2.11. The main information is that there is longitudinal

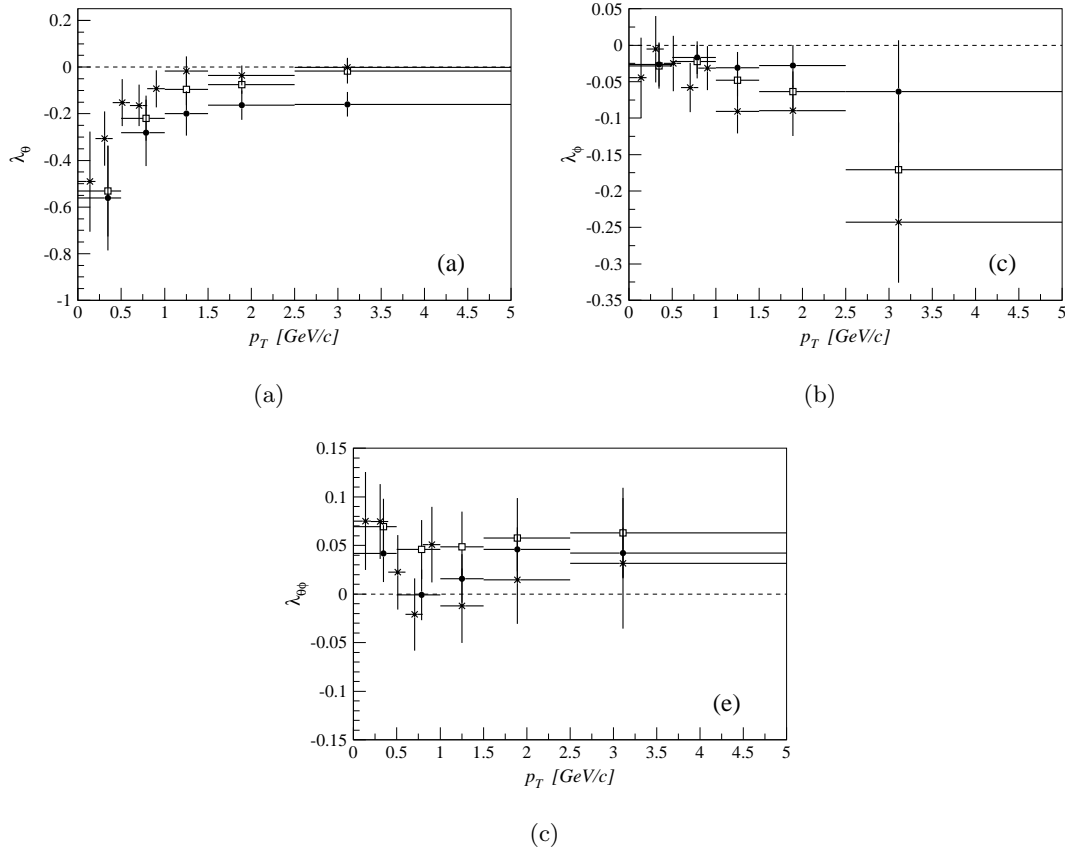


Figure 2.11: Polarization parameters for  $J/\psi$  production in p-C and p-W collisions as measure by the HERA-B collaboration [107]. The results obtained in the Collins-Soper, Gottfried-Jackson and helicity frames are represented, respectively, by black circles, white squares and asterisks.

polarization at very low  $p_t$  that vanishes going at higher transverse momenta. The magnitude of the  $\lambda_\theta$  parameter depends on the reference frame chosen; the same thing can be said for the  $\lambda_\phi$  parameter, but with the opposite tendency: in the reference

where the  $\lambda_\theta$  is higher,  $\lambda_\phi$  is lower and vice-versa. The  $\lambda_{\theta\phi}$  is everywhere a bit higher than zero, with typical values of 0.05.

### 2.7.6 Very recent theoretical results

The theoretical work described in Section 1.7 led to the determination of the long-distance color-octet matrix elements with a global fit to the  $J/\psi$  cross section data collected up to LHC energies. The extracted values can then be used to make predictions on the degree of polarization.

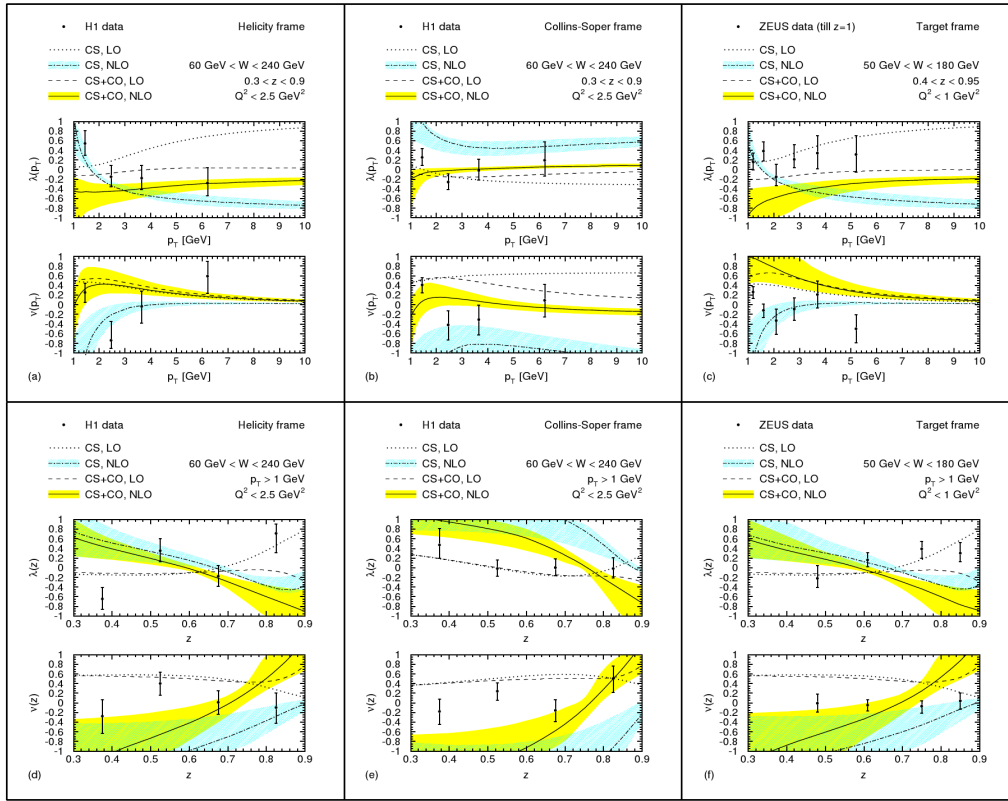


Figure 2.12: Polarization parameters as measured by the ZEUS (left) and H1 (right) collaborations in the helicity, Collins-Soper and Target reference frames [97, 53]. The notation is  $\lambda = \lambda_\theta$  and  $\nu = \lambda_\phi$ . Experimental data are compared with NLO CSM (light blue band) and with NLO NRQCD (yellow band) [108].

This was done both for photoproduction and hadroproduction, but the result in the

latter case will be shown in Chapter 4 Section 4.8, where the comparison with ALICE data will be discussed.

For photoproduction the situation is the one shown in Figure 2.12: H1 and ZEUS data are shown together with the prediction from NLO (LO) CSM and NLO (LO) NRQCD [108]. The very large statistical errors in the experimental points do not allow to draw a clear conclusion and also the theoretical curves are affected by large uncertainties. Contrarily to what stated in Section 1.7 for the cross section case, polarization data for photo-produced  $J/\psi$  do not clearly favour one approach with respect to the others.

## Chapter 3

# The ALICE apparatus at the LHC

ALICE (A Large Ion Collider Experiment) is the dedicated heavy-ion experiment at the Large Hadron Collider (LHC). Its main goal is the study of the Quark-Gluon Plasma (QGP), a state of matter formed in heavy ion collisions and which is believed to have characterized the first microseconds of the history of the Universe.  $pp$  collisions are studied by this experiment in order to obtain reference data for QGP-related analysis and to investigate open issues in elementary particle physics, such as the quarkonium hadroproduction mechanism.

In this chapter, after an introduction concerning the LHC acceleration facility in Section 3.1, a brief description of the ALICE detector layout is carried out in Section 3.2. The forward muon spectrometer of ALICE, the relevant sub-detector for the analysis reported in this thesis, is described in more detail in Section 3.3 and, in the following section (3.4), trigger and data acquisition are sketched. Finally, Section 3.5 is devoted to the presentation of the ALICE offline framework, which was extensively used for the  $J/\psi$  polarization analysis (see Chapter 4).

### 3.1 The Large Hadron Collider at CERN

The LHC [109] is the main accelerator at CERN and is designed to accelerate and collide protons and lead ions at the highest center of mass energies ever achieved (14 TeV for  $pp$  and 5.5 TeV/nucleon for  $PbPb$  collisions) and at high luminosity ( $\mathcal{L} = 10^{34} \text{cm}^2 \text{s}^{-1}$  and  $\mathcal{L} = 10^{27} \text{cm}^2 \text{s}^{-1}$  respectively). Other colliding systems, such as lighter ions and p-A, are also foreseen in the LHC program.

The accelerator is installed in the 27 km tunnel constructed for the former machine (the Large Electron Positron collider, LEP), and it is located between 45 and 170 meters underground across the frontier between Switzerland and France. The two counter-rotating beams circulate in two separated pipes inside the same yoke of the superconducting dipole magnets and can intersect in eight points. The dipole magnets are cooled at the temperature of 1.9 K with super-fluid Helium at atmospheric pressure and produce a magnetic field of 8.4 T.

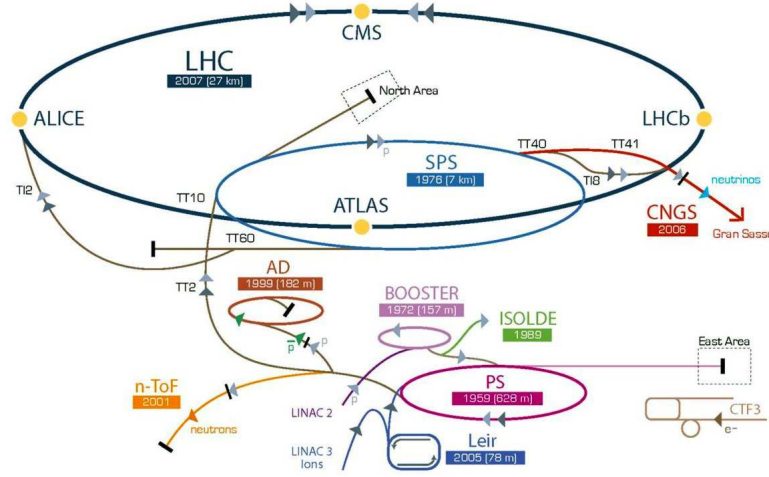


Figure 3.1: Schematic view of the CERN accelerator complex.

In Figure 3.1 the accelerating chain is shown. Protons start their accelerating process inside the linear accelerator (LINAC) and the Proton Synchrotron Booster; then they are injected in the Proton Synchrotron (PS), where they are accelerated up to a momentum of 25 GeV/ $c$ . The following step is the Super Proton Synchrotron (SPS), where protons reach the momentum of 450 GeV/ $c$  and are finally injected in the LHC. The ions acceleration procedure is more complex, as it includes additional stripping and accumulation phases at the beginning of the chain.

Large experiments are placed in four of the eight intersection points: ALICE [56], ATLAS [57], CMS [58] and LHCb [59]. Other two smaller experiments, LHCf [110] and TOTEM [111], share the interaction point with ATLAS and CMS respectively.

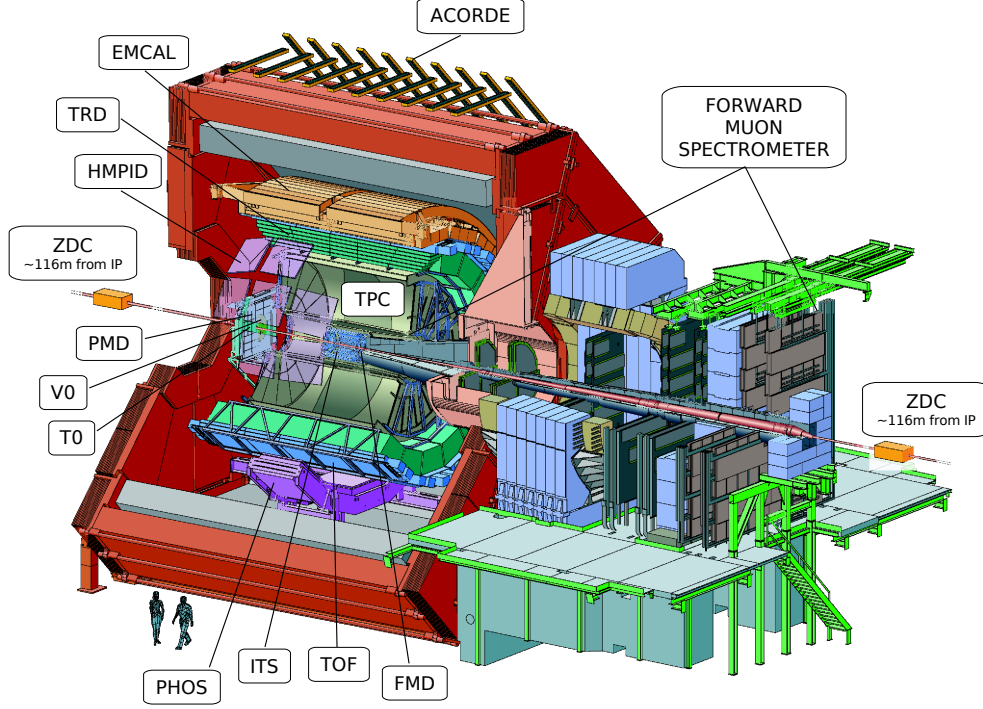
The assembling of the LHC started in 2005, when the first superconducting dipole was installed, and was completed in May 2007, when the last magnet was installed. At the end of 2008 the LHC circulated the first proton beams, but a serious accident occurred at the very beginning of the commissioning phase forced to stop for one entire year. Operations were resumed in November 2009, with  $pp$  collisions at  $\sqrt{s} = 900$  GeV. Due to the consequences of the accident occurred in 2008, in its first three years the machine is forced to run at lower energy with respect to the nominal one: proton beams are accelerated at 3.5 TeV/c and heavy ions at 1.38 TeV/c per nucleon.

In 2010 the operation time of the LHC was shared between machine development operations and physics-dedicated runs, while the target in 2011 was to deliver as much integrated luminosity as possible to the experiments and more than  $5 \text{ nb}^{-1}$  were collected by ATLAS and CMS. ALICE cannot cope with high interaction rates and, therefore, the proton beams are displaced to reduce the  $pp$  luminosity. The LHC also provided two months of  $PbPb$  collisions at  $\sqrt{s_{NN}} = 2.76$  TeV: in fall 2010 the luminosity was kept low, while in 2011 an integrated luminosity of about  $2 \cdot 10^2 \text{ } \mu\text{b}^{-1}$  was delivered to the experiments.

## 3.2 ALICE layout

ALICE was designed to study the physics of the quark-gluon plasma (see Section 1.8) in an unprecedented energy regime. It is a general-purpose heavy-ion experiment, sensitive to the majority of known observables (such as hadrons, electrons, muons and photons). The ALICE detector was built by a collaboration of more than 1000 physicists and engineers from more than 110 institutes of 33 countries. Its design is driven by the requirement of tracking and identifying particles in a wide momentum range (from less than 100 MeV/c up to about 100 GeV/c) and of reconstructing short-living particles such as open heavy flavours and hyperons in a very high multiplicity environment, up to 8000 charged particles per rapidity unit at mid-rapidity. The ALICE layout is shown in Figure 3.2 and consists of a central part, covering mid-rapidity ( $|\eta| < 0.9$ ) over the full azimuth, and several forward systems. The reference frame adopted by ALICE is a cartesian system with the origin in the interaction point (IP), the  $z$  axis along the beam pipe pointing at the opposite direction with respect





to the muon spectrometer, the  $y$  axis pointing upwards and the  $x$  axis completing the right-handed system and pointing at the center of the LHC.

The central part is placed inside a warm solenoid magnet that provides a maximum field of 0.5 T, which is useful to track low momentum particles. It essentially contains detectors devoted to the tracking and to the particle identification. The biggest forward system is the muon spectrometer, which is devoted to quarkonia and heavy flavours physics. Other smaller forward detectors are aimed to the determination of particle multiplicity in each event and of the centrality of heavy ion collisions.

In the following sections some details on each subsystem are given.

### 3.2.1 Inner Tracking System (ITS)

The ITS [56] consists of six cylindrical layers of silicon detectors, with a radius varying from 4 to 44 cm. Pixel, drift and strip detectors have been chosen for the two inner-most, the two intermediate and the two outer layers respectively. The high resolution pixel detectors have an extended polar-angle coverage ( $|\eta| < 1.98$ ) to provide, together

with the forward detectors, a continuous coverage in rapidity for charged particles multiplicity.

The six layers operate, together with the central detectors, at low frequency (about 100 Hz), while the Silicon Pixel Detector (SPD) can run at higher rate (about 1 kHz) to provide the vertex information for events triggered by the Forward Muon Spectrometer. The ITS is designed to localize the primary vertex with a resolution better than 100  $\mu\text{m}$ , reconstruct the secondary vertexes from the decay of hyperons and  $D$  and  $B$  mesons, track and identify low momentum particles ( $p < 100 \text{ MeV}/c$ ) and to complete and improve the information provided by the TPC.

### 3.2.2 Time Projection Chamber (TPC)

The TPC [56] is the main tracking detector of central barrel. It is designed to provide charged-particle momentum measurements up to  $p_t = 100 \text{ GeV}/c$ , with good particle identification and vertex determination in the high multiplicity environment of  $PbPb$  collisions. The simultaneous detection of high and low momentum particles is achievable with a low magnetic field ( $\leq 0.5 \text{ T}$ ) and a large detector volume which allows to measure a large section of the track, thus increasing the sensitivity for the sagitta determination. The TPC has an inner radius of about 85 cm and an outer one of about 250 cm, with a total length of about 500 cm. This size leads to a 88  $\mu\text{s}$  drift time, which is the limiting factor for the luminosity in  $pp$  collisions. The study of soft hadronic observables requires a resolution of 1% for momenta between 100  $\text{MeV}/c$  and 1  $\text{GeV}/c$ , while the detection of hard probes requires a 10% resolution for tracks with  $p_t = 100 \text{ GeV}/c$ . The latter can be achieved by using the TPC in combination with ITS and TRD. The resolution on the relative momentum between two particles, necessary to measure two-particle correlations, has to be better than 5  $\text{MeV}/c$ . Finally, the TPC can provide particle identification by  $dE/dx$  measurement in certain momentum intervals from the low-momentum region up to few tens of  $\text{GeV}/c$ , in combination with TOF, TRD and ITS.

### 3.2.3 Transition Radiation Detector (TRD)

The TRD [56] provides electron identification for momenta greater than 1  $\text{GeV}/c$ , where the pion rejection capability through energy loss measurement in the TPC is no longer sufficient. Its use, in conjunction with TPC and ITS, allows to measure the production of light and heavy vector meson resonances and, thanks to the determination of the impact parameter, of open charm and beauty. A similar technique can be used to

separate the directly produced  $J/\psi$  mesons from those produced by B-decays. The TRD consists of 18 sectors of 6 layers each with a 5-fold segmentation along the beam direction, for a total of  $18 \times 5 \times 6 = 540$  detector modules. Each module consists of a radiator of 4.8 cm thickness, a multi-wire proportional readout chamber and its front-end electronic. The TRD increases the ALICE pion rejection capabilities by a factor of 100 for electron momenta above 3 GeV/ $c$  and allows a mass resolution of 100 MeV/ $c^2$  for the  $\Upsilon$ .

### 3.2.4 Time Of Flight (TOF)

The TOF [56] is a large area array for particle identification in the momentum range from 0.2 to 2.5 GeV/ $c$ . Coupled with the ITS and TPC it provides an event-by-event identification of large samples of pions, kaons and protons. The need for a large coverage pushed to the use of a gaseous detector: Multi-gap Resistive Plate Chambers were chosen, providing an intrinsic time resolution of better than 40 ps and an efficiency close to 100%. The detector is segmented in 18 sectors in  $\phi$  and 5 segments in  $z$ . The whole device is inscribed in a cylindrical cell with an internal radius of 370 cm and an external one of 399 cm.

### 3.2.5 High Momentum Particle Identification Detector (HMPID)

Dedicated to the inclusive measurement of identified hadrons with  $p_t > 1$  GeV/ $c$ , the HMPID [56] is designed as a single-arm array with a pseudo-rapidity acceptance of  $|\eta| < 0.6$  and an azimuthal coverage of about  $58^\circ$ , corresponding to 5% of the central barrel phase space. The detector is based on proximity-focusing Ring Imaging Cherenkov counters and consists of seven modules of about  $1.5 \times 1.5$  m<sup>2</sup> each. The HMPID enhances the PID capability of ALICE by enabling the identification of particles beyond the momentum interval attainable through energy loss (in ITS and TPC) and time-of-flight measurements (in TOF). The detector is optimized to extend the range for  $\pi/K$  and  $K/p$  discrimination, on a track-by-track basis, up to 3 GeV/ $c$  and 5 GeV/ $c$  respectively.

### 3.2.6 PHOTon Spectrometer (PHOS)

The high resolution electromagnetic spectrometer [56] is designed to provide photon identification as well as neutral meson identification through the two-photons decay channel. The measurement of single photon and di-photon spectra and Bose-Einstein correlations of direct photons allow testing the properties of the initial phase of the

heavy-ions collision, while the detection of high-pt  $\pi^0$  allows the investigation of jet quenching as a probe of deconfinement. The PHOS is a single arm spectrometer including a highly segmented electromagnetic calorimeter made of lead-tungstenate crystals and a charged particle veto detector consisting of a Multi-Wire Proportional Chamber with cathode-pad readout. The spectrometer, positioned at the bottom of the ALICE setup at a distance of 460 cm from the interaction point, covers a pseudo-rapidity range of  $|\eta| < 0.12$  and  $100^\circ$  in azimuthal angle.

### 3.2.7 ElectroMagnetic Calorimeter (EMCal)

The EMCal [56] is the last detector added to the ALICE layout and its construction started in 2008. It improves the capabilities of jet studies and gives trigger signals on hard jets, photons and electrons. It is placed between the ALICE spaceframe, supporting the entire central detectors, and the magnet coils. The azimuthal acceptance covered ( $107^\circ$ ) is limited by the PHOS and the HMPID. The chosen technology is a layered Pb-scintillator sampling calorimeter with alternating layers of 1.44 mm of lead and 1.76 mm of polystyrene scintillator.

### 3.2.8 Forward Muon Spectrometer

The muon spectrometer [56] is the main forward detector in ALICE. It is devoted to heavy quarkonia and open heavy flavours detection. For details on this system see Section 3.3.

### 3.2.9 Forward Multiplicity Detector (FMD)

The FMD [56] is a silicon strip detector divided in seven disks perpendicular to the beam pipe and placed at distances between 42 and 225 cm from the IP. It provides a charged particle multiplicity information complementary to the SPD, covering the pseudo-rapidity ranges  $-3.4 < \eta < -1.7$  and  $1.7 < \eta < 5.1$ .

### 3.2.10 Photon Multiplicity Detector (PMD)

The PMD [56] is a preshower detector measuring the multiplicity and spatial ( $\eta - \phi$ ) distribution of photons on an event-by-event basis, in the forward region ( $2.3 < \eta < 3.7$ ). Placed at about 360 cm from the interaction point, in the side opposite to the Muon Spectrometer, the PMD provides estimates of the transverse electromagnetic energy and of the reaction plane on an event-by-event basis. It consists of two identical

planes of detectors, made of gas proportional counters with honeycomb structure and wire readout, with a  $3X_0$  thick lead converter in between.

### 3.2.11 T0

The T0 [56] consists of two arrays of Cherenkov counters, with a time resolution better than 50 ps, asymmetrically placed at 72.7 cm (muon spectrometer side) and 375 cm (PMD side) from the interaction vertex, with a pseudo-rapidity coverage of  $-3.28 < \eta < -2.97$  and  $4.61 < \eta < 4.92$  respectively. It is designed to provide a T0 signal for the TOF detector, to measure the vertex position with a precision of  $\pm 1.5$  cm, thus providing a Level-0 interaction trigger (see Section 3.4), and to measure the particle multiplicity.

### 3.2.12 V0

The V0 [56] is made of two arrays of scintillator material, located 90 cm (Muon Spectrometer side) and 340 cm (PMD side) from the interaction point. The detectors are segmented into 72 elementary counters distributed in 5 rings, with a pseudo-rapidity coverage of  $-3.8 < \eta < -1.7$  and  $2.8 < \eta < 5.1$ . The measurement of the time-of-flight difference between the two parts of the detector allows to identify and reject the beam-gas events, thus providing a minimum bias trigger for the central barrel detectors and a validation signal for the muon trigger. Moreover, the V0 can measure the charged particle multiplicity, thus resulting in a centrality indicator for  $PbPb$  collisions.

### 3.2.13 Zero Degree Calorimeter (ZDC)

The ZDC [56] provides a centrality estimation and trigger in  $PbPb$  collisions by measuring the energy carried in the forward direction (at zero degrees relative to the beam direction) by non-interacting (spectator) nucleons. The detector consists of two pairs of quartz-fibers hadronic calorimeters (for neutron and protons), placed on both sides of the interaction point, at 116 m from it. The system is completed by two electromagnetic calorimeters (ZEM), both placed at about 7 m from I.P. (PMD side), which allow to resolve ambiguities in the determination of the centrality.

Being placed between the beam pipes, the neutron calorimeter (ZN) has the most severe geometrical constraints: the transverse dimensions have to be smaller than 7 cm, requiring a very dense passive material (tungsten). The stringent space constraints do not hold for the proton calorimeter (ZP), which is made with a less dense material

(lead). The ZN, segmented in four regions, can also provide an estimation of the reaction plane.

The electromagnetic calorimeter (ZEM), made of lead and quartz fibres, is designed to measure the energy of particles, mostly photons generated from  $\pi^0$  decays, at forward rapidities ( $4.8 < \eta < 5.7$ ). Differently from the ZN and ZP, the ZEM fibres are oriented at  $45^\circ$ , a choice that maximizes the detector response. The ZDCs cannot provide a Level-0 trigger, since they are located too far from the interaction point, but they can provide an essential Level-1 trigger for centrality (see Section 3.4).

### 3.3 The Forward Muon Spectrometer

The goal of the muon spectrometer is the study of open heavy flavours, quarkonia and weak bosons production via their muonic decay channels in a wide range of transverse momentum and in the pseudo-rapidity range  $-4.0 < \eta < -2.5$ .

The design has been essentially driven by two requirements: perform charmonium detection down to zero transverse momentum and resolve the bottomonium states ( $\Upsilon(1S)$ ,  $\Upsilon(2S)$  and  $\Upsilon(3S)$ ) in the large-background environment of central  $PbPb$  collisions.

The spectrometer, shown in Figure 3.2, is composed by a system of absorbers, five stations of tracking detectors that, together with a warm dipole magnet, are used to measure muon momenta, and two stations of trigger chambers shielded by an iron wall. The spectrometer has a total length of 17 m and covers the polar angular range  $171^\circ \leq \theta \leq 178^\circ$  with respect to the ALICE reference frame.

In the following sections more details on each component of the muon spectrometer are given.

#### 3.3.1 Absorbers and shieldings

The ALICE Muon Spectrometer design was driven by the requirement of coping with a high multiplicity scenario in  $PbPb$  collisions: about 7000 particles produced in the spectrometer acceptance and about 6000 particles intercepting the beam-pipe in the region  $-7 < \eta < -4$ .

The front absorber has the double task of attenuating the forward flux of charged particles by at least two orders of magnitude and of decreasing the background of muons from the decay of pions and kaons by limiting the free path for primary  $\pi/K$ . This can be achieved by minimizing the distance between the absorber and the vertex,

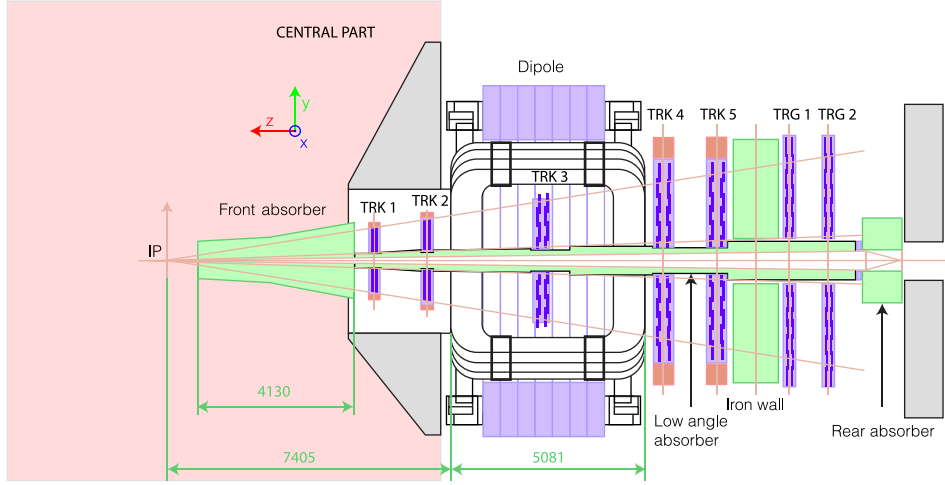


Figure 3.2: The ALICE muon spectrometer layout.

compatibly with the dimension of the inner tracker and the position of the multiplicity counters: the minimal value imposed by such constraints is 90 cm.

The absorber design and composition are optimized to provide good shielding capabilities on the one hand, and a limited multiple scattering (which could compromise the spectrometer mass resolution) on the other. This can be achieved by using low- $Z$  material in the absorber layers close to the vertex and high- $Z$  shielding materials at the rear end.

A total thickness of 20 cm of Pb interleaved with layers of boronated polyethylene, which can moderate neutrons by quasi-elastic scattering, was chosen for the front part, while lead and tungsten were selected for the rear end. The absorber is completed by a combination of concrete and carbon, as shown in Figure 3.3.

The small-angle beam shield is made of dense materials (pure tungsten in the most critical region, tungsten-lead mixture elsewhere) encased in a 4 cm thick stainless steel envelope. The latter is “pencil-shaped”: it follows the  $178^\circ$  acceptance line up to a maximum radius of 30 cm and then stays constant up to the end of the spectrometer. The inner cone opens up till the end of the muon arm.

The absorption system is completed by a muon filter, located between the tracking and the trigger system, 14.5 m away from the IP. It is a 120 cm thick wall made of iron, whose aim is to reduce the background on the trigger stations. The muon filter absorbs

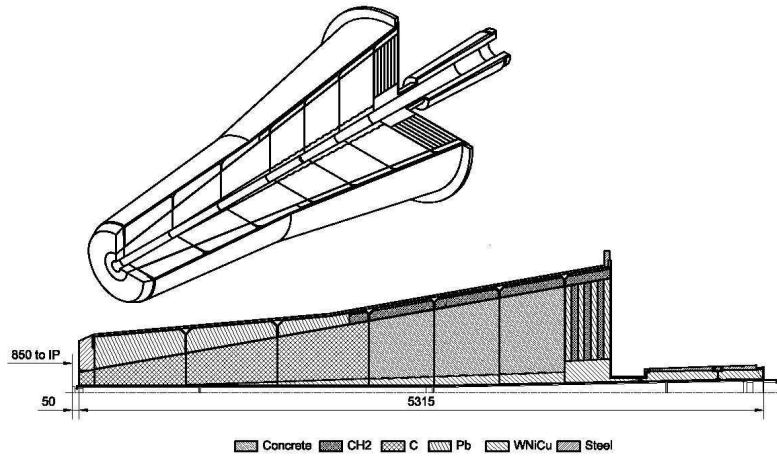


Figure 3.3: Layout of the front absorber.

hadrons and low-momentum muons: the combined effect of the front absorber and the muon filter prevents muons with  $p < 4 \text{ GeV}/c$  from reaching the trigger chambers.

### 3.3.2 Dipole magnet

The Muon Spectrometer is equipped with a warm dipole magnet which provides a maximum central field of 0.7 T and an integral field of 3 Tm. The general concept of the magnet is based on a window frame return yoke, fabricated from low carbon steel sheets. The saddle-type excitation coils are water-cooled with demineralized water, whose inlet temperature can vary between 15 and 25°C. Its overall dimensions are 5 m in length, 7.1 m width and 9 m height, with a total weight of about 890 tons.

The dipole has an angular acceptance of  $171^\circ < \theta < 178^\circ$  and is designed to provide a horizontal magnetic field perpendicular to the beam axis, whose polarity can be reverted within a short time.

### 3.3.3 The tracking system

The tracking chambers design was driven by two main constraints: to achieve the spatial resolution of  $100 \mu\text{m}$ , necessary for an invariant mass resolution of  $100 \text{ MeV}/c^2$  at the  $\Upsilon$  mass, and to operate in a maximum hit density of about  $5 \cdot 10^{-2} \text{ cm}^{-2}$ , the expected rate in central  $PbPb$  collisions. Less stringent criteria are required for the resolution along the non-bending plane (parallel to the magnetic field), which has to be better than about 2 mm to allow an efficient track finding. An additional constraint



is imposed by the large area (about 100 m<sup>2</sup>) covered by the tracking system.

All these requirements have been fulfilled by the use of Multi-Wire Proportional Chambers (MWPC) with cathode pad readout.

The detectors are arranged in five stations: two are placed before, one inside and two after the dipole magnet. Each station is made of two chamber planes, with two cathode planes each, which are readout in order to provide bi-dimensional information. The segmentation of the cathode pads is designed to keep the occupancy at a 5% level: since the hit density decreases with the distance from the beam pipe, larger pads are used at larger radii. The total number of channels is about one million.

Multiple scattering of the muons in the chamber is minimized by using composite material, such as carbon fibres, resulting in a thickness of about  $0.03X_0$ .

Although based on standard MWPC design, the individual chambers have been adapted to meet the particular constraints on the different tracking stations. The first two are based on a quadrant structure: Figure 3.4(a,c) shows a layout of the cathode plane for one of the quadrants of Station 2. For the other stations a slat architecture was chosen (Figure 3.4(b,d)). The slats and quadrants overlap to avoid dead zones in the detector.

For all the stations, the front-end electronics is based on a 64 channels board (MANas NUMérique, MANU). On this board the signals of four 16-channels charge amplifier chips (Multiplexed ANALogic Signal processor, MANAS) are sent to 12-bits ADCs and to a readout chip (Muon Arm Readout Chip, MARC) whose functionalities include the zero suppression. The Concentrator ReadOut Cluster (CROCUS) dispatches the trigger signal from the central trigger processor (CTP) to each half plane, it performs the calibration of the MANU, and gathers data through specific buses (Protocol for the ALICE Tracking CHamber, PATCH) sending them to the DAQ within 240 $\mu$ s after the trigger signal.

### **Alignment**

During the installation phase the chambers were positioned according to theodolite measurements and with photogrammetry, with a spatial accuracy of few tenths of a millimeter, but a better alignment is needed to assure the  $\Upsilon$  separation capability.

Special data-taking runs without magnetic field are periodically carried out in order to improve the quality of the alignment with an offline procedure: straight tracks are

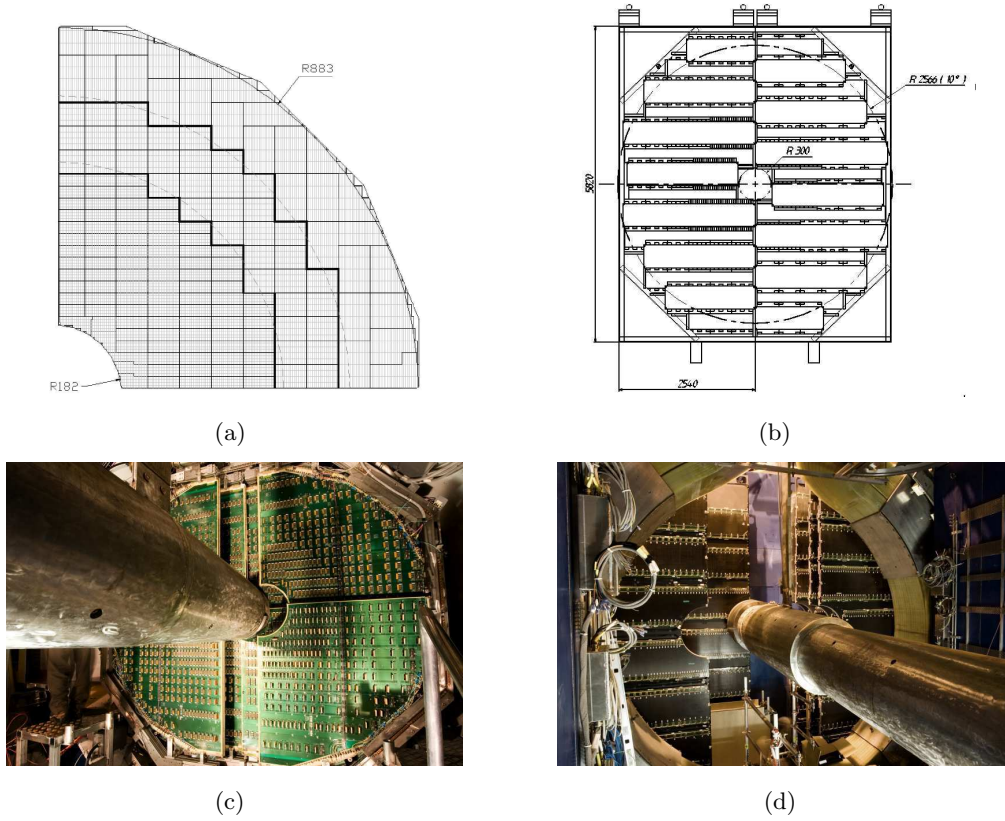


Figure 3.4: Tracking chambers: the cathode plane layout of Station 2 (a,c) and the scheme (b) of a station with slat architecture (d).

processed with the Millepede algorithm [112], thus determining the chamber positions. This positions can be taken into account in the track reconstruction phase. However, after switching on the magnet and electronic power supplies, such initial positioning can be disturbed by the forces of the L3 and dipole magnetic fields, as well as by the thermal expansion of the chambers and their support. The displacements and deformations are measured and recorded during data taking by the Geometry Monitoring System (GMS), *i.e.* an array of about 460 optical sensors which are placed on platforms located at each corner of the tracking chambers. The resolution achieved by the GMS is better than  $40\ \mu\text{m}$ .

### 3.3.4 The trigger system

The trigger system of the ALICE Muon Spectrometer consists of two trigger stations (MT1 and MT2) located at about 16 m from the interaction point and 1 m apart from each other, placed behind the iron muon filter.

Each station is constituted by two planes of 18 Resistive Plate Chambers (RPCs) that are large area detectors, made up of high resistivity ( $\sim 4 \cdot 10^7 \Omega\text{m}$ ) bakelite electrodes separated by 2 mm wide gas gap. The surface of the bakelite foils on the gap side is painted with linseed oil, while the external surface is painted with graphite, with one layer connected to the high voltage and the other to the ground (Figure 3.5).

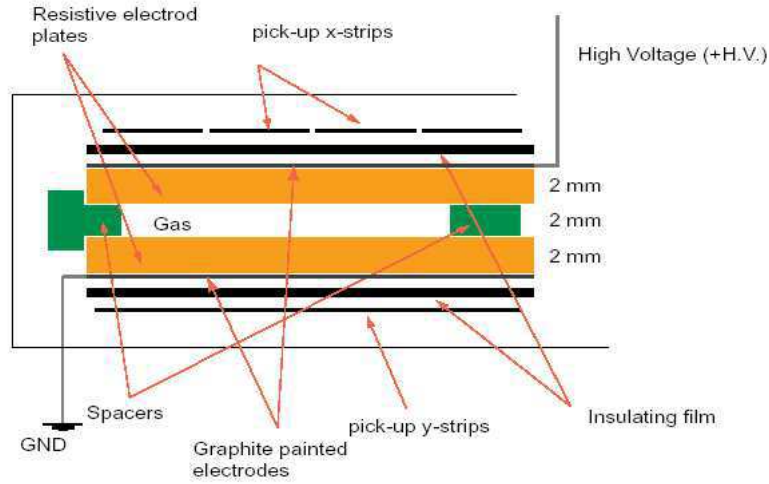


Figure 3.5: Schematic view of a Resistive Plate Chamber.

The signal is picked up by read-out strips connected with the Front-End Electronics (FEE), which basically consists of a leading-edge discriminator stage followed by a shaper. The strips are placed on both sides of the chambers, in order to provide a bi-dimensional information. The horizontal strips (aligned with the  $x$  axis in the ALICE reference system) measure the bending deviation due to the dipole magnetic field, while vertical strips (aligned with the  $y$  axis) measure the non-bending direction. The two layers of read-out pads are therefore called “bending” and “non-bending” plane respectively.

The signals coming from the FEE, consisting in the  $x$  and  $y$  fired strip patterns of the four detection planes, are sent to the local trigger electronics. The whole system is

divided in 234 detection areas, each of them associated with a local trigger board. The local board density reflects the strip segmentation which is finer in the region close to the beam pipe, where a higher particle multiplicity is expected: in particular, moving from the beam pipe outwards, the strip pitch is about 1, 2 and 4 cm in the bending plane and about 2 and 4 cm in the non-bending plane. The main aims of the local electronics are to perform the local trigger algorithm and deliver the trigger decision on single tracks, and to backup strip patterns and trigger decision in a pipeline memory which is read-out on occurrence of an ALICE trigger sequence.

The geometry of the detection elements is projective: straight tracks from the interaction point cross the strip with the same ID number in all chambers. The principle of the  $p_t$  cut with the trigger relies on the use of an estimated deviation of the measured track with respect to the track of a muon with infinite momentum (see Figure 3.6). The estimation is performed by the local boards. The maximum measurable deflection

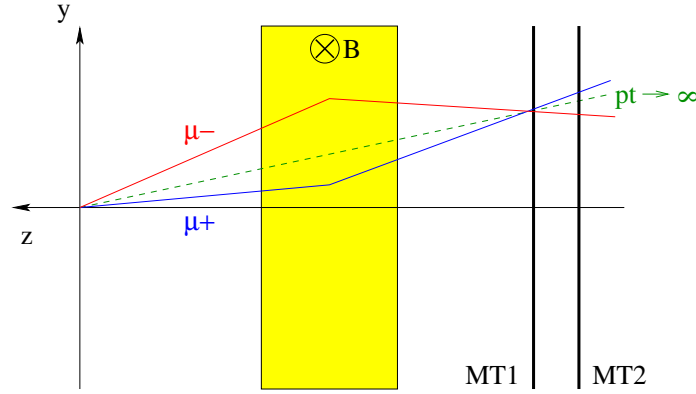


Figure 3.6: The muon spectrometer trigger principle, based on the estimation of the transverse momentum of the track: the larger the deviation, with respect to the  $p_t \rightarrow \infty$  straight line, the lower the  $p_t$  of the track.

has been fixed, for practical reasons, to  $\pm 8$  strips in the vertical direction and  $\pm 1$  in the horizontal direction. This defines the maximum width of the open “roads” between MT1 and MT2.

### Trigger chambers’ efficiency determination

The ALICE Muon Spectrometer provides a Level-0 trigger (see Section 3.4) for heavy quark and quarkonia measurements in the forward region. The spectrometer response

function can be calculated through simulations, provided the efficiency map of the Resistive Plate Chambers of which it is constituted. The nominal efficiency of each RPC was measured before installation and proved to be above 95%, but since the detector has to work for long periods in a high radiation environment, it is important to monitor any possible modification with respect to the nominal value. Moreover, due to the large area covered by each chamber, the possible variation in efficiency might be not homogeneous, so the maps have to be measured with the highest granularity achievable, *i.e.* on a local-board basis.

These requirements led to the implementation of a specific code which runs over all the tracks recorded by the muon spectrometer and gives a very accurate efficiency determination.

The method starts from the definition of a “triggerable” track, *i.e.* a track which fires at least three out of four chambers in both planes. Given a sample of  $N_{tot}$  particles, the number of reconstructed tracks firing all the chambers is:

$$N_{4/4} = N_{tot} \prod_{11 \leq i \leq 14} \epsilon_i$$

where the chambers are conventionally numbered from 11 to 14 in order to distinguish them from the 10 tracking chambers.

Analogously, the number of muons that would be triggered even if the information of the chamber  $ch$  is not taken into account is:

$$N_{3/4}^{ch} = N_{tot} \prod_{\substack{11 \leq i \leq 14 \\ i \neq ch}} \epsilon_i$$

Hence, the efficiency of the chamber  $ch$  can be calculated as:

$$\epsilon_{ch} = \frac{N_{4/4}}{N_{3/4}^{ch}}. \quad (3.1)$$

It is worth noting that the efficiency can be calculated separately for the bending and non-bending plane, since the 3/4 condition has to be satisfied by both independently. The algorithm for the chamber efficiency measurement, analyzes the reconstructed tracks searching for the presence of the associated fired strips in all chambers: in this way it is possible to determine  $N_{4/4}$  and  $N_{3/4}^{ch}$ , and hence the chamber efficiency according to Eq. 3.1.

### 3.4 ALICE trigger and data acquisition

The trigger signals from the detectors are collected and processed by the ALICE Central Trigger Processor (CTP). The CTP is designed to select events having a variety of different features and rates and to perform a scaling down of these rates in order to fit the bandwidth requirements of the acquisition system.

The first trigger signals, called Level-0 (L0), arrive  $1.2\mu\text{s}$  after the collision and are sent by the fastest detectors, such as the SPD, V0, T0 and the muon trigger system. These signals are combined in the CTP with logic AND and OR in order to select a certain class of events. The information of slower detectors is used to create a Level-1 trigger signal (L1), that is dispatched after  $6.5\mu\text{s}$ . The ALICE trigger system has a past-future protection circuit that looks for other events of requested types in time windows before and after the collision under investigation: this helps the rejection of pile-up events and the read out of the detectors. The last level of trigger, the so called Level-2 (L2), waits for the past-future protection and arrives after  $88\mu\text{s}$ .

The ALICE Data Acquisition system (DAQ) has been designed to cope with extremely challenging conditions: on the one hand  $pp$  collisions occur at high rates and have relatively small event sizes, while on the other hand  $PbPb$  collisions are characterized by lower rates and larger amount of data, up to  $1.25\text{GB/s}$  sent to the storage elements.

Once the CTP makes the decision to acquire a specific event, the trigger signal is dispatched to the front-end read-out electronics (FERO) of the involved detectors. Data are then sent to farms of computers, called Local Data Concentrators, that build the event fragments from the front-end electronics into sub-events. The sub-events are then sent to the Global Data Collectors (GDC) that take all the sub-events from the various LDCs and build the whole event and, eventually, send it to the storage facilities.

### 3.5 The ALICE offline framework: AliRoot

The project for the ALICE offline framework, AliRoot [113], started in 1998 [114] and has been continuously developed by the offline core team and collaboration members. AliRoot is entirely based on Object Oriented technology (C++) and depends on the ROOT [115] framework, which provides an environment for the development of software package for event generator, detector simulation, event reconstruction and data

acquisition and analysis.

The final objectives of the AliRoot framework are:

- the simulation of the primary hadronic collisions and the resulting detector response;
- the reconstruction of the physics data (raw-data) coming from simulated and real events;
- the analysis of reconstructed data.

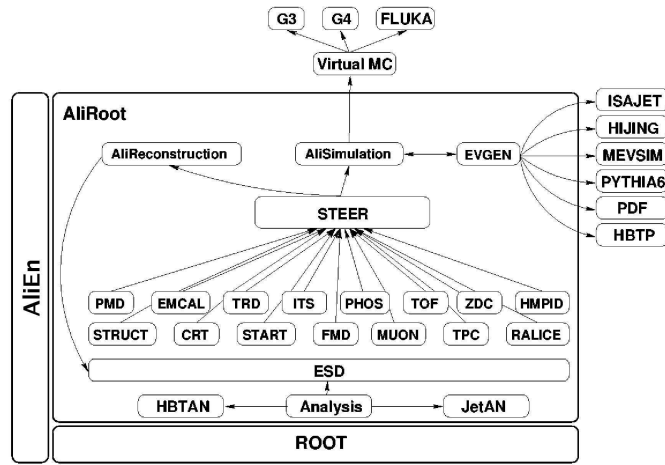


Figure 3.7: Schematic view of the AliRoot framework.

A schematic picture of the framework layout is shown in Figure 3.7: the core of the system is the STEER module, which provides steering, run management, interface classes and base classes. The codes from the different detectors are independent, so that different detector groups can work concurrently on the system while minimizing the interference. The hadronic collision can be simulated with different Monte Carlo event generators, like, for example, PYTHIA and Hijing, which are interfaced to the framework in a completely transparent way to the users. The detector response simulation follows the same logic, allowing the user to switch among different transport packages like GEANT3, GEANT4 and FLUKA.

The role of the framework is shown schematically in Figure 3.8. The left branch of the curve represents the simulation phase, when the Monte Carlo truth is degraded

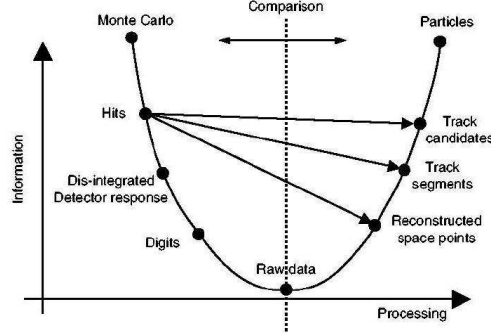


Figure 3.8: Data processing framework.

to reproduce the detector response. On the contrary, the right branch is the reconstruction phase: the real or simulated data are reconstructed in order to retrieve back the kinematics of the detected particles. The primary interactions are simulated via event generators and the resulting kinematic tree is then used in the transport package, where each particle is transported into the set of detectors: the point where the energy is deposited together with the amount of such energy constitutes an hit. The hits contain also information about the particle that generated them. At the next step the hits are dis-integrated: the information on the parent track is lost and the spatial position is translated into the corresponding detector readout element (*e.g.* strips, pads, etc.), thus generating the digits. The digits are eventually converted in raw-data, which are stored in binary format.

The reconstruction chain can then start from raw-data or from digits and allows the creation of track candidates. The final output of the reconstruction is an Event Summary Data (ESD), a root file containing all the output relevant for physics studies. Metadata information of reconstructed events in the ESD file are stored in the Tag database of AliRoot: this allows to select only those events of interest for the specific analysis considered, with a fast query to the database. The selection, performed through a train of “analysis tasks”, results in the creation of Analysis Object Data (AOD) files, which contain all the informations needed for a specific analysis and can be more easily handled by the users.





## Chapter 4

# J/ $\psi$ polarization study

The polarization study for inclusive J/ $\psi$  production in  $pp$  collisions at  $\sqrt{s} = 7$  TeV was carried out in ALICE at forward rapidity, using data collected by the forward muon spectrometer. The implementation of a dedicated muon trigger allowed to collect a sizable amount of J/ $\psi$ , essential for the polarization study. The implementation, during 2011, of new trigger strategies dedicated to the detection of rare events at midrapidity in the  $e^+e^-$  decay channel will allow to perform the same measurement for  $|y| < 0.9$ . In Section 4.1 the analysis strategy is outlined in view of the statistical and acceptance-related constraints. Section 4.2 is devoted to the description of the available data sample, while in Section 4.3 the cuts applied to the collected events are listed and motivated. The signal extraction is described in Section 4.4, while details on the Monte Carlo simulation performed for the estimation of the acceptance and the efficiency of the detector are given in Section 4.5. In Section 4.6 the fits to the corrected angular spectra are described, while in the following one (4.7) the detailed description of the various sources of systematic uncertainty and of the methods used for their estimation are reported. Final results are presented and compared with theoretical predictions in Section 4.8, while in the last two sections (4.9 and 4.10) some considerations on the assumptions made in the analysis and on the possible role of the non-prompt component in the inclusive measurement are given.

## 4.1 Analysis Strategy

From the experimental point of view, quarkonium polarization is studied through the extraction of the angular distribution of its decay products. This distribution was calculated in Chapter 2 Section 2.2 and corresponds to the expression:

$$W(\cos\theta, \phi) \propto \frac{1}{3 + \lambda_\theta} \cdot (1 + \lambda_\theta \cos^2\theta + \lambda_\phi \sin^2\theta \cos 2\phi + \lambda_{\theta\phi} \sin 2\theta \cos\phi). \quad (4.1)$$

For the analysis described in this section, the muonic decay channel was used and  $\theta$  and  $\phi$  represent the polar and azimuthal angles identified by the  $\mu^+$  direction in the rest frame of the  $\mu^+\mu^-$  system (also called “dimuon”). The helicity and Collins-Soper definitions of the polarization axis (see Chapter 2 Section 2.3 for their description) were adopted.

The basic analysis steps are the following:

1. define a binning for the angular variables;
2. divide the collected dimuon events according to the binning defined in the previous step and, for each bin, plot the invariant mass spectrum;
3. fit the invariant mass spectra and extract the number of  $J/\psi$  signal events for each angular bin;
4. correct the extracted yields for the detector acceptance and efficiency;
5. fit the corrected distribution with Eq. 4.1 and extract the  $\lambda$  parameters.

Considering that the goal is to study the evolution of the polarization parameters with the  $J/\psi$  transverse momentum, the data sample should be divided in bins of three variables:  $\theta$ ,  $\phi$  and  $p_t$ . This means that the number of collected dimuon events has to be sufficiently high to allow to perform a fit to the invariant mass in each bin. With the statistics collected by the muon spectrometer of ALICE during 2010 (corresponding to the data sample used for this analysis, see Section 4.2 for more details), this turned out to be impossible and a different approach was adopted.

It is indeed possible to factorize the  $\cos\theta$  and  $\phi$  dependencies by integrating Eq. 4.1 over  $\phi$  or  $\cos\theta$  respectively, thus obtaining [86]:

$$W(\cos\theta) \propto \frac{1}{3 + \lambda_\theta} (1 + \lambda_\theta \cos^2\theta) \quad (4.2)$$

$$W(\phi) \propto 1 + \frac{2\lambda_\phi}{3 + \lambda_\theta} \cos 2\phi. \quad (4.3)$$

These expressions provide a separation between the two angular variables and allow to divide the data sample in bins of:

- $\cos\theta$  and  $p_t$  to extract the  $\lambda_\theta$  parameter;
- $\phi$  and  $p_t$  to extract  $\lambda_\phi$ , once  $\lambda_\theta$  is known.

It is evident that Eq. 4.2 and 4.3 do not contain the parameter  $\lambda_{\theta\phi}$ , but this can be in principle estimated performing a change of variable:

$$\tilde{\phi} = \begin{cases} \phi - \frac{3}{4}\pi & \text{for } \cos\theta < 0 \\ \phi - \frac{1}{4}\pi & \text{for } \cos\theta > 0 \end{cases}$$

and studying the  $\cos\theta$ -integrated expression:

$$W(\tilde{\phi}) \propto 1 + \frac{\sqrt{2}\lambda_{\theta\phi}}{3 + \lambda_\theta} \cos\tilde{\phi}. \quad (4.4)$$

Nevertheless, the inclusion in the analysis procedure of the  $\tilde{\phi}$  variable introduces some additional issues and, for this reason, the  $\lambda_{\theta\phi}$  parameter was assumed to be zero. This is the approach adopted by all the experiments that carried out this analysis in the past, with the exception of HERA-B (see Chapter 2 Section 2.7), which measured  $\lambda_{\theta\phi}$  and found a value only slightly different from zero. More details on this topic and on the *a – posteriori* check of the assumption can be found in Section 4.9.

As seen in Chapter 2 Section 2.6, the detector acceptance is a key issue for the polarization study, in particular at low  $p_t$  and for values of  $\cos\theta$  approaching  $\pm 1$ . In this sense the ALICE muon spectrometer is not an exception. In Figure 4.1 the acceptance and efficiency of the detector as a function of  $p_t$  and  $\cos\theta$  in the helicity reference frame is shown: below 2 GeV/ $c$  and for  $|\cos\theta| > 0.8$  the acceptance falls steeply to values lower than 5%, forcing to exclude these kinematical regions from the analysis.

## 4.2 Data sample and run selection

The data sample used for the analysis is about 80% of the statistics collected by the muon spectrometer system during 2010 and corresponds to  $\sim 100 \text{ nb}^{-1}$ . It was collected during 2 months of data taking, from the beginning of September 2010 to the beginning of November of the same year. The runs corresponding to this period were dedicated to the muon spectrometer acquisition, since the readout detectors were only the muon

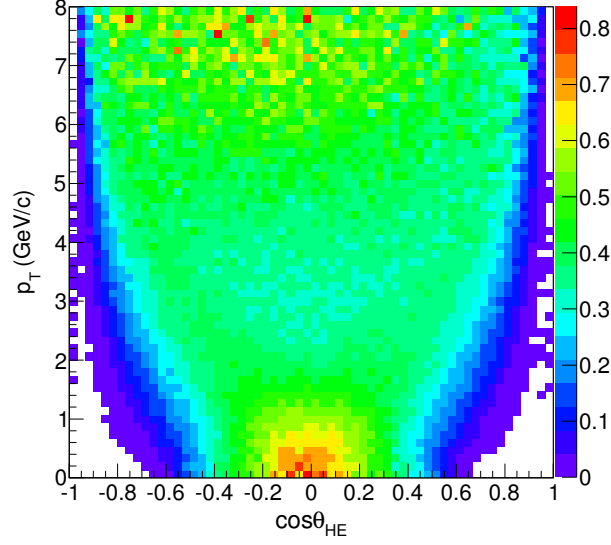


Figure 4.1: Two dimensional acceptance times efficiency plot ( $p_t$  as a function of  $\cos\theta$ ) from realistic Monte Carlo (MC) simulation for the helicity reference frame. See Section 4.5 for the details on the MC simulation.

trigger and tracking, the SPD, the V0 and the ZDC.

The active trigger class was the so-called CMUS, corresponding to a Minimum-Bias (MB) trigger in coincidence with a muon trigger. The MB trigger was defined as:

$$\{\text{sign}_{\text{SPD}} \text{ OR } \text{sign}_{\text{V0A}} \text{ OR } \text{sign}_{\text{V0C}}\} \text{ AND } \text{bptx}$$

where the different requirements correspond to:

- $\text{sign}_{\text{SPD}}$ : at least one pixel fired in the two SPD layers;
- $\text{sign}_{\text{V0A/C}}$ : at least one signal in the V0 hodoscopes in the A/C side;
- $\text{bptx}$ : the AND condition for a signal in the LHC beam pick-up counters (A and C sides).

The muon trigger algorithm is described in Chapter 3 Section 3.3.4 and acts as a non-sharp  $p_t$  cut on the single muon tracks. The  $p_t$  threshold of the trigger algorithm is programmable and, in the data taking period used for this analysis, was set to 1 GeV/c in the last week and to “all- $p_t$ ” (no  $p_t$  cut applied by the trigger) in the rest of the period. In order to use all the events together, an offline trigger of 1 GeV/c was

Table 4.1: Runs used for the analysis.

$p_t$ threshold	run numbers
all	133006 133010 133327 133330 133414 133419 133563 133800
	133924 133969 133985 134094 134198 134204 134304 134497
	134666 134679 134685 134690 134841 134905 134914 134919
1 GeV/ $c$	135658 135704 135709 135712
	135748 135761 135795 136177
	136180 136189 136372 136376

imposed to all the data (see Section 4.3).

The detector conditions along the whole data taking period were good and stable for the trigger stations, with an average efficiency per local board  $\geq 95\%$  and with no major problems coming from the read-out electronics (no dead areas were observed). Also the tracking chambers had a general good behaviour, with some specific electronic and detector issues, emerging from time to time, which forced to exclude some readout channels from the data acquisition. This non-uniformity in the detector conditions during the running period was taken into account in the MC simulation using the so-called “RejectList” (see Section 4.5).

Runs were selected according to the following criteria:

- the list of read-out detectors must contain the muon tracking (MTK), the muon trigger (MTG), the SPD and the VZERO;
- the run must be tagged as “good run” from the DAQ experts, meaning that the data acquisition was successful and that the running conditions were stable and under control;
- some quality checks (Quality Assurance - QA) have to be passed: they allow to monitor the stability of several key-parameters for the muon spectrometer data acquisition such as the trigger chambers efficiency, the number of cluster associated to a tracking track, the number of tracks per muon trigger, etc.

The full list of runs used for the analysis can be found in Table 4.1.

### 4.3 Analysis cuts

Analysis cuts were applied at three different levels: on the collected events, on the single tracks inside each event and on the opposite-charged muon pairs (dimuons).

The cuts on the events were performed in order to select real  $pp$  collisions and to reject events coming from beam-gas interactions. In order to obtain this filtering, the data were processed with a specific code devoted to the determination of “physics events”, called Physics Selection. The code selects the desired trigger class (CMUS for the current analysis) and adds the following requirements:

- {at least 2 clusters reconstructed in the SPD} **OR**  
  {at least 1 cluster reconstructed in SPD and a signal in either V0A or V0C} **OR**  
  {both the V0 fired};
- the V0 background flag off (see Chapter 3 Section 3.2.12);
- a number of SPD clusters lower than the quantity:  $65 + 4 \cdot SPD_{tracklets}$ .

The last requirement is imposed in order to remove from the data sample those events which were tagged online as coming from beam-beam collisions, but that were actually generated by beam-gas interactions. The rejection is based on the SPD clusters/tracklets correlation which, for genuine beam-beam events, is expected to be direct with a slope of about 3-4. Beam-gas interactions induce a rather different correlation, as the one shown in Figure 4.2 (right). If this kind of distorted behaviour is also seen in MB events, this means that in the sample some events come from beam-gas interaction (see Figure 4.2 (left)). The bulk part of these events (more than 60%) can be removed by means of the cut reported above (red line in Figure 4.2).

On top of the Physics Selection filter, two additional event cuts were applied: one vertex reconstructed with the SPD and at least two tracks reconstructed in the muon spectrometer were required to retain the event.

Inside each event, tracks must satisfy the condition  $2.5 < \eta < 4$  and must also have  $17.6 < R_{\text{abs}} < 88.9$  cm, where  $R_{\text{abs}}$  is the radial distance of the track from the beam axis at the end of the front absorber ( $z = 503$  cm). The latter requirement eliminates forward tracks which, due to the high- $Z$  material used in the absorber in that region (see Chapter 3 Section 3.3.1), are strongly affected by multiple scattering.

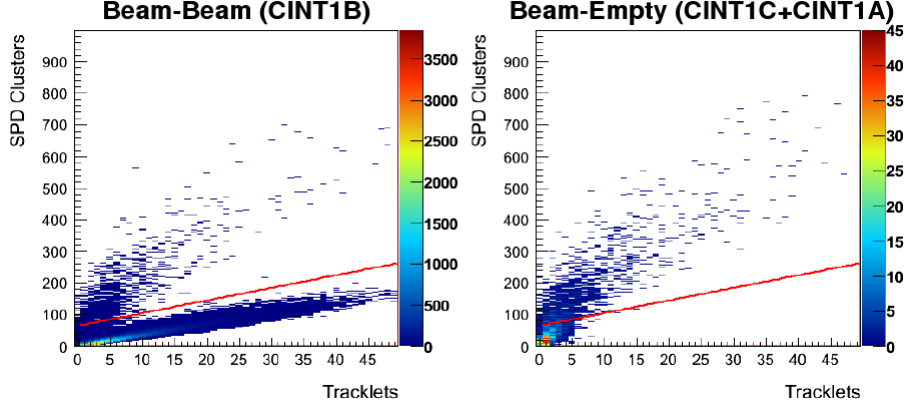


Figure 4.2: Correlation between number of SPD clusters and number of SPD tracklets for a MB-tagged event (left) and a beam-gas tagged event (right). The red line corresponds to the cut applied by the physics selection code.

After all the cuts described, single tracks with opposite charge are coupled two-by-two, building the so-called dimuon. A sharp cut on the rapidity is applied to all the dimuons to restrict the study to the detector acceptance:  $2.5 < y < 4$ . Finally, at least one of the two tracks forming the dimuon has to satisfy the offline muon trigger condition with a  $p_t$  threshold of 1 GeV/c, chosen as the highest of the two online trigger thresholds used for the data acquisition in the period under consideration.

## 4.4 Signal Extraction

The total number of  $J/\psi$  events in the data sample used for this analysis was estimated through a fit to the invariant mass spectrum of unlike sign dimuons after the application of all the cuts described in Section 4.3 and also applying the restrictions in  $p_t$  and  $|\cos\theta|$  motivated in Section 4.1. The  $J/\psi$  signal was described by a Crystal Ball function (CB) [116], which can be written in the form:

$$f_{sig}(m_{\mu^+\mu^-}) = \begin{cases} N \cdot e^{-\frac{1}{2} \cdot t^2} & \text{if } t > |\alpha| \\ N \cdot \left[ \frac{\frac{n}{|\alpha|}}{\frac{n}{|\alpha|} - |\alpha| - t} \right]^n \cdot e^{-\frac{1}{2} \cdot |\alpha|^2} & \text{if } t < |\alpha| \end{cases} \quad (4.5)$$

$$\text{where} \quad t(m_{\mu^+\mu^-}) = \begin{cases} \frac{m_{\mu^+\mu^-} - \mu}{\sigma} & \text{if } \alpha > 0 \\ -\frac{m_{\mu^+\mu^-} - \mu}{\sigma} & \text{if } \alpha < 0. \end{cases}$$



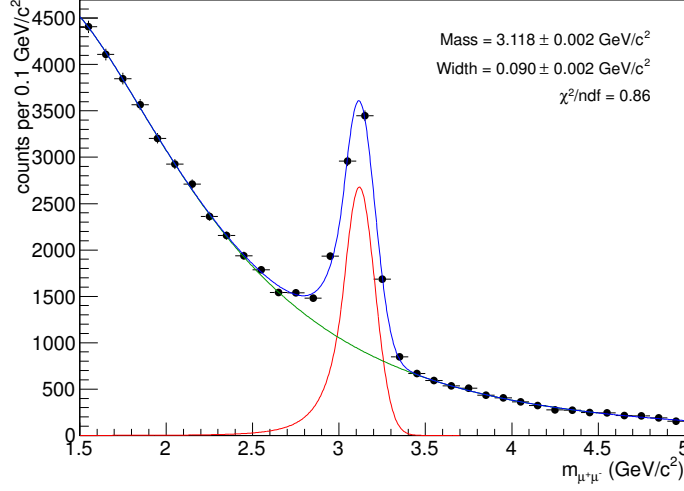


Figure 4.3: Invariant mass of opposite sign muon pairs in the range  $2 < p_t < 8$  GeV/ $c$ . The fit is plotted as a blue line and is the sum of a Crystal Ball function (for the signal, in red line) and of a gaussian with variable width (for the background, in green line).

This shape corresponds to the sum of a gaussian with variance  $\sigma$  and mean  $\mu$  and a polinomial tail, for values of the mass lower than  $\mu$ , which takes into account the radiative energy loss of the muons.

For the background an empirical function, corresponding to a Gaussian with a width ( $\gamma$ ) linearly depending on mass, was adopted:

$$f_{bkg}(m_{\mu^+\mu^-}) = N \cdot e^{-\frac{(m_{\mu^+\mu^-} - \nu)^2}{2\gamma^2}} \quad \text{where} \quad \gamma = \delta + \beta \cdot \frac{m_{\mu^+\mu^-} - \nu}{\nu}. \quad (4.6)$$

The fit is shown in Figure 4.3 and well describes the shape of the data, with a  $\chi^2/ndf$  of 0.86. The position of the CB peak differs from the  $J/\psi$  nominal mass (PDG value =  $3096.916 \pm 0.011$  MeV/ $c^2$ ) by 21 MeV/ $c^2$  and the width of the peak is in agreement with what expected from Monte Carlo simulations.

Integrating the CB in all the range from 1.5 to 5 GeV/ $c^2$  and normalizing to the bin width (100 MeV/ $c^2$ ), the number of  $J/\psi$  events that can be used for the analysis was obtained. The result is:

$$N_{J/\psi}^{\text{TOT}} = 6830 \pm 140$$

With this limited number of  $J/\psi$ , the binning in  $\cos\theta$ ,  $\phi$  and  $p_t$  has to be carefully chosen: a sufficient number of dimuon events for each bin is required to properly fit the corresponding invariant mass spectra.

Since both Eq. 4.2 and 4.3 are symmetric with respect to zero, the absolute values of  $\cos\theta$  and  $\phi$  were considered; moreover,  $|\phi|$  is expected to be symmetric with respect to  $\pi/2$  because of the period of the  $\cos 2\phi$  function and, for this reason, the azimuthal analysis was restricted to the region  $0 < |\phi| < \pi/2$ , mirroring events with  $|\phi| > \pi/2$  in the  $|\phi| < \pi/2$  region.

The study was performed in five bins for the  $|\cos\theta|$  variable:  $[0 - 0.15]$ ,  $[0.15 - 0.3]$ ,  $[0.3 - 0.45]$ ,  $[0.45 - 0.6]$  and  $[0.6 - 0.8]$ . In  $|\phi|$  four bins were defined:  $[0 - 0.63]$ ,  $[0.63 - 0.94]$ ,  $[0.94 - 1.26]$  and  $[1.26 - \pi/2]$ . The transverse momentum intervals were defined as  $2 < p_t < 3$  GeV/ $c$ ,  $3 < p_t < 4$  GeV/ $c$  and  $4 < p_t < 8$  GeV/ $c$ .

The fits to the invariant mass spectra corresponding to each bin of  $|\cos\theta|$ ,  $|\phi|$  and  $p_t$  were performed using the same function adopted for the determination of the total number of  $J/\psi$  events, *i.e.* the sum of Eq. 4.5 and Eq. 4.6. Other shapes were tried, instead of the CB, for the description of the peak, as a simple gaussian or a double Crystal Ball (with asymmetric tails in both sides), but they were both rejected since the first one badly described the low-mass region, while the second one gives very similar results with respect to the default choice, but with 2 additional free parameters. Also for the background case other functions were tested, as a single or a sum of two exponentials, but in both cases the shapes were not sufficiently flexible to adapt to the different background trends in the various bins.

The tails of the CB were fixed to the values extracted from the MC for each bin, since in real data the high background in the left part of the peak makes the evaluation of the signal tails difficult.

The width of the gaussian part of the CB function, when left as a free parameter in the fit to the data, was found to be dependent on the kinematics and to range between 72 and 120 MeV/ $c^2$ , in agreement with the MC within  $\sim 8 - 10$  MeV/ $c^2$ . As a default choice, this parameter was fixed, for each bin  $i$  (where  $i$  represents a certain  $|\cos\theta|$  or  $|\phi|$  interval for the  $J/\psi$   $p_t$  bin under study), to

$$\sigma_{J/\psi}^i = \sigma_{J/\psi} \cdot (\sigma_{J/\psi}^{i,MC} / \sigma_{J/\psi}^{MC}),$$

*i.e.* by scaling the measured width for the angle-integrated spectrum with the MC ratio between the widths for the bin  $i$  and for the integrated spectrum.

The position of the peak was left as a free parameter, and was found to correspond to

the nominal  $J/\psi$  pole mass within at most 1%.

The quality of all the fits was satisfactory, with  $\chi^2/\text{ndf}$  in a range between 0.63 and

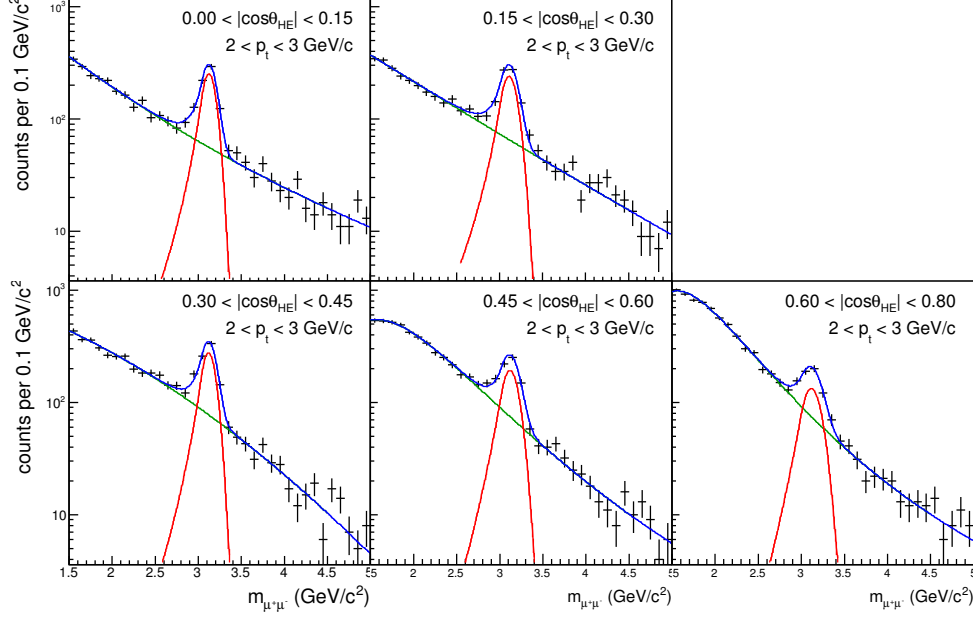


Figure 4.4: Invariant mass of opposite sign muon pairs in the five bins of  $\cos\theta_{HE}$  for  $2 < p_t < 3 \text{ GeV}/c$ . The fit to each spectrum is plotted as a blue line and is the sum of a crystal ball (for the signal, red line) and of a gaussian with variable width (for the background, green line).

1.34. Signal over background ratios in a  $\pm 3\sigma$  mass window around the CB peak were found to vary between 0.5 and 3.5.

In Figure 4.4, as an example, the fits to the five bins of  $|\cos\theta|$  for the  $p_t$  bin from 2 to 3  $\text{GeV}/c$  are shown as blue lines and also the signal (red lines) and background (green lines) components are shown separately: the fitting function well reproduces the data for all the bins.

All the fits to the invariant mass spectra,  $\chi^2/\text{ndf}$ , S/B and number of signal events extracted for each bin are reported in Appendix B.

## 4.5 Acceptance and Efficiency correction: iterative procedure

The acceptance and efficiency ( $A \times \epsilon$ ) of the detector was evaluated through Monte Carlo simulation of pure signal events. The software framework used for the simulation was AliROOT (see Chapter 3 Section 3.5), which contains all the informations on the geometry of the detector, useful for a realistic reconstruction of the simulated events.

The input distributions for the kinematical variables ( $p_t$  and  $y$ ) were chosen as a parametrization of the differential cross-sections measured by ALICE at forward rapidity in previous analysis, with data taken at the same energy [60]. In Figure 4.5 the measured cross-sections are plotted together with their systematical errors (boxes). The parametrizations are shown as red lines and correspond to the following shapes:

$$f(p_t) = \frac{p_t}{\left[1 + 0.36 \cdot \left(\frac{p_t}{2.44}\right)^2\right]^{3.9}} \quad , \quad g(y) = \exp - \frac{(y/7.72)^2}{2 \cdot 0.383^2}.$$

The angular distribution of the decay products was chosen to be flat, since the anisotropies on this distribution are not known a priori and rather represent the outcome of this analysis.

In order to simulate a realistic response of the different detectors, the framework makes use of the Offline Condition DataBase (OCDB), which contains informations on the performances of each detector during each run. Some of the OCDB files are automatically generated during the data taking and keep track of the general conditions of the apparatus on a run-by-run basis; others are built specifically for the MC simulation and embed informations extracted from real data.

The most important OCDB entries used for the MC simulation in this analysis are:

- **Trigger Chamber efficiency:** this quantity is evaluated for each local board using real events, following the procedure described in Chapter 3 Section 3.3.4. Typical values for the efficiency are 95-98%, as can be seen in Figure 4.6 for the case of the bending plane of station 12. From Figure 4.6 (b) it is possible to see that the errors on the efficiencies are quite low and of the order of 0.5% in average;
- **Residual Misalignment:** it contains a random misalignment, for each tracking chamber, inside the range  $0\text{-}mis_{max}$ , where  $mis_{max}$  is the maximum residual

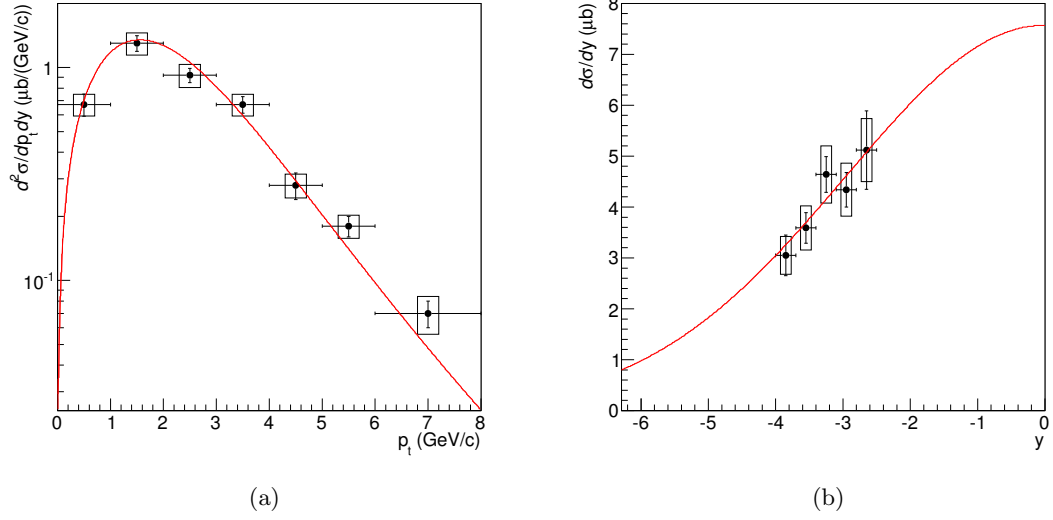


Figure 4.5: Differential cross section for inclusive  $J/\psi$  production as a function of  $p_t$  (left) and  $y$  (right) as measured by the ALICE experiment in pp collisions at  $\sqrt{s} = 7$  TeV. Bars are the statistical errors, boxes are the systematical errors. The red line is the parametrization adopted in the MC simulation used for  $A \times \epsilon$  determination.

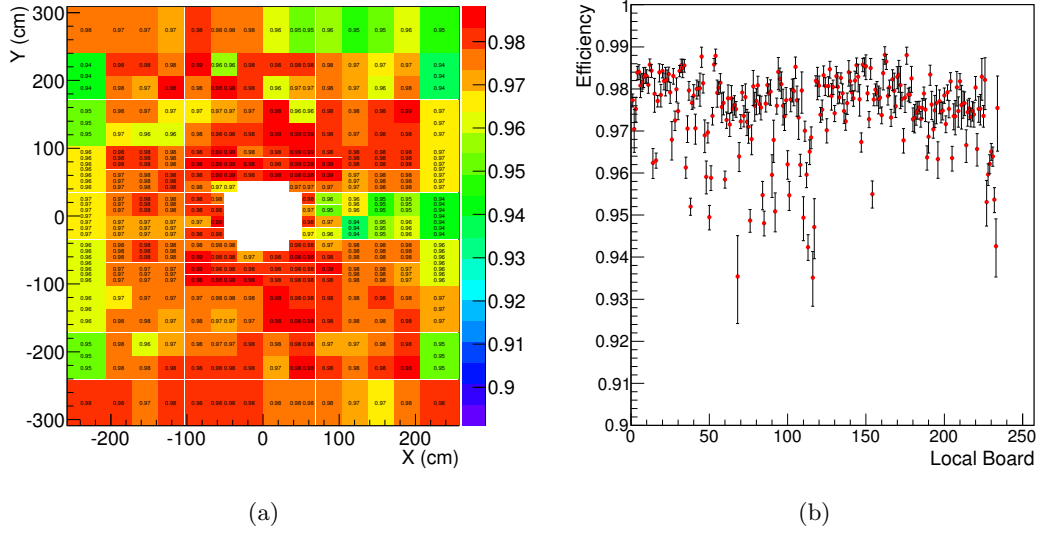


Figure 4.6: Efficiency values for each local board of the bending plane of chamber 12 (second plane of the first trigger station).

misalignment estimated after the alignment procedure described in Chapter 3 Section 3.3.3;

- **Reject List:** the list of all the dead channels in the tracking stations. Since only one MC generation was performed for the whole period and considering that the dead channels can change from run to run, the probability of having one particular dead channel is weighted for the statistics collected when that channel was off.
- **MUON RecoParam:** the list of parameters used for the online reconstruction of the tracks in real data (*e.g.* definition of the tracking algorithm, cuts on the clusters associated to a track, on the low/high limits in momentum, etc.).
- **ITS RecoParam:** analogously to the previous case, the list of the parameters used by the ITS to reconstruct the vertex. This is used to simulate a realistic primary vertex distribution.

With the MC simulation described above it is possible to extract the two-dimensional ( $\cos\theta$  or  $\phi$  as a function of  $p_t$ )  $A \times \epsilon$  map in the particular conditions in which the data were collected. These maps are shown in Figure 4.7 for the helicity and the Collins-Soper reference frames.

Two main considerations can be made:

- The symmetry between positive and negative values of the angular variables, already discussed in Section 4.1 for Eq. 4.2 and 4.3, is present also at the acceptance level. Opposite values of  $\cos\theta$  and  $\phi$  correspond, in fact, to the same angular configuration, but with the  $\mu^+$  and the  $\mu^-$  exchanged: considering that the acceptance and the efficiency of the muon spectrometer do not depend on the charge of the muon, the  $A \times \epsilon$  has to be the same for positive and negative regions of the angular variables.
- As already discussed in Section 4.1, the acceptance falls down to zero for low  $p_t$  and large  $|\cos\theta|$  values. This aspect was discussed in Chapter 2 Section 2.6 and is related to the fact that in these particular kinematical configurations the two decay muons are aligned with the polarization axis in the  $J/\psi$  rest frame: one of them with the same versus, the other one with opposite versus. Observing the situation from the laboratory reference frame, this means that one of the two muons can be either outside the detector's geometrical acceptance or have

very low momentum and, in both cases, it cannot be tracked in the spectrometer. This is particularly valid in the HE reference frame, where the direction of the  $J/\psi$  in the laboratory is chosen as the polarization axis, but holds also for the CS frame which, in the low- $p_t$  region probed by ALICE, is not very different from the helicity one.

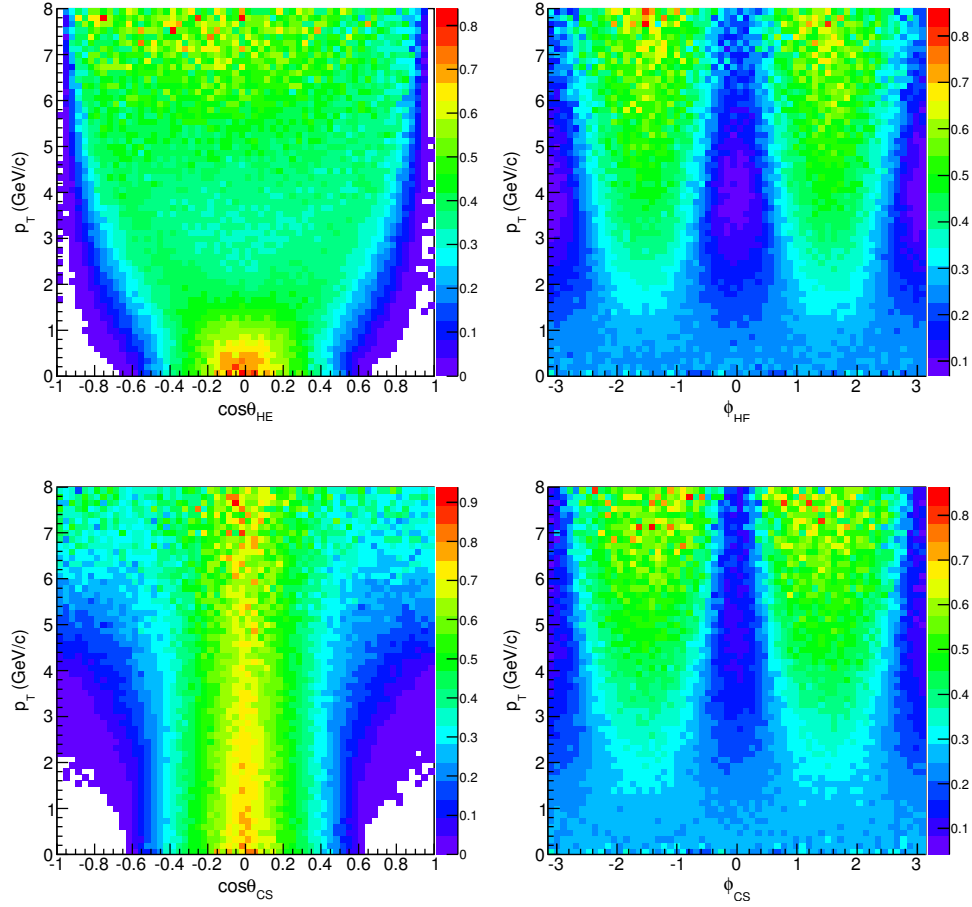


Figure 4.7: Two dimensional  $A \times \epsilon$  plots from realistic MC simulation for the helicity (top) and the Collins-Soper (bottom) reference frames:  $\cos\theta$ - $p_t$  (left) and  $\phi$ - $p_t$  (right).

When the analysis strategy involves the integration of the signal over one kinematical variable, the acceptance correction can be biased if the differential distribution injected

in the MC simulation for the integrated variable is not known a priori (see Appendix A for more details on this point).

In this analysis the rapidity dependence of the polarization parameters is not studied and the signal is therefore integrated over  $y$ , but this doesn't represent an issue for the  $A \times \epsilon$  correction, since the  $y$  differential distribution for inclusive  $J/\psi$  production was already extracted in previous analysis [60] and a parametrization of this shape was used for the MC simulation.

The other integration performed in this analysis is the one over the angular variables: the  $|\phi|$  dependence is neglected when the  $|\cos\theta|$  spectrum is studied and, the other way around, the signal is integrated over  $|\cos\theta|$  when the  $|\phi|$  spectrum is considered. In this case the correct input distributions are not known a priori, but rather represent the outcome of the analysis. Moreover, the effect of polarization (in particular of the  $\lambda_\theta$  parameter) on the acceptance was found to be very strong (up to  $\sim 30\%$ ) in previous analysis [60]. For this reason, an iterative procedure for the  $A \times \epsilon$  correction was adopted.

The procedure starts with the non-polarized MC sample described above, which is used for a first-step correction of the differential  $|\cos\theta|$  and  $|\phi|$  distributions. The fit to the corrected spectra with the functional forms in Eq. 4.2 and 4.3 (see Section 4.6) gives a first estimation of the parameters:  $\lambda_{\theta,HE}^{1st}$ ,  $\lambda_{\phi,HE}^{1st}$ ,  $\lambda_{\theta,CS}^{1st}$  and  $\lambda_{\phi,CS}^{1st}$ . These values are used to weight the flat MC in order to obtain a new simulated sample, this time polarized as the first estimation got from real data: this sample is used to perform a new  $A \times \epsilon$  correction of the spectra which, when fitted, give a second estimation of the parameters ( $\lambda_{\theta,HE}^{2nd}$ ,  $\lambda_{\phi,HE}^{2nd}$ ,  $\lambda_{\theta,CS}^{2nd}$  and  $\lambda_{\phi,CS}^{2nd}$ ). The iteration proceeds in this way until a stability condition is reached, *i.e.* when the results at the step  $i$  are the same obtained at the step  $(i - 1)$  within a given fiducial value, which was chosen to be 0.005 since the results are given with a 2-digit accuracy. In Figure 4.8 the  $\lambda_\theta^{HE}$  parameter as a function of the iteration number is plotted for the three  $p_t$  bins considered (in this case the procedure was carried on for 10 iterations, even if the convergence condition was verified earlier), showing the effect of the iterative procedure, which is not very large and is more important for values of the parameters different from zero. The stability is reached in at most 3-4 iterations, with values that, from iteration to iteration, do not fluctuate much.

In order to evaluate the robustness of this approach some tests were performed and are reported in Appendix D.



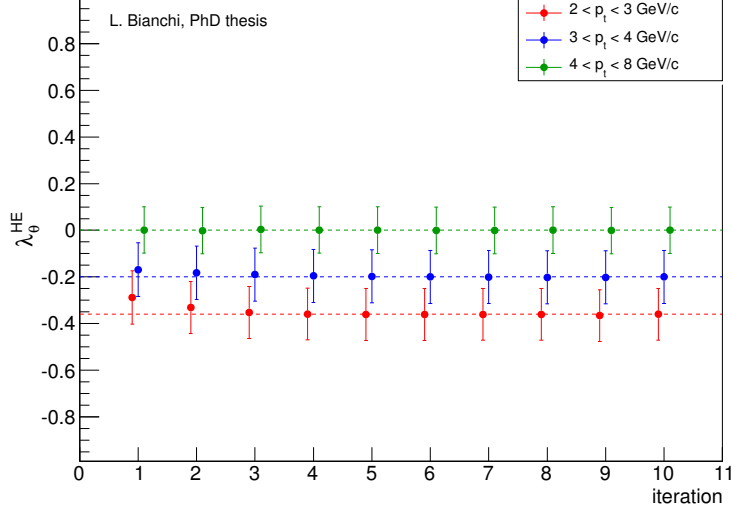


Figure 4.8:  $\lambda_\theta$  parameter estimated for the three  $p_t$  bins in the helicity reference frame as a function of the iteration number. Errors are purely statistical.

## 4.6 Fits to the $A \times \epsilon$ corrected spectra

A simultaneous study of the  $J/\psi$  polarization in two reference frames is particularly interesting since frame-invariant quantities can be worked-out (see Chapter 2 Section 2.5) and used in the analysis procedure.

In particular, for each iteration of the  $A \times \epsilon$  correction, the four spectra ( $|\cos\theta_{HE}|$ ,  $|\phi_{HE}|$ ,  $|\cos\theta_{CS}|$  and  $|\phi_{CS}|$ ) were simultaneously fitted with Eq. 4.2 and 4.3, adding the additional constraint:

$$\mathcal{F} = \frac{\lambda_\theta^{HE} + 3\lambda_\phi^{HE}}{1 - \lambda_\phi^{HE}} = \frac{\lambda_\theta^{CS} + 3\lambda_\phi^{CS}}{1 - \lambda_\phi^{CS}}, \quad (4.7)$$

which decreases the number of angular free parameters from four to three and, therefore, reduces the statistical error on the results.

This invariant quantity  $\mathcal{F}$  corresponds to the class of invariants reported in Section 2.5, when the three parameters  $c$  assume the values:

$$c_1 = -3, \quad c_2 = 0, \quad c_3 = 1.$$

In Figure 4.9 the simultaneous fit for the  $2 < p_t < 3$  GeV/ $c$  bin is shown for the last iteration of the  $A \times \epsilon$  calculation. The quality of the fit is good for all the  $p_t$  bins, the  $\chi^2/ndf$  values being 1.08, 1.00, 1.32 for  $2 < p_t < 3$ ,  $3 < p_t < 4$  and  $4 < p_t < 8$  GeV/ $c$

respectively, as can be seen in Appendix C.

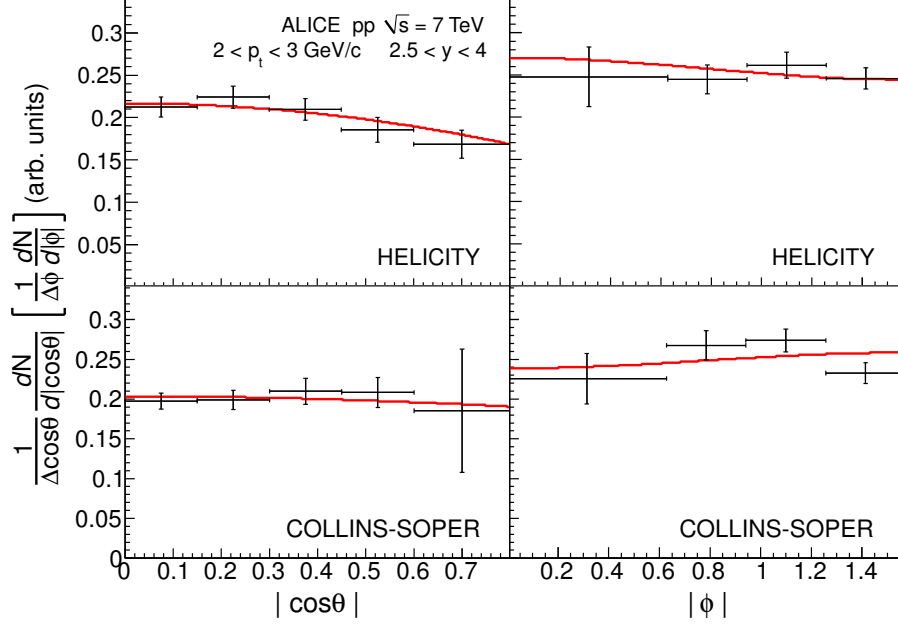


Figure 4.9:  $A \times \epsilon$  corrected spectra for the first  $p_t$  bin in the helicity (top) and Collins-Soper (bottom) reference frames. Errors are pure statistical. The red line represents the simultaneous fit with the  $\mathcal{F}$ -invariance constraint.

Forcing the fit to satisfy the  $\mathcal{F}$  invariance is not compulsory in the analysis procedure: it was verified (see Appendix D) that, fitting the corrected spectra separately for the two frames, the results are in agreement with what found with the default approach.

## 4.7 Systematic uncertainties

Various sources of systematic uncertainty on the measurement of the polarization parameters have been investigated by slightly varying the analysis procedure and looking at the effect of this change on the final results. In principle, detector-related systematics are not expected to be large since the angular distribution of the muons is measured in event-by-event defined reference frames and the effect of some local detector issues not well taken into account in simulation is in general diluted in the final result.

Nevertheless, the estimation of the systematics is not trivial since the limited statistics

used for the analysis do not allow to completely disentangle the systematical from the statistical sources of uncertainty: little changes in the analysis procedure can induce sizable effects in the final results mostly due to the natural statistical fluctuation around the estimated central value rather than to real systematic effects. For this reason, if the source of systematic is not expected to be dependent on the  $p_t$  of the  $J/\psi$ , the best way to evaluate its effect would be to apply it in the whole  $p_t$  range from 2 to 8 GeV/c in order to reduce the statistical effect. This was in the end possible only in one case (signal extraction), while for the other cases the three  $p_t$  bins were maintained for the evaluation.

The uncertainty on the signal extraction is not expected to be very much dependent on the  $p_t$  of the  $J/\psi$ , as already found in previous analysis [60], and was therefore estimated in the whole explored  $p_t$  range. It was evaluated repeating all the analysis leaving the width of the CB function as a free parameter in the fits to the invariant mass spectra. This procedure leads to an absolute variation of the polarization parameters between 0.02 and 0.10, in general higher for  $\lambda_\theta$  than for  $\lambda_\phi$ .

Another sizeable source of systematic uncertainty is the choice of the input distributions for  $p_t$  and  $y$  in the simulation (see Section 4.5 and Appendix A for the motivation). It was evaluated by comparing the results obtained with the default choice with those obtained simulating the  $p_t$  and  $y$  shapes with an extrapolation of lower energy results [117]. The parametrizations used are:

$$f'(p_t) = \frac{p_t}{\left[1 + \left(\frac{p_t}{5.07}\right)^2\right]^{4.1}} \quad , \quad g'(y) = 100.78 - 1.8353 \cdot y^2$$

and are shown in Figure 4.10 (blue lines). In this case the magnitude of the effect is in principle dependent on the  $p_t$  of the  $J/\psi$ , since the difference between the two  $p_t$  shapes used is not constant versus  $p_t$ : for this reason the systematic was evaluated in  $p_t$  bins. The absolute effect that this change of parametrization in the MC simulation causes on the polarization parameters varies between 0.01 and 0.07.

For the lowest  $p_t$  bin, the acceptance in the helicity frame drops by about 40% in the highest  $|\cos \theta|$  bin used in the analysis ( $0.6 < |\cos \theta| < 0.8$ ), and has also a strong variation inside the bin itself. An alternative approach was therefore followed, fitting the angular spectrum in the restricted interval  $0 < |\cos \theta| < 0.6$  (instead of the default choice  $0 < |\cos \theta| < 0.8$ ) and conservatively considering the absolute variation in the

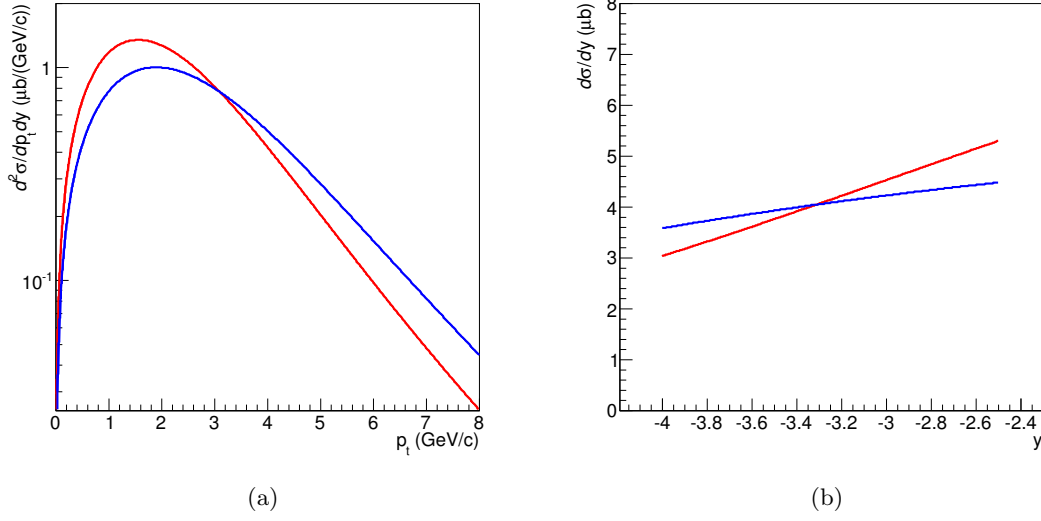


Figure 4.10:  $p_t$  and  $y$  differential shapes used for the MC simulation (red lines) and for the systematic evaluation (blue lines).

result of the fit (0.16) as an additional systematic uncertainty on  $\lambda_\theta$ . For consistency, the same evaluation was performed in the Collins-Soper frame.

The role of the systematic uncertainties from the trigger and tracking efficiency (both dependent on the muons  $p_t$  and, therefore, also on the  $J/\psi$   $p_t$ ) was also studied. The first one was evaluated by varying the efficiency values for each detector element by 2% with respect to the default values in the simulation. This percentage was chosen as four times the statistical error on the efficiency values, which is of the order of 0.5% for each local board (see Figure 4.6(b)). For the tracking part, the rather conservative choice of comparing the reference results, obtained with realistic dead channel maps, with those relative to an ideal detector set-up (*i.e.* a detector with no dead channels) was chosen. These two sources give a less important contribution to the overall systematic evaluation, with typical values of 0.03-0.04.

All the obtained values can be found in Table 4.2, as well as the total amount of systematic uncertainty evaluated by quadratically combining the results for the different contributions.

Table 4.2: Summary of the systematic uncertainties on the  $J/\psi$  polarization parameters estimation.

	$p_t(\text{GeV}/c)$	$\lambda_\theta^{\text{HE}}$	$\lambda_\phi^{\text{HE}}$	$\lambda_\theta^{\text{CS}}$	$\lambda_\phi^{\text{CS}}$
Signal	2-8	$\pm 0.10$	$\pm 0.02$	$\pm 0.05$	$\pm 0.05$
MC Input	2-3	$\pm 0.07$	$\pm 0.01$	$\pm 0.02$	$\pm 0.01$
	3-4	$\pm 0.05$	$\pm 0.04$	$\pm 0.03$	$\pm 0.02$
	4-8	$\pm 0.03$	$\pm 0.02$	$\pm 0.05$	$\pm 0.03$
Trig. Eff.	2-3	$\pm 0.08$	$\pm 0.03$	$\pm 0.02$	$< 0.005$
	3-4	$\pm 0.06$	$\pm 0.01$	$\pm 0.01$	$< 0.005$
	4-8	$< 0.005$	$\pm 0.02$	$\pm 0.04$	$\pm 0.03$
Track. Eff.	2-3	$\pm 0.03$	$\pm 0.02$	$\pm 0.07$	$\pm 0.04$
	3-4	$< 0.005$	$\pm 0.01$	$\pm 0.04$	$\pm 0.01$
	4-8	$< 0.005$	$\pm 0.02$	$\pm 0.02$	$\pm 0.03$
Fit range	2-3	$\pm 0.16$	-	$\pm 0.10$	-
Total	2-3	$\pm 0.21$	$\pm 0.04$	$\pm 0.13$	$\pm 0.07$
	3-4	$\pm 0.13$	$\pm 0.05$	$\pm 0.07$	$\pm 0.05$
	4-8	$\pm 0.10$	$\pm 0.04$	$\pm 0.08$	$\pm 0.07$

## 4.8 Results

The obtained results are shown in Figure 4.11 and reported in Table 4.3.

For both the reference frames and in all the explored range of  $p_t$  the  $\lambda_\theta$  and  $\lambda_\phi$  parameters are compatible with zero within uncertainties.

In the helicity reference frame there is a hint for a slightly longitudinal polarization at low  $p_t$  ( $1.6\sigma$  significance for  $2 < p_t < 3 \text{ GeV}/c$ ), which then progressively vanishes going towards higher transverse momenta.

In the Collins-Soper case the  $\lambda_\theta$  parameter is systematically slightly lower than zero, but everywhere compatible with no polarization. The magnitude of the systematical uncertainty is comparable with that of the statistical one: only in the first  $p_t$  bin the systematics are higher since one additional source was considered with respect to the other  $p_t$  bins (see Section 4.7).

Frame	$p_t$ (GeV/c)	$\langle p_t \rangle$ (GeV/c)	$\lambda_\theta$	$\lambda_\phi$
HE	2-3	2.5	$-0.36 \pm 0.09 \pm 0.21$	$0.05 \pm 0.04 \pm 0.04$
	3-4	3.5	$-0.20 \pm 0.11 \pm 0.13$	$0.01 \pm 0.05 \pm 0.05$
	4-8	5.2	$0.00 \pm 0.10 \pm 0.10$	$0.00 \pm 0.04 \pm 0.04$
CS	2-3	2.5	$-0.10 \pm 0.14 \pm 0.13$	$-0.04 \pm 0.08 \pm 0.07$
	3-4	3.5	$-0.06 \pm 0.14 \pm 0.07$	$-0.03 \pm 0.08 \pm 0.05$
	4-8	5.2	$-0.09 \pm 0.10 \pm 0.08$	$0.03 \pm 0.06 \pm 0.07$

Table 4.3:  $\lambda_\theta$  and  $\lambda_\phi$  parameters results in three  $p_t$  bins and for the helicity (HE) and Collins-Soper (CS) reference frames. Statistical and systematic errors are quoted separately.

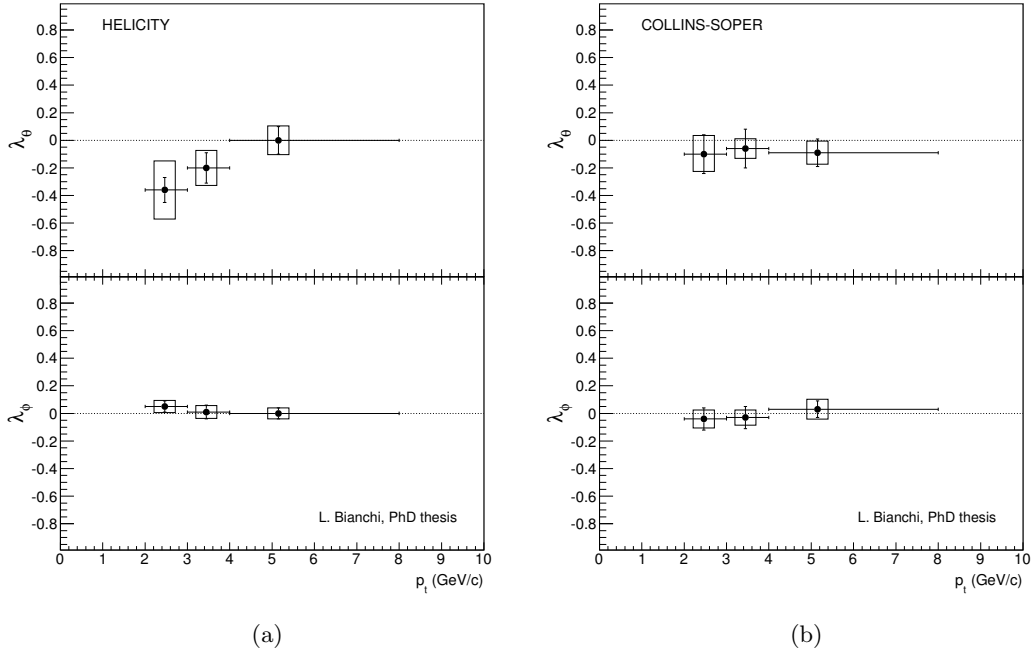


Figure 4.11: Polarization parameters measured in the helicity (a) and Collins-Soper (b) reference frames as a function of the transverse momentum of the  $J/\psi$ . The  $\lambda_\theta$  parameter is shown on top and the  $\lambda_\phi$  on bottom. Bars represent statistical errors, while boxes represent systematics.

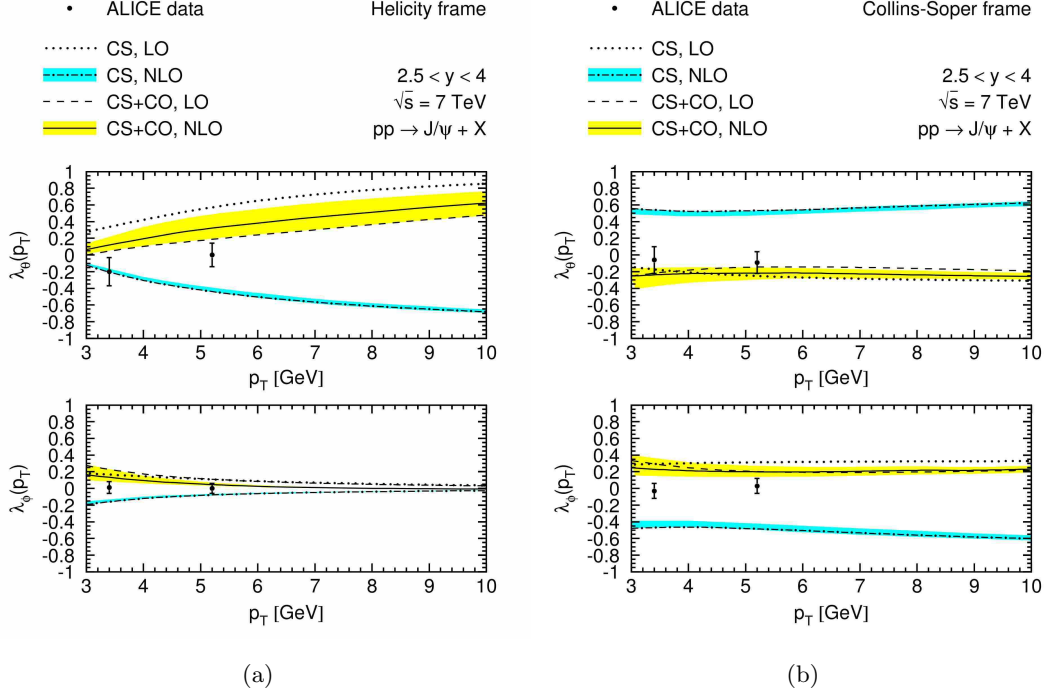


Figure 4.12: Polarization parameters  $\lambda_\theta$  and  $\lambda_\phi$  measured by ALICE in the helicity (a) and Collins-Soper (b) reference frames compared with NLO CSM (light blue band) and with NLO NRQCD (yellow band) [108].

As already discussed in Chapter 1 Section 1.7 and Chapter 2 Section 2.7.6, theoretical results on  $J/\psi$  hadro- and photo-production were published very recently [73, 108]. A new global fit to the color-octet long-distance terms of NRQCD was performed using data from Belle, Tevatron Run I and Run II, HERA Run I and Run II, RHIC, LEP II and LHC and the results were used to predict  $J/\psi$  polarization in photoproduction (see Section 2.7.6 for a comparison with ZEUS and H1 data) and hadroproduction.

In particular, NRQCD and CSM at NLO accuracy were used to determine the degree of polarization for direct  $J/\psi$  production in  $pp$  collisions at  $\sqrt{s} = 7$  TeV. These predictions, provided in the kinematical domain studied by the ALICE muon spectrometer, were compared with the results obtained with this analysis.

The comparison is shown in Figure 4.12. Theoretical curves extend only down to  $p_t = 3$  GeV/ $c$  since at lower transverse momenta the calculation is affected by divergencies. LO and NLO predictions are only slightly different for NRQCD, while the effect of the second order correction for CSM is much more important. Data slightly favour the

NRQCD approach, in particular in the Collins-Soper reference frame, even if for a conclusive comparison higher  $J/\psi$  transverse momenta must be studied experimentally. This will be probably possible profiting of the high-statistics data sample collected during 2011.

## 4.9 The role of the $\lambda_{\theta\phi}$ parameter

As already stated in Section 4.1, the  $\lambda_{\theta\phi}$  was assumed to be zero for this analysis. The reason is that some little statistical fluctuations on this parameter were found to introduced big effects on the extraction of the whole angular distribution, in particular in the bin  $3 < p_t < 4$  GeV/ $c$  and for the helicity reference frame.

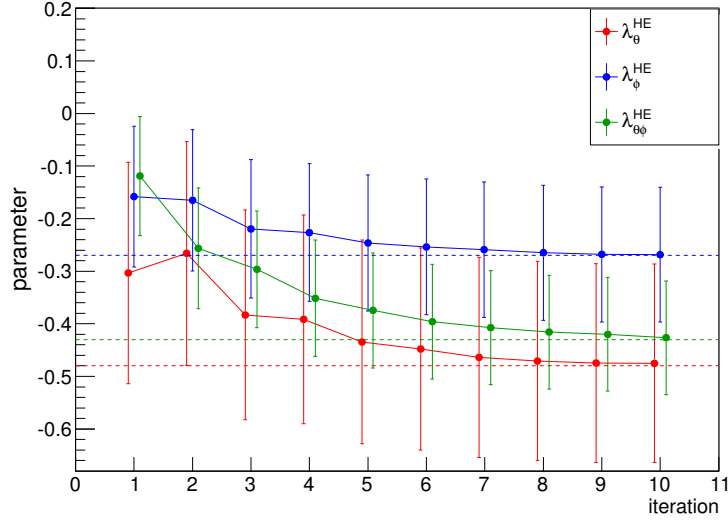


Figure 4.13:  $\lambda_{\theta}$ ,  $\lambda_{\phi}$  and  $\lambda_{\theta\phi}$  parameters estimated for  $3 < p_t < 4$  GeV/ $c$  in the helicity reference frame as a function of the iteration number. Errors are purely statistical.

For the estimation of the  $\lambda_{\theta\phi}$  parameter the signal was extracted in five bins of the  $|\tilde{\phi}|$  quantity (see Section 4.1):

$$[0, 0.628] - [0.628, 1.256] - [1.256, 1.884] - [1.884, 2.512] - [2.512, \pi]$$

with the same procedure described in Section 4.4 for the  $\cos\theta$  and  $\phi$  variables. The measured yields were corrected for the  $A \times \epsilon$  projected in the  $\tilde{\phi}$  variable and the iterative procedure was extended to the new parameter.

In Figure 4.13 the values estimated for the three polarization parameters after the fit



to the corrected spectra in the  $3 < p_t < 4$  GeV/ $c$  bin are plotted as a function of the iteration number for the case of no  $\mathcal{F}$  constraint requirement<sup>1</sup>. What is clear from the figure is that the parameters assume progressively lower values as the number of the iteration increases and this behaviour stops only after 7-8 iterations. This is a completely different situation with respect to the iteration plots shown in Section 4.5, where the convergence was observed after just 2-3 iterations. Moreover, the values to which the iterative procedure converges when  $\lambda_{\theta\phi}$  is introduced are quite extreme for this  $p_t$  bin, while in all the other bins (and also for the Collins-Soper frame) the results are similar to what obtained with the default procedure.

The  $\lambda_{\theta\phi} = 0$  assumption was checked by correcting the extracted yields in the  $|\tilde{\phi}|$  bins with the MC tuned at the last iteration in the determination of  $\lambda_\theta$  and  $\lambda_\phi$  with the default approach. If the corrected spectrum turns out to be not compatible with a flat distribution, then the assumption has to be re-checked, while if that is the case, the conclusion is that the bias due to the assumption is negligible.

This procedure is different from the tuning of all the three parameters together with an iterative approach, since little statistical fluctuations in the  $\tilde{\phi}$  distribution cannot be magnified iteration after iteration. This *a – posteriori* check was repeated for each bin in  $p_t$  and for the two reference frames.

The result of the check is shown in Figure 4.14 and supports the assumption of a zero  $\lambda_{\theta\phi}$ : the corrected distributions are everywhere compatible with a flat trend and a fit with a zero-degree polynomial function gives a  $\chi^2/ndf$  lower than 1.3 for all the bins and for both the frames.

---

<sup>1</sup>Not imposing the  $\mathcal{F}$  constraint is not an issue here since it was verified (see Appendix D) that the results obtained with and without the constraint are in agreement.

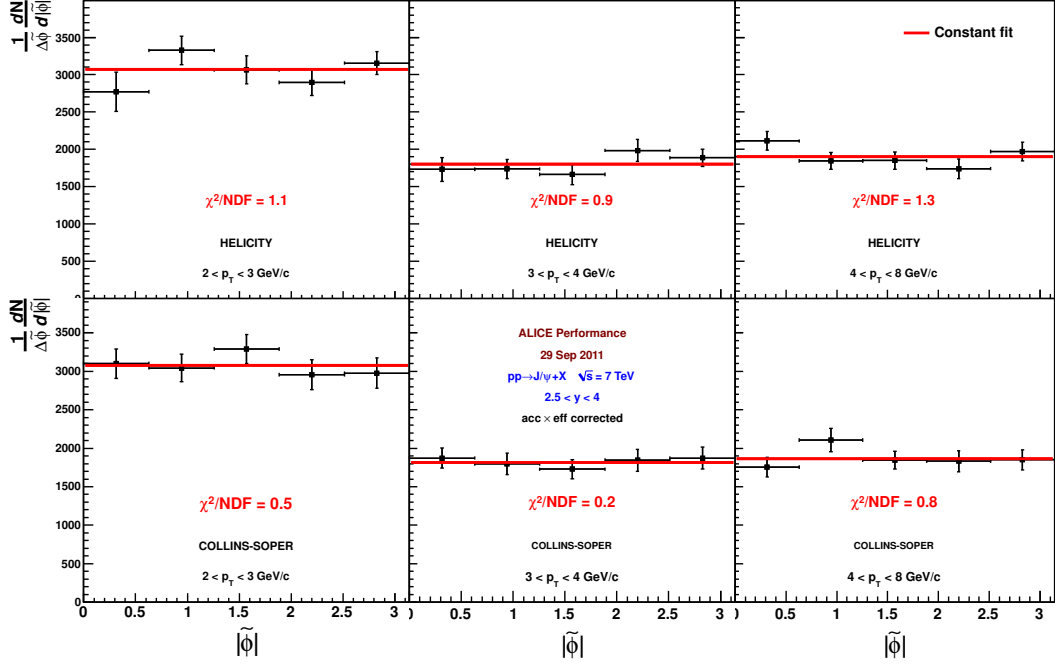


Figure 4.14:  $\tilde{\phi}$  corrected spectra for the helicity (first row) and the Collins-Soper (second row) reference frames in the three  $p_t$  bins (from left to right). A  $\times \epsilon$  correction made with the MC tuned with  $\lambda_\theta$  and  $\lambda_\phi$  coming from the final results in each  $p_t$  bin and with a  $\lambda_{\theta\phi}=0$  assumption. The red line represents the zero-polynomial fit to the spectra.

This result cannot be considered as a measurement of  $\lambda_{\theta\phi}$ , since the only way to have a solid final number for this parameter is to use the iterative approach for all the angular variables. Nevertheless, this check gives a very important hint on the flatness of the  $\tilde{\phi}$  corrected spectrum and makes the case of a  $\lambda_{\theta\phi}=0$  for all the bins: this point reassures on the solidness of the result for the other two parameters obtained with an  $A \times \epsilon$  coming from a MC with a  $\lambda_{\theta\phi}=0$  input.

## 4.10 The role of the non-prompt component

The muon spectrometer allows the measurement of inclusive  $J/\psi$  production: the determination of the non-prompt ( $J/\psi$  coming from the decay of B-hadrons) and of the direct ( $J/\psi$  coming from the decay of higher  $c\bar{c}$  states as  $\psi(2S)$  and  $\chi_c$ ) components is not possible since the secondary vertex is not reconstructible for tracks emitted at

forward rapidity (the ALICE vertex detector doesn't cover this rapidity region). Unfortunately, theoretical predictions on quarkonium polarization are usually given for prompt or even direct production, since the inclusion of the decay effects is not trivial from the theoretical point of view. It is therefore important to estimate by how much the results can change if only the prompt component would have been measured. As discussed in Chapter 1 Section 1.6.4, the LHCb experiment was able to extract both the prompt and non-prompt  $J/\psi$  cross-sections in the kinematical domain  $p_t < 15$  GeV/c and  $2 < y < 4.5$  [68], as shown in Figure 4.15. Starting from this measurement, it is possible to extract the fraction of  $J/\psi$  coming from B decay in the inclusive sample for the ALICE kinematics, which are a subrange of the LHCb ones. The calculation gives 10% for  $2 < p_t < 3$  GeV/c, 13% for  $3 < p_t < 4$  GeV/c and 15% for  $4 < p_t < 8$  GeV/c, where the increasing trend reflects the expected harder  $p_t$  dependence of the cross section for  $J/\psi$  production coming from B decay with respect to the prompt production.

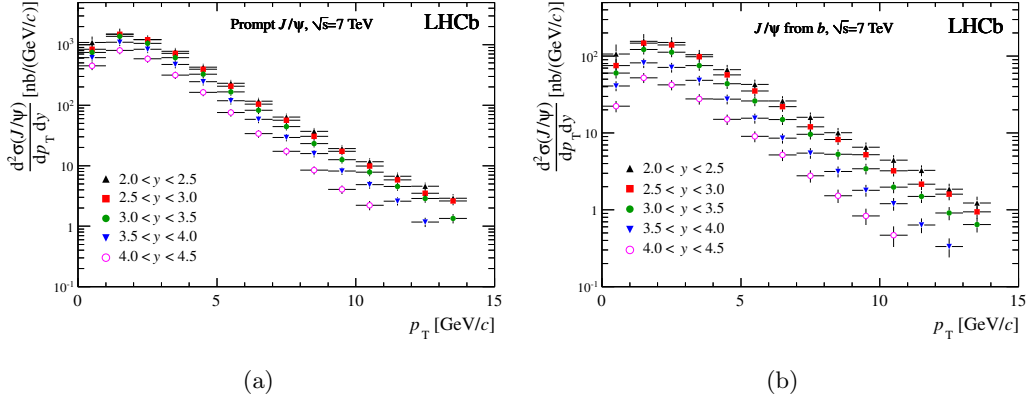


Figure 4.15: Differential  $p_t$  cross section for prompt (a) and non-prompt (b)  $J/\psi$  production at the LHC as measured by the LHCb experiment.

From BaBar experiment's measurements it is possible to have an estimate on the degree of polarization of non-prompt  $J/\psi$  with respect to the B hadron momentum direction<sup>2</sup>, which is the natural axis to be considered. The values in the helicity frame are:

$$\lambda_\theta = -0.196 \pm 0.044 \quad \text{for } p < 1.1 \text{ GeV}/c$$

<sup>2</sup>The measurement refers to the  $\Upsilon(4S)$  center of mass frame, but simulation in BaBar's kinematical domain show that the rms spread of the difference between this definition and the one referring to the B hadron momentum is only 0.085 in  $\cos\theta_{HE}$

$$\lambda_\theta = -0.592 \pm 0.032 \quad \text{for } p > 1.1 \text{ GeV}/c$$

where  $p$  is the  $J/\psi$  momentum in the laboratory reference frame.

This sizable polarization is expected to be highly diluted when the chosen axis is the  $J/\psi$  direction in the laboratory frame, which is the one used when the inclusive measurement is performed. MC studies carried out by the LHCb collaboration [68] (*i.e.* in the same kinematical domain of ALICE) confirm this expectation. Moreover, the CDF experiment measured the polarization of non-prompt  $J/\psi$  with respect to the  $J/\psi$  direction in the laboratory frame (see Chapter 2 Section 2.7.1 and [91]) and found  $\lambda_\theta = -0.106 \pm 0.033(\text{stat}) \pm 0.007(\text{syst})$ , confirming again the expected dilution of the polarization in a different kinematical domain.

It is therefore possible to make an estimation of what would be the  $\lambda_\theta$  value if the non-prompt component could be subtracted from the data sample; for each  $p_t$  bin it is sufficient to:

1. simulate a reference  $\cos\theta$  spectrum with a  $\lambda_\theta$  corresponding to the one measured for that  $p_t$  bin and with  $N$  entries;
2. assume two “extreme” limits for the  $\lambda_\theta$  parameter for non-prompt  $J/\psi$  ( $\lambda_\theta^{J/\psi \leftarrow B}$ ) and simulate a  $\cos\theta$  spectrum for each assumption with  $N \cdot R_{J/\psi \leftarrow B}$  entries, where  $R_{J/\psi \leftarrow B}$  is the fraction of  $J/\psi$  coming from B in the inclusive sample for the considered  $p_t$  bin. The two assumptions made for  $\lambda_\theta^{J/\psi \leftarrow B}$  are  $\pm 0.2$ , conservatively doubling the value measured by CDF;
3. subtract from the reference spectrum the non-prompt spectrum for the upper (lower) assumption for  $\lambda_\theta^{J/\psi \leftarrow B}$  obtained in the previous step;
4. re-fit with a quadratic shape the two new spectra obtained and extract the  $\lambda_\theta$  values corresponding to the two assumptions.

In this way, two values for the  $\lambda_\theta$  parameter for each  $p_t$  bin are obtained, corresponding to the upper and lower limits for a prompt measurement, given the inclusive result reported in Table 4.3. The result is shown on Figure 4.16 and the general outcome is that the discrepancy between the prompt and the inclusive measurement of  $\lambda_\theta$  is not higher than 0.05 for all the  $p_t$  bins: the conclusion is that the result obtained for inclusive production is also a good estimation for the prompt component, the difference being well inside the systematical errors of the measurement.

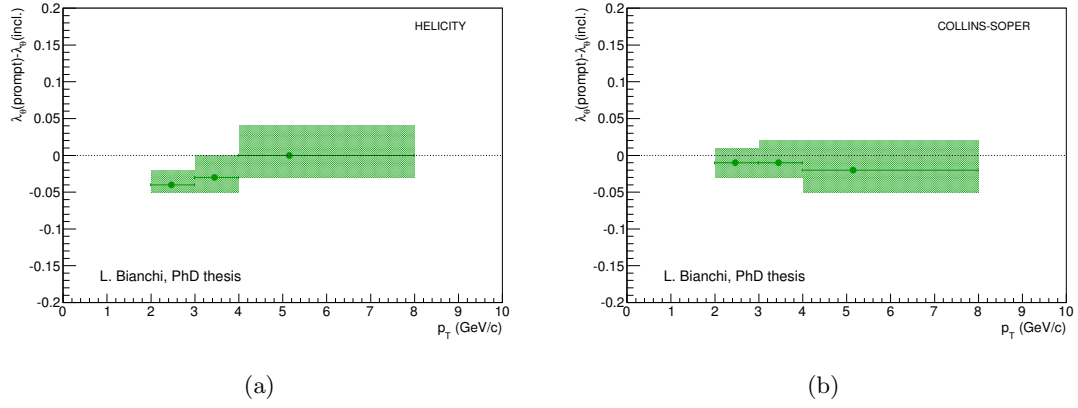


Figure 4.16: Difference between the measured  $\lambda_\theta$  and the value of the same parameter for prompt  $J/\psi$ . The green area correspond to the region between the values obtained making the extreme assumptions  $\lambda_\theta(J/\psi \leftarrow B) = \pm 0.2$ ; the marker is the value obtained when considering  $\lambda_\theta(J/\psi \leftarrow B) = 0$ . The case of the helicity frame is shown in (a), the case of the Collins-Soper one in (b).

# Conclusions

In this thesis the first results on  $J/\psi$  polarization at the LHC energies was presented. Such results, obtained making use of data collected by ALICE during 2010, are eagerly awaited by the heavy quarkonium scientific community, since they can help in solving the long standing puzzle of quarkonium hadroproduction which, after almost forty years from the  $J/\psi$  discovery, is still an open issue.

The analysis of the anisotropies in the directions of the  $J/\psi$  decay products, quantified with the three parameters  $\lambda_\theta$ ,  $\lambda_\phi$  and  $\lambda_{\theta\phi}$ , was used to extract polarization. In particular, when  $\lambda_\theta$  is +1 the polarization is transverse, while when  $\lambda_\theta$  is -1 the polarization is longitudinal.

ALICE studied inclusive- $J/\psi$  polarization in the muonic decay channel dividing the signal in three  $p_t$  bins:  $2 < p_t < 3$  GeV/ $c$ ,  $3 < p_t < 4$  GeV/ $c$  and  $4 < p_t < 8$  GeV/ $c$ . The parameters  $\lambda_\theta$  and  $\lambda_\phi$  were extracted in two different reference frames (helicity and Collins-Soper), while  $\lambda_{\theta\phi}$  was assumed to be zero: this assumption was verified *a posteriori* to be realistic.

The result of this analysis is that no significant polarization is observed in both the considered frames: a hint for a slightly longitudinal value of  $\lambda_\theta$  at low  $p_t$  in the helicity reference frame can be found, but only at the  $1.6\sigma$  significance level. In the Collins-Soper frame  $\lambda_\theta$  is systematically slightly lower than zero, but everywhere compatible with no polarization. The  $\lambda_\phi$  parameter is found to be consistent with zero in all the  $p_t$  bins and for the two reference frames.

The comparison of the results with very recent theoretical predictions of NRQCD and CSM at full NLO accuracy was carried out. None of the two theoretical curves provides a perfect description of the data in both frames, but a better agreement with NRQCD can be found, in particular in the Collins-Soper reference frame, where the

strongly transverse polarization expected by the CSM is not observed.

It has to be noted that ALICE's results are for inclusive  $J/\psi$  production, while the theoretical curves are given for direct  $J/\psi$ . However, in our kinematic domain, the effect of the non prompt component ( $J/\psi$  from  $B$  decays) has been shown to be negligible and the contribution of higher mass charmonia ( $\chi_c$  and  $\psi(2S)$ ) should not have a very strong impact on the polarization parameters [73].

A conclusive comparison data-theory requires the experiments to probe higher  $J/\psi$  transverse momenta and, in ALICE, this will be possible exploiting the higher statistics data sample collected during 2011. Finally, results on  $\Upsilon$  polarization at the LHC are within reach and would provide further constraints to the theory and a new testing ground for the factorization approach at the basis of the description of heavy quarkonia production.

## Appendix A

# Analysis dimensionality and acceptance bias

When the analysis strategy involves the integration of the signal over one kinematical variable, the acceptance correction can be biased if the differential distribution injected in the MC simulation for the integrated variable is not known a priori.

To illustrate this point we suppose to be interested in a physical quantity which depends on two kinematical variables:  $\cos\theta$  and  $\phi$ . If we are able to extract the signal in a two-dimensional (2D) approach, the correction for the detector acceptance can be applied in the following way:

$$\begin{aligned}\text{CORR}(\cos\theta, \phi) &= \text{REC}_{\text{data}}(\cos\theta, \phi) \cdot \text{ACC}^{-1}(\cos\theta, \phi) = \\ &= \text{REC}_{\text{data}}(\cos\theta, \phi) \cdot \frac{\text{GEN}_{\text{MC}}(\cos\theta, \phi)}{\text{REC}_{\text{MC}}(\cos\theta, \phi)}.\end{aligned}$$

If we want to extract a one-dimensional (1D) corrected spectrum, it is then sufficient to perform an integration on the 2D distribution:

$$\begin{aligned}\{\text{CORR}(\cos\theta)\}^{1\text{D} \leftarrow 2\text{D}} &= \int d\phi \text{CORR}(\cos\theta, \phi) = \\ &= \int d\phi \text{REC}_{\text{data}}(\cos\theta, \phi) \cdot \frac{\text{GEN}_{\text{MC}}(\cos\theta, \phi)}{\text{REC}_{\text{MC}}(\cos\theta, \phi)} \quad (\text{A.1})\end{aligned}$$

On the contrary, when we extract the signal in a 1D approach, *i.e.* integrating over one of the two variables, what we do is:

$$\text{REC}_{\text{data}}(\cos\theta) = \int d\phi \text{REC}_{\text{data}}(\cos\theta, \phi) \quad , \quad \text{ACC}(\cos\theta) = \frac{\int d\phi \text{REC}_{\text{MC}}(\cos\theta, \phi)}{\int d\phi \text{GEN}_{\text{MC}}(\cos\theta, \phi)}$$



↓

$$\{\text{CORR}(\cos \theta)\}^{1\text{D}} = \int d\phi \text{REC}_{\text{data}}(\cos \theta, \phi) \frac{\int d\phi \text{GEN}_{\text{MC}}(\cos \theta, \phi)}{\int d\phi \text{REC}_{\text{MC}}(\cos \theta, \phi)} \quad (\text{A.2})$$

The last expression is, in general, different from Eq. A.1 and this is the reason why the integration of the signal can introduce a bias in the acceptance correction. The only case for which the two results in Eq. A.1 and A.2 coincide is when

$$\text{REC}_{\text{data}}(\cos \theta, \phi) = \text{REC}_{\text{MC}}(\cos \theta, \phi),$$

*i.e.* when the reconstructed spectrum in the MC overlaps with the reconstructed spectrum from real data. If the geometrical description and the efficiency of the detector are well taken into account in the simulation, this happens only when the dependence of the physical quantity under study on the integrated kinematical variable is known *a priori* and is injected in the MC simulation.

In the analysis described in Chapter 4, the signal is integrated over the rapidity and over the angular variable which is not under study ( $\phi$  when we analyze the  $\cos\theta$  distribution,  $\cos\theta$  when we analyze the  $\phi$  distribution): the integration over the angular variables is therefore a problem, since the behaviour is not known and rather represents the outcome of the analysis. For this reason an iterative procedure was adopted: in this approach the kinematical inputs in the simulation are adjusted iteration after iteration and the final correction is performed with a suitably polarized MC.

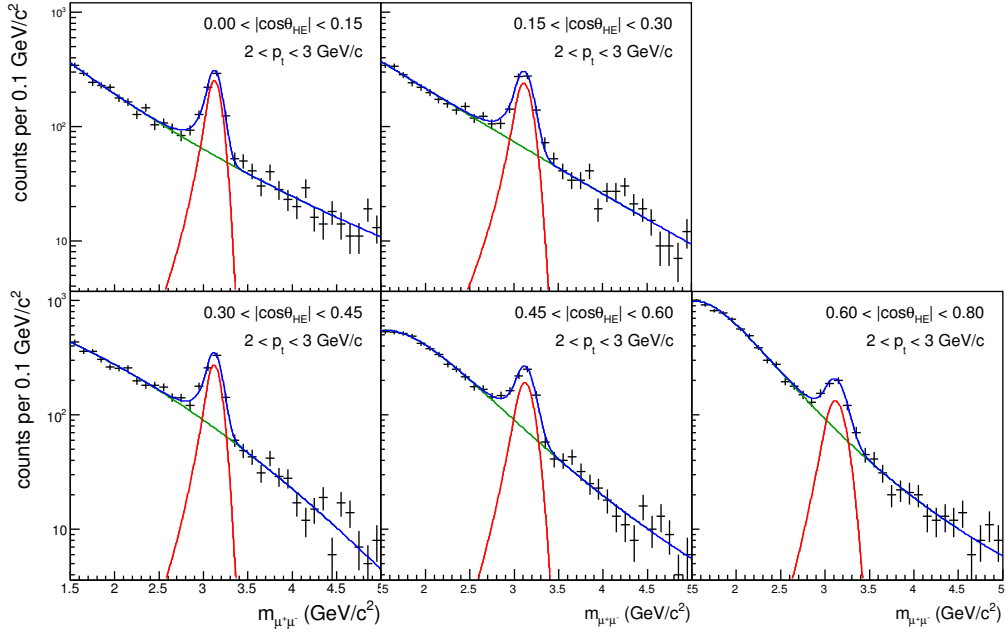
## Appendix B

# Invariant mass Fits

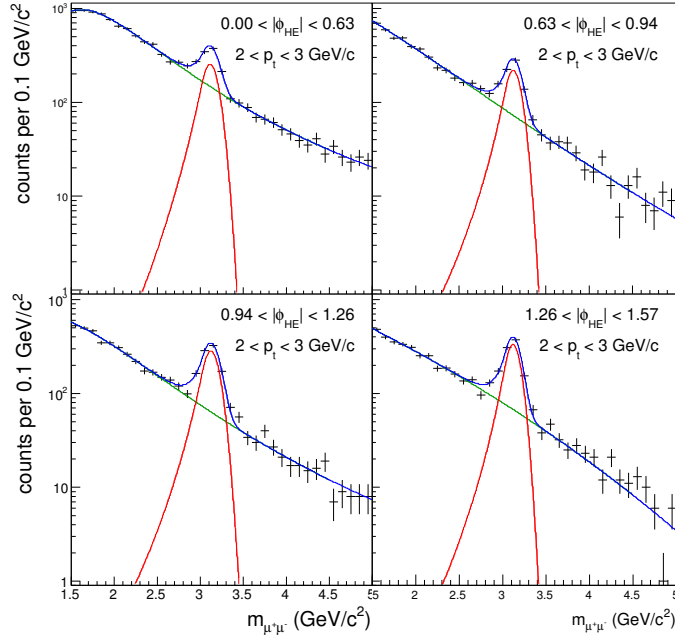
In this appendix more details on the fits to the invariant mass spectra for each bin of  $|\cos\theta|$  and  $|\phi|$ , for the three bins of  $p_t$  considered and for the Collins Soper and helicity reference frames are reported. The fitting function consists of a Crystal Ball plus a gaussian with continuously varying width (for more details see Chapter 4 Section 4.4). In Table B.1 the  $\tilde{\chi}^2 = \chi^2/\text{ndf}$ , the S/B ratio in a  $\pm 3\sigma$  window with respect to the CB peak and the number of  $J/\psi$  extracted for each bin are shown. The fits are then displayed in all the Figures from B.1 to B.6.

Table B.1:  $\tilde{\chi}^2$ , S/B and  $N_{J/\psi}$  from the fit to the invariant mass distributions of each bin in the kinematical variables.

spec.	bin	2 < p <sub>t</sub> < 3GeV/c			3 < p <sub>t</sub> < 4GeV/c			4 < p <sub>t</sub> < 8GeV/c		
		$\tilde{\chi}^2$	S/B	$N_{J/\psi}$	$\tilde{\chi}^2$	S/B	$N_{J/\psi}$	$\tilde{\chi}^2$	S/B	$N_{J/\psi}$
$\cos\theta_{\text{HE}}$	0.00-0.15	0.86	1.99	586 $\pm$ 32	1.08	3.04	342 $\pm$ 25	1.19	3.00	400 $\pm$ 27
	0.15-0.30	1.03	1.60	649 $\pm$ 38	0.99	2.52	336 $\pm$ 25	2.07	3.75	474 $\pm$ 31
	0.30-0.45	1.34	1.55	638 $\pm$ 39	1.34	1.89	359 $\pm$ 27	0.77	2.50	392 $\pm$ 25
	0.45-0.60	0.65	1.09	531 $\pm$ 42	1.28	1.35	370 $\pm$ 31	1.02	1.13	327 $\pm$ 30
	0.60-0.80	0.81	0.72	303 $\pm$ 30	0.85	0.65	246 $\pm$ 30	1.45	0.74	401 $\pm$ 34
$\phi_{\text{HE}}$	0.00-0.63	0.49	0.74	667 $\pm$ 95	1.11	0.51	327 $\pm$ 71	0.95	0.63	463 $\pm$ 50
	0.63-0.94	1.19	1.31	555 $\pm$ 38	1.32	1.42	340 $\pm$ 28	0.86	1.54	439 $\pm$ 32
	0.94-1.26	1.15	1.92	760 $\pm$ 44	1.06	2.50	472 $\pm$ 29	0.93	2.51	554 $\pm$ 31
	1.26-1.57	1.60	2.14	794 $\pm$ 40	1.01	3.65	567 $\pm$ 31	1.05	3.77	640 $\pm$ 32
$\cos\theta_{\text{CS}}$	0.00-0.15	1.51	1.45	1064 $\pm$ 54	1.18	1.22	601 $\pm$ 44	0.91	0.96	658 $\pm$ 52
	0.15-0.30	1.13	1.30	827 $\pm$ 50	1.08	1.19	479 $\pm$ 40	1.00	0.96	479 $\pm$ 40
	0.30-0.45	1.05	1.09	580 $\pm$ 45	1.14	1.74	396 $\pm$ 31	1.21	1.35	379 $\pm$ 31
	0.45-0.60	1.13	1.28	297 $\pm$ 27	1.47	2.19	200 $\pm$ 19	1.55	2.19	263 $\pm$ 23
	0.60-0.80	1.30	0.85	96 $\pm$ 40	0.97	1.48	116 $\pm$ 17	0.81	2.19	298 $\pm$ 24
$\phi_{\text{CS}}$	0.00-0.63	0.76	0.66	772 $\pm$ 108	0.91	0.50	477 $\pm$ 41	1.06	0.34	484 $\pm$ 47
	0.63-0.94	0.94	1.42	624 $\pm$ 43	1.32	1.47	355 $\pm$ 29	1.02	1.52	437 $\pm$ 33
	0.94-1.26	1.03	2.08	748 $\pm$ 39	0.80	2.67	441 $\pm$ 29	0.87	3.19	557 $\pm$ 32
	1.26-1.57	0.86	1.93	688 $\pm$ 39	0.62	3.68	503 $\pm$ 29	1.35	5.13	583 $\pm$ 30



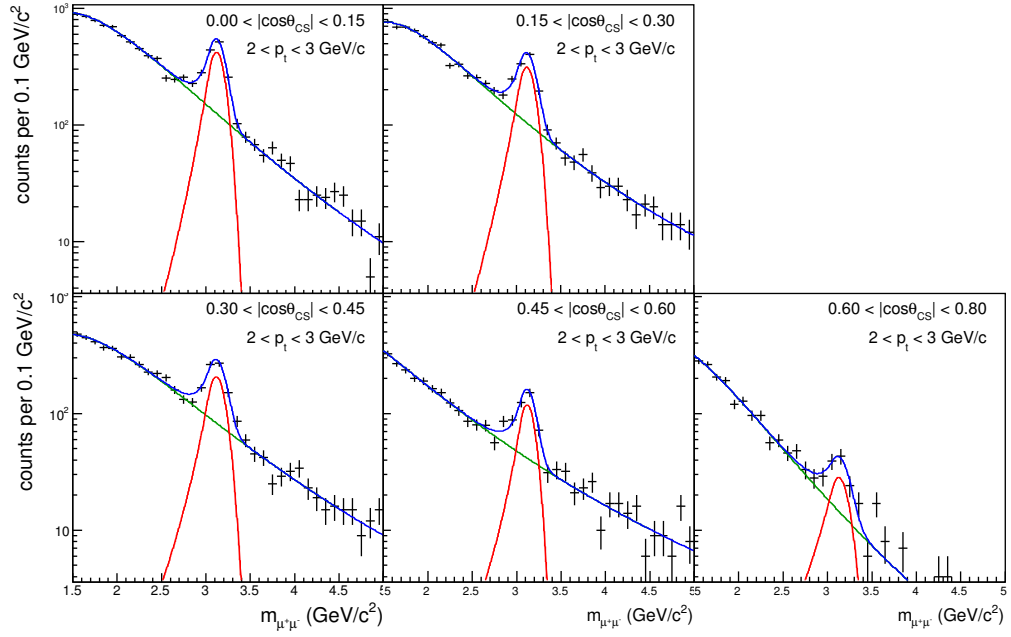
(a)



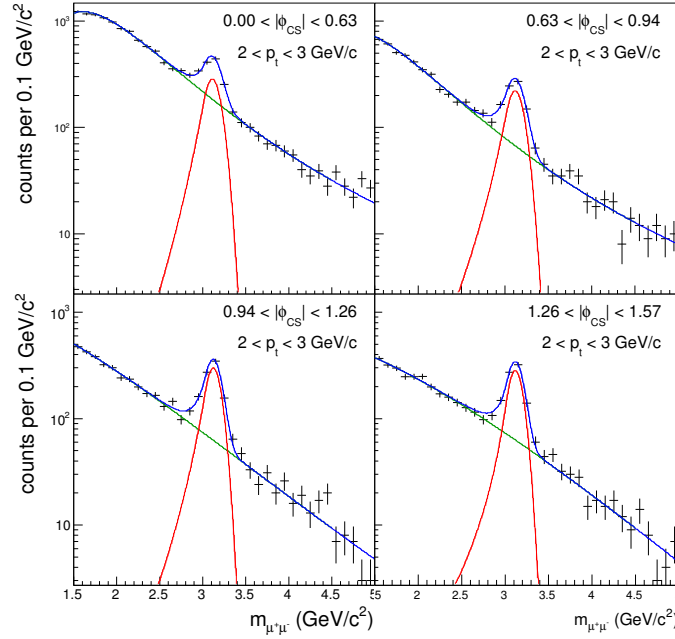
(b)

Figure B.1: Invariant mass of opposite sign muon pairs in the five bins of  $|\cos\theta_{\text{HE}}|$ (a) and in the four bins of  $|\phi_{\text{HE}}|$ (b) for  $2 < p_t < 3 \text{ GeV}/c$ . The fit to each spectrum is plotted as a blue line.

## Appendix B

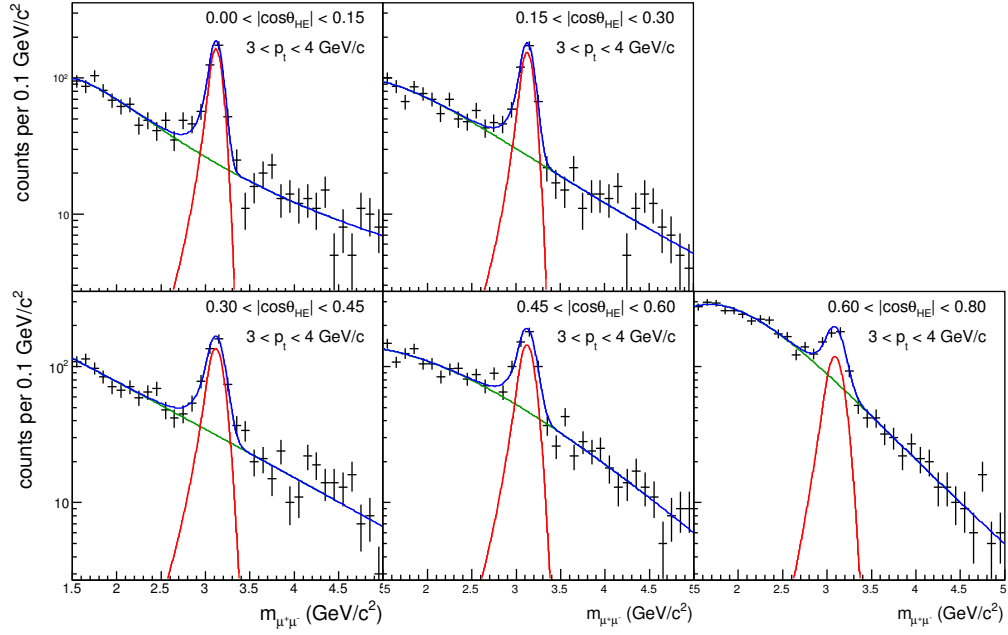


(a)

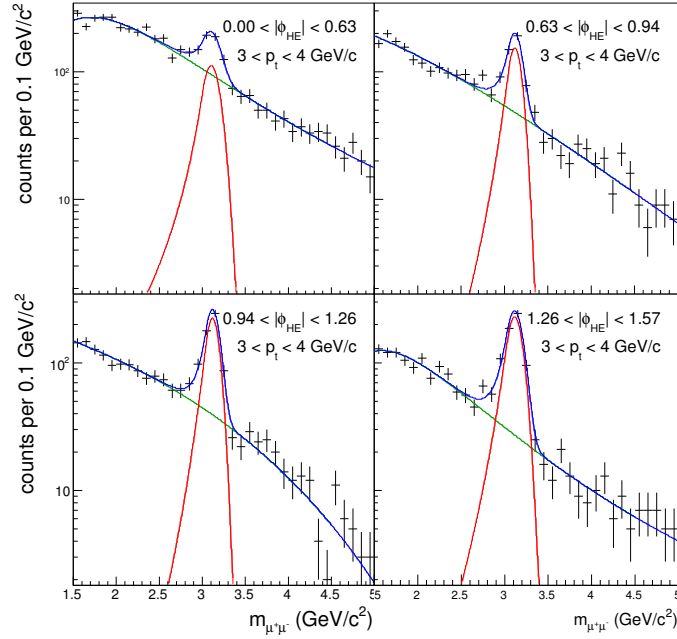


(b)

Figure B.2: Invariant mass of opposite sign muon pairs in the five bins of  $|\cos\theta_{CS}|$ (a) and in the four bins of  $|\phi_{CS}|$ (b) for  $2 < p_t < 3$  GeV/c. The fit to each spectrum is plotted as a blue line.



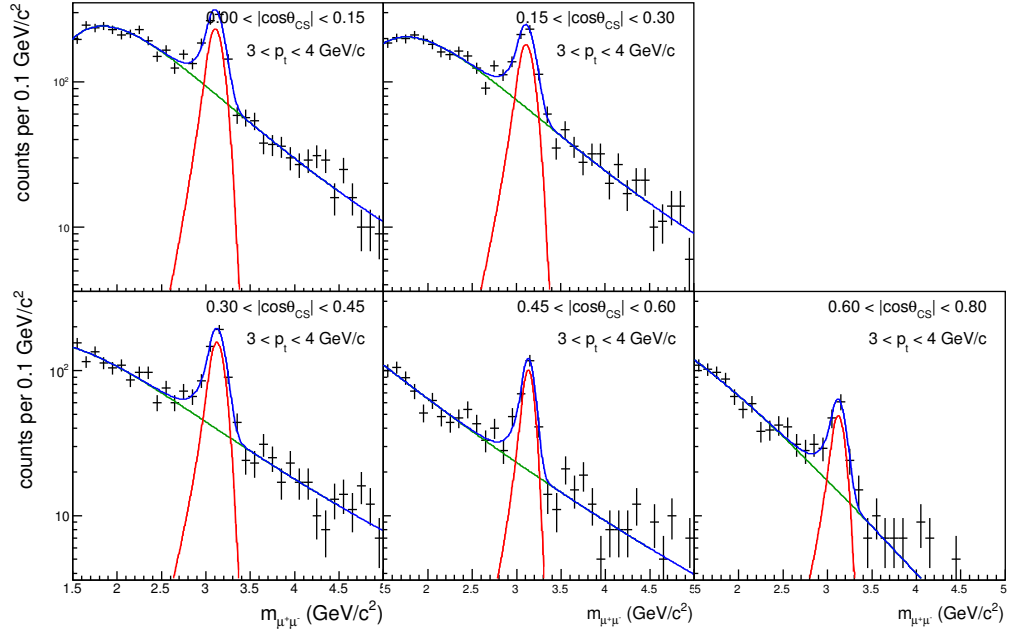
(a)



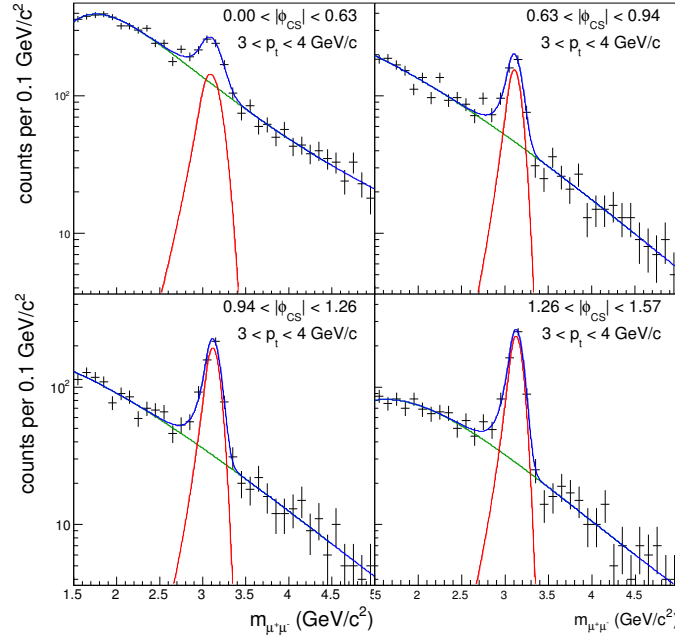
(b)

Figure B.3: Invariant mass of opposite sign muon pairs in the five bins of  $|\cos\theta_{HE}|$ (a) and in the four bins of  $|\phi_{HE}|$ (b) for  $3 < p_t < 4$  GeV/c. The fit to each spectrum is plotted as a blue line.

## Appendix B

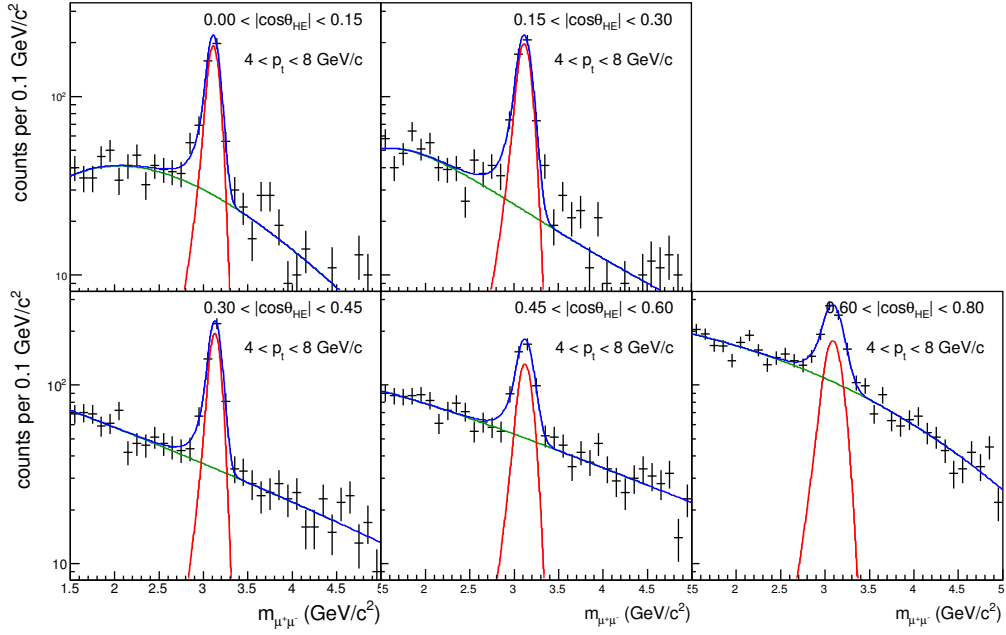


(a)

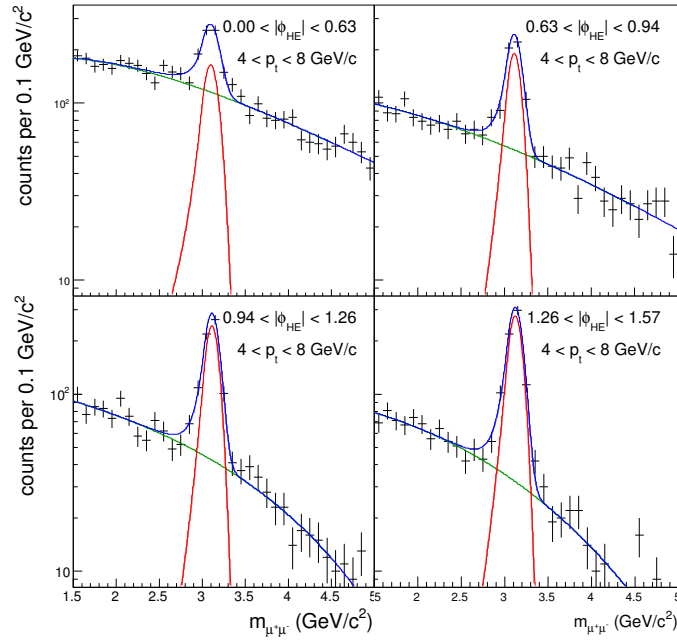


(b)

Figure B.4: Invariant mass of opposite sign muon pairs in the five bins of  $|\cos\theta_{CS}|$ (a) and in the four bins of  $|\phi_{CS}|$ (b) for  $3 < p_t < 4$  GeV/c. The fit to each spectrum is plotted as a blue line.



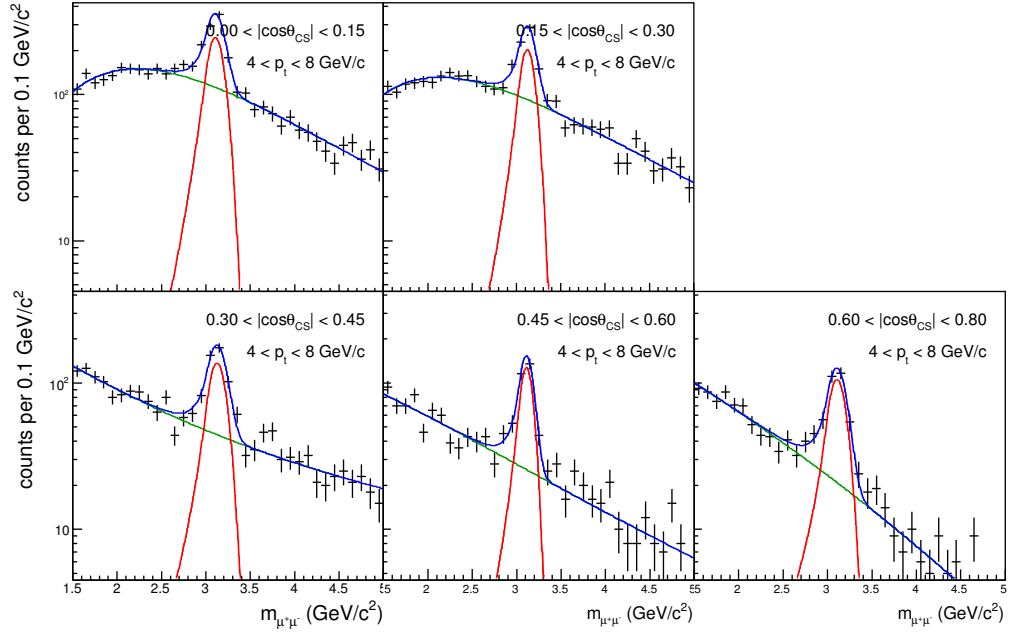
(a)



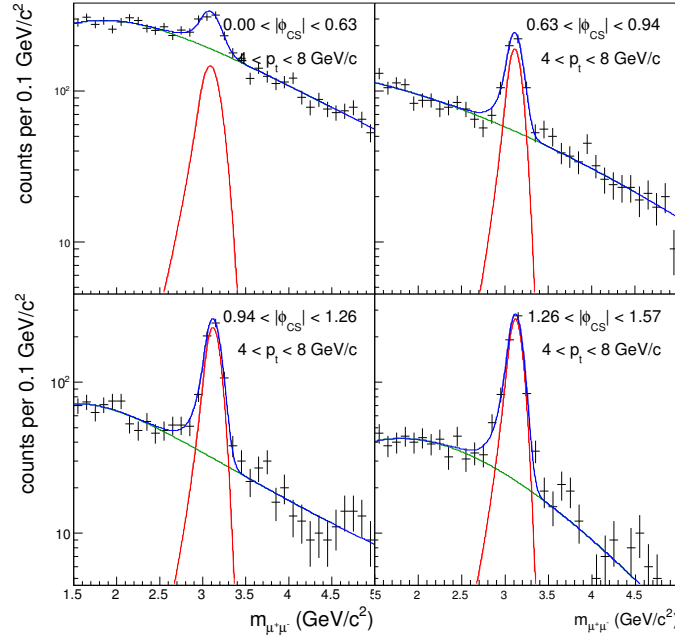
(b)

Figure B.5: Invariant mass of opposite sign muon pairs in the five bins of  $|\cos\theta_{HE}|$ (a) and in the four bins of  $|\phi_{HE}|$ (b) for  $4 < p_t < 8$  GeV/c. The fit to each spectrum is plotted as a blue line.

## Appendix B



(a)



(b)

Figure B.6: Invariant mass of opposite sign muon pairs in the five bins of  $|\cos\theta_{CS}|$ (a) and in the four bins of  $|\phi_{CS}|$ (b) for  $4 < p_t < 8$  GeV/c. The fit to each spectrum is plotted as a blue line.





## Appendix C

### Fits to the corrected spectra

The results of the fits to the  $A \times \epsilon$  corrected spectra are here shown for the three  $p_t$  bins under study. The fits were performed in a simultaneous way in the two reference frames, with the additional requirement:

$$\mathcal{F} = \frac{\lambda_{\theta}^{HE} + 3\lambda_{\phi}^{HE}}{1 - \lambda_{\phi}^{HE}} = \frac{\lambda_{\theta}^{CS} + 3\lambda_{\phi}^{CS}}{1 - \lambda_{\phi}^{CS}}$$

(see Chapter 4 Section 4.6 for more details). Only statistical errors are plotted and the fits are shown as red lines.

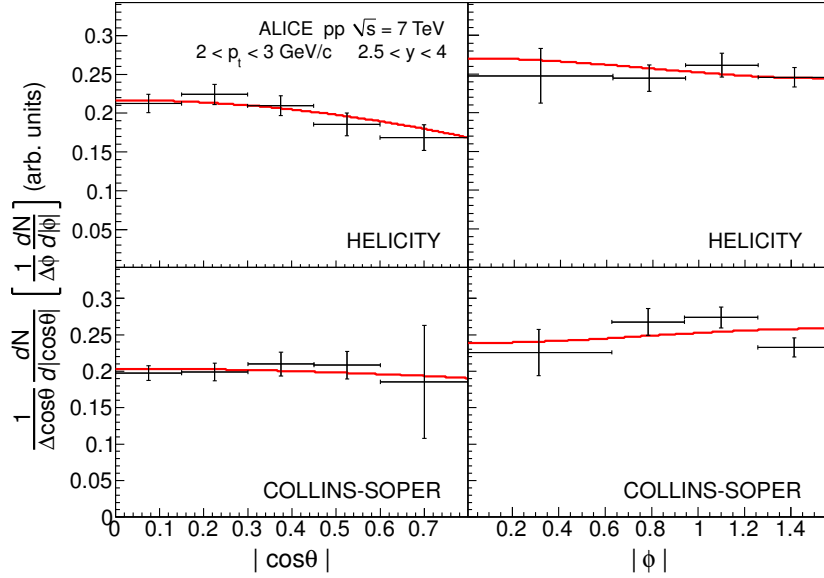


Figure C.1: Fit to the corrected spectra:  $2 < p_t < 3$  GeV/ $c$ .

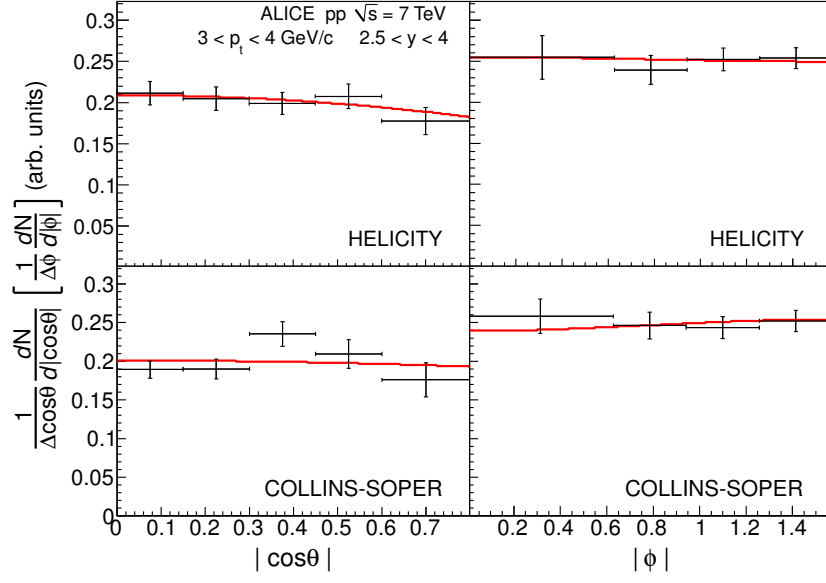


Figure C.2: Fit to the corrected spectra:  $3 < p_t < 4$  GeV/ $c$ .

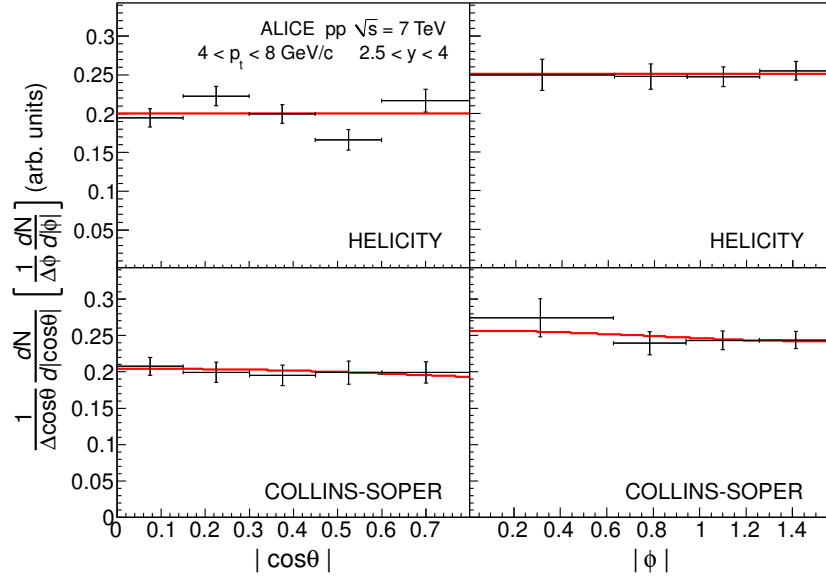


Figure C.3: Fit to the corrected spectra:  $4 < p_t < 8$  GeV/ $c$ .

## Appendix D

# Checks on the analysis procedure

Many tests on the analysis procedure described in Chapter 4 were performed, in particular for what concerns the iterative approach and the simultaneous fit to the corrected spectra. In the following sections the description and the outcome of these checks are given.

### D.0.1 Iterative procedure

As already motivated in Chapter 4 Section 4.5, the iterative procedure is a powerful method when, due to statistics restrictions, an integration over one variable is needed and when the correlation between this variable and the others under study is not known a priori. The convergence of the method has been verified, but the fact that the procedure converges to the correct values has to be checked carefully. In particular, if many local minima of the difference  $|\lambda_{\theta}^{inMC} - \lambda_{\theta}^{result}|$  are present in the parameters' allowed region, one could find that the procedure converges to different values if the iterative correction starts from differently polarized MC samples.

A first test consists in starting the procedure from  $A \times \epsilon$  obtained from very differently polarized MC samples, checking if the iterations in the different cases lead to the same result. This test was performed on two differently polarized MC samples of  $\sim 10^6$  J/ $\psi$  events:

$$\text{TEST1 : } \quad \lambda_{\theta}^{\text{HE}} = 0.88 \quad , \quad \lambda_{\phi}^{\text{HE}} = -0.99 \quad , \quad \lambda_{\theta}^{\text{CS}} = 0.00 \quad , \quad \lambda_{\phi}^{\text{CS}} = -0.50$$

$$\text{TEST2 : } \quad \lambda_{\theta}^{\text{HE}} = -1.00 \quad , \quad \lambda_{\phi}^{\text{HE}} = 0.00 \quad , \quad \lambda_{\theta}^{\text{CS}} = -1.00 \quad , \quad \lambda_{\phi}^{\text{CS}} = 0.00$$

In both cases the iterative procedure was started from four differently polarized acceptances:

$$\text{START1 : } \lambda_{\theta}^{\text{HE}} = 1.00 \text{ , } \lambda_{\phi}^{\text{HE}} = 1.00 \text{ , } \lambda_{\theta}^{\text{CS}} = 1.00 \text{ , } \lambda_{\phi}^{\text{CS}} = 1.00$$

$$\text{START2 : } \lambda_{\theta}^{\text{HE}} = 0.00 \text{ , } \lambda_{\phi}^{\text{HE}} = 0.00 \text{ , } \lambda_{\theta}^{\text{CS}} = 0.00 \text{ , } \lambda_{\phi}^{\text{CS}} = 0.00$$

$$\text{START3 : } \lambda_{\theta}^{\text{HE}} = 1.00 \text{ , } \lambda_{\phi}^{\text{HE}} = 0.00 \text{ , } \lambda_{\theta}^{\text{CS}} = 1.00 \text{ , } \lambda_{\phi}^{\text{CS}} = 0.00$$

$$\text{START4 : } \lambda_{\theta}^{\text{HE}} = 0.00 \text{ , } \lambda_{\phi}^{\text{HE}} = -0.50 \text{ , } \lambda_{\theta}^{\text{CS}} = 0.00 \text{ , } \lambda_{\phi}^{\text{CS}} = -0.50$$

The result of the test is shown in Figure D.1: the values of  $\lambda_{\theta}$  and  $\lambda_{\phi}$  in the two reference frames are plotted as a function of the iteration number without their statistical error (negligible given the very high number of  $J/\psi$  used for the test). Open points refer to TEST 1, while full points concern TEST 2. The outcome of the check is that the result of the iterative procedure doesn't depend on the starting point and the correct value is reached in at most 3 iterations.

Another very important test to be performed to check the iterative procedure consists in following a quite different correction strategy. As discussed in Section 4.5, the final result of the iterative procedure is reached when the outcome of the correction gives the same parameters injected in the MC used to perform the correction. In order to find these values, an alternative way can be followed. Supposing, as an example, to be interested in studying the first  $p_t$  bin in the helicity frame, the procedure is the following:

1. the  $\lambda_{\theta}^{\text{CS}}$  and  $\lambda_{\phi}^{\text{CS}}$  inputs in the MC are fixed to those found after the last iteration of the default approach: this is done in order to disentangle the check for the two reference frames. These values can be labelled as  $\lambda_{\theta}^{\text{CS},fix}$  and  $\lambda_{\phi}^{\text{CS},fix}$ ;
2. the  $[\lambda_{\theta}^{\text{HE}}, \lambda_{\phi}^{\text{HE}}]$  space is divided in  $20 \times 20$  bins in the full range of variation  $[-1,1]$ ;
3. for each bin  $i$  previously identified, a Monte Carlo sample with the angular input  $[\lambda_{\theta,i}^{\text{HE},in}, \lambda_{\phi,i}^{\text{HE},in}, \lambda_{\theta}^{\text{CS},fix}, \lambda_{\phi}^{\text{CS},fix}]$  ( $\lambda_{\theta,i}^{\text{HE},in}$  and  $\lambda_{\phi,i}^{\text{HE},in}$  are the central values of the bin  $i$ ) is produced weighting the unpolarized MC (see Chapter 4 Section 4.5). This is done only in case the condition  $|\lambda_{\phi,i}^{\text{HE},in}| \leq 0.5 \cdot (1 + \lambda_{\theta,i}^{\text{HE},in})$  is satisfied, i.e. if the input couple represents a kinematically allowed angular configuration (see Chapter 2 Section 2.4). With this MC the correction of the data spectrum is performed, finding  $\lambda_{\theta,i}^{\text{HE},out}$  and  $\lambda_{\phi,i}^{\text{HE},out}$ ;

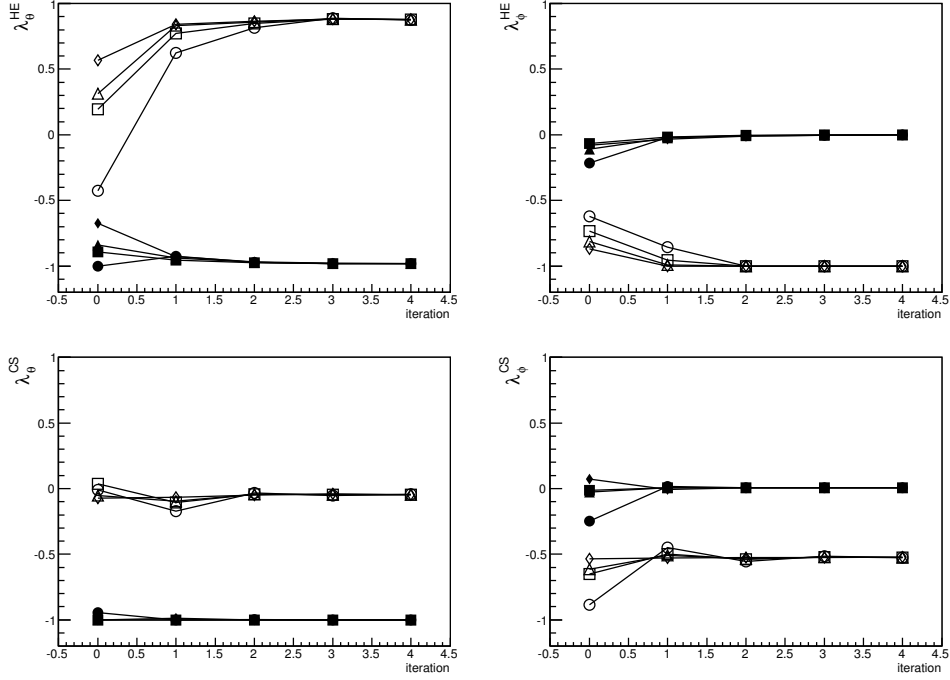


Figure D.1: Check on the iterative procedure. Open symbols correspond to TEST 1, while full markers to TEST 2. Circles, squares, triangles and rhombes refer to the different starting points of the iterative procedure: START 1, START 2, START 3 and START 4 respectively (see the text for more details).

4. a 2-dimensional histogram is produced, where the value  $|\Delta\lambda_\theta| = |\lambda_{\theta,i}^{HE,out} - \lambda_{\theta,i}^{HE,in}|$  is plotted as a function of  $\lambda_{\theta,i}^{HE,in}$  and  $\lambda_{\phi,i}^{HE,in}$ . The same thing is done for the  $\phi$  variable. An example of these two plots is shown in Figure D.2(a) and (b): they identify two minima regions (one for each parameter) for the difference between the input and the output. In order to find the final values, the intersection between the two minima regions has to be found: this is shown in Figure D.3, where the quantity  $|\Delta\lambda_\theta| + |\Delta\lambda_\phi|$  is plotted as a function of  $\lambda_{\theta,i}^{HE,in}$  and  $\lambda_{\phi,i}^{HE,in}$  for all the  $p_t$  bins in both the frames.

The results of this alternative procedure were compared with those obtained with the default approach (red crosses in Figure D.3) and the outcome is that there is a perfect agreement between the two for all the  $p_t$  bins and in the two reference frames.

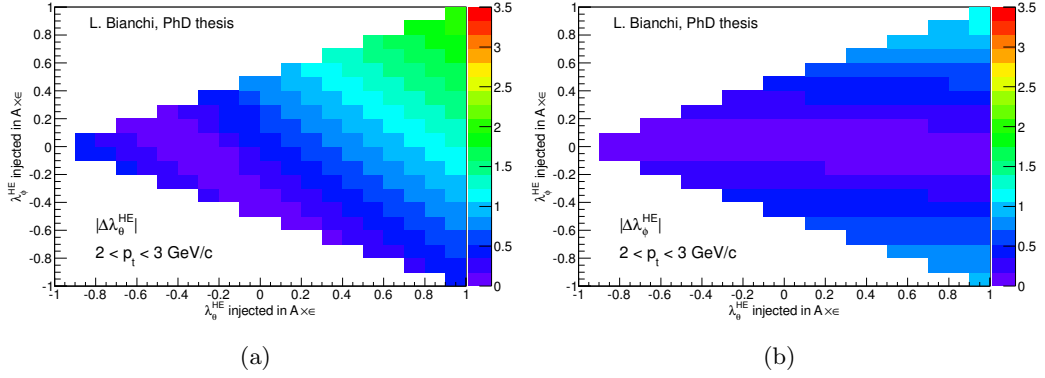


Figure D.2: Test on the iterative procedure:  $|\Delta\lambda_\theta| = |\lambda_{\theta,i}^{\text{HE},out} - \lambda_{\theta,i}^{\text{HE},in}|$  (a) and  $|\Delta\lambda_\theta| = |\lambda_{\theta,i}^{\text{HE},out} - \lambda_{\theta,i}^{\text{HE},in}|$  (b) as a function of the  $[\lambda_\theta^{\text{HE}}, \lambda_\phi^{\text{HE}}]$  input in the MC for the  $2 < p_t < 3 \text{ GeV}/c$  bin.

### D.0.2 Check on the fit to the corrected spectra

The fits to the corrected spectra were performed in a simultaneous way for the two reference frames (see Chapter 4 Section 4.6), imposing the invariance of the quantity  $\mathcal{F}$  in order to further constraint the fit and to reduce the statistical errors in the results. It is nevertheless interesting to try to perform the fits separately for the two frames without the constraint  $\mathcal{F}$  in order to understand if the condition alters the final results. For this reason all the correction procedure was re-performed treating the four spectra separately and fitting them with the shapes in Eq. 4.2 and 4.3. The result of this check can be found in Figure D.4, where the comparison between the reference results (black points) and the results obtained with the separate fit (red points) is shown.

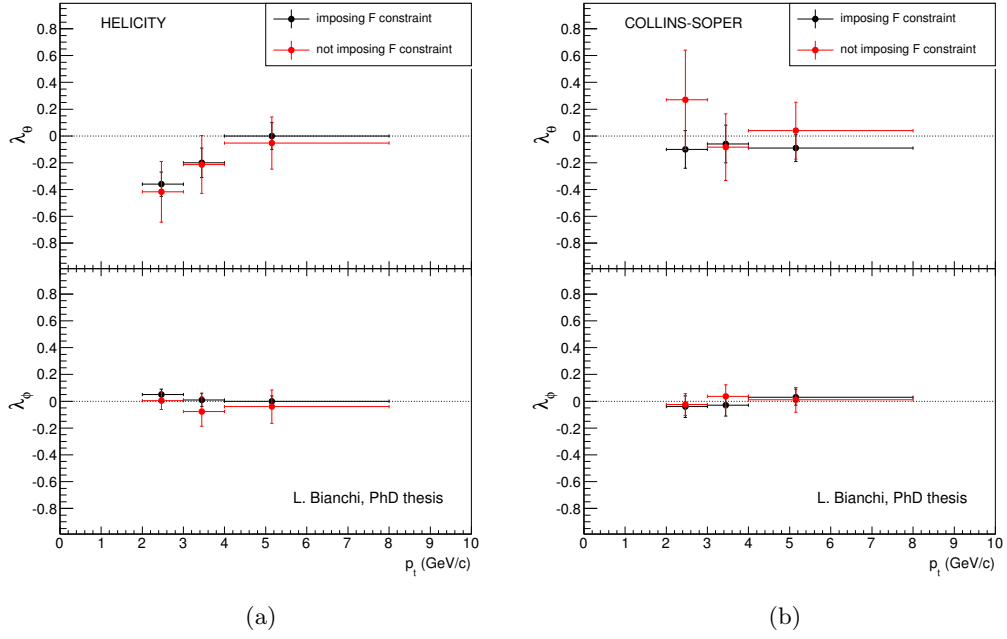


Figure D.4:  $\lambda_\theta$  and  $\lambda_\phi$  parameters, in the helicity (a) and Collins-Soper (b) reference frames, estimated with the default approach (black points) and without asking the invariance of the quantity  $\mathcal{F}$  (red points). Only statistical errors are plotted.

The agreement between the two techniques is good, re-insuring on the goodness of the default procedure.



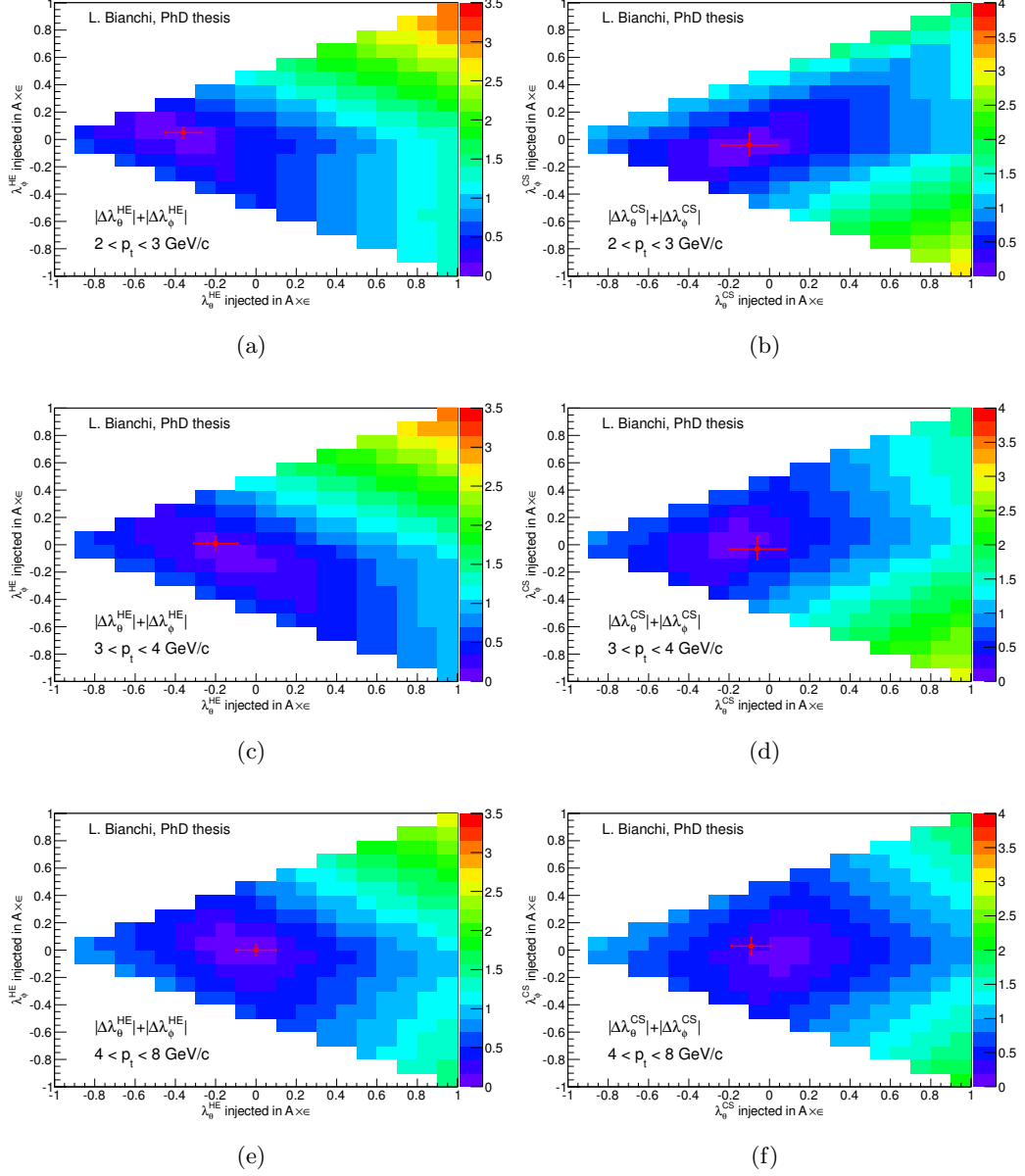


Figure D.3: Test on the iterative procedure:  $|\Delta\lambda_\theta| + |\Delta\lambda_\phi|$  as a function of the  $[\lambda_\theta, \lambda_\phi]$  input in the MC for the helicity (a,c,e) and Collins-Soper (b,d,f) reference frames and for the three considered  $p_t$  bins. Red crosses correspond to the polarization parameters measured with the default approach (only the statistical error is shown).

# Acknowledgments

This work was made possible thanks to the help, advice and presence of many people. Among them I want to explicitly acknowledge...

... Enrico Scomparin and Roberta Arnaldi who helped and supported me since I was an undergraduate and who supervised my thesis work. Their patience in answering all my questions has been invaluable and it deserves my deepest gratitude. At the same time I'd like to thank Ermanno Vercellin for the thesis direction in Torino and for his help in decrypting all the meaningless rules for the co-tutorship signature.

... Cynthia Hadjidakis for the supervision of my thesis work in Orsay and for her kindness in introducing me in the research group at the IPNO. Together with her, I also want to thank Bruno Espagnon, my thesis director in Orsay, for his help in dealing with the sprawling bureaucracy and for reading my thesis carefully.

... Federico Antinori, François Vazeille and Patrick Robbe because they read my thesis and took active part to the defence with interesting questions and suggestions.

... the ALICE groups in Torino and Orsay, which made me feel as part of something and which allowed me to attend many schools, conferences and workshops all over the world. A special thought to Anna Piccotti, who recently left us unexpectedly: we will miss her humble competence for long.

... all the PhD students I had the chance to meet in these three years: clever people inclined to talk about stupid things, and for this last reason I want to thank them.

... my friends, my girlfriend and my parents for many important reasons... and because they suffer me... even if I am a physicist!

## Acknowledgments

---

# List of Figures

1.1	First observations of the $J/\psi$ peak. . . . .	6
1.2	$R$ ratio as of July 1974 . . . . .	7
1.3	ATLAS' discovery of the $\chi_b(3P)$ . . . . .	11
1.4	Charmonium (a) and Bottomonium (b) spectra . . . . .	13
1.5	Lattice calculation of bottomonium spectrum . . . . .	17
1.6	Feynman diagrams for $J/\psi$ hadro- and photo-(lepto-)production . . . . .	19
1.7	Tevatron results on $J/\psi, \psi(2S)$ , $J/\psi$ from $\chi_c$ and $\Upsilon$ . . . . .	25
1.8	CDF results compared with CSM at NLO and NNLO* . . . . .	26
1.9	PHENIX result on $J/\psi$ cross section . . . . .	28
1.10	DELPHI result on $J/\psi$ cross section . . . . .	29
1.11	H1 results on cross section for photo-produced $J/\psi$ . . . . .	31
1.12	ALICE results on $J/\psi$ cross section . . . . .	32
1.13	LHC + CDF experiments results on $J/\psi \leftarrow B$ . . . . .	32
1.14	ATLAS results on $J/\psi$ cross section . . . . .	34
1.15	CMS: quarkonia detection performance . . . . .	34
1.16	CMS results on $J/\psi$ , $\psi(2S)$ and $\Upsilon$ cross sections . . . . .	35
1.17	$J/\psi$ $p_t$ differential cross section from LHCb . . . . .	37
1.18	$J/\psi$ from B-meson measured by LHCb . . . . .	38
1.19	Global NLO NRQCD fit to LHC data . . . . .	39
1.20	Global NLO NRQCD fit to non-LHC data . . . . .	40
1.21	Charmonium (a) and bottomonium (b) spectral functions . . . . .	43
1.22	$J/\psi$ suppression pattern before LHC . . . . .	45
1.23	LHC first results on quarkonium suppression . . . . .	47
2.1	Schematic picture of quarkonium decay into two leptons . . . . .	52
2.2	Reference frame definitions . . . . .	57
2.3	Kinematically allowed region for the $\lambda_\theta$ , $\lambda_\phi$ and $\lambda_{\theta\phi}$ parameters . . . . .	58

## LIST OF FIGURES

---

2.4	$\theta$ and $\phi$ angles definition . . . . .	61
2.5	Polarization parameter $\alpha = \lambda_\theta$ as measured by CDF . . . . .	63
2.6	Polarization parameter $\alpha = \lambda_\theta$ as measured by CDF and D0 . . . . .	64
2.7	Polarization parameter $\alpha = \lambda_\theta$ as measured by PHENIX . . . . .	65
2.8	$J/\psi$ polarization measured by ZEUS and H1 . . . . .	66
2.9	$\alpha (= \lambda_\theta)$ parameter measured by BaBar . . . . .	68
2.10	$\alpha (= \lambda_\theta)$ parameter measured by E866 . . . . .	69
2.11	Polarization parameters as measure by the HERA-B collaboration . . . .	70
2.12	$\lambda_\theta$ and $\lambda_\phi$ from ZEUS and H1 compared with NLO CSM and NRQCD .	71
3.1	Schematic view of the CERN accelerator complex. . . . .	74
3.2	The ALICE muon spectrometer layout. . . . .	82
3.3	Layout of the front absorber. . . . .	83
3.4	Tracking chambers of the muon spectrometer . . . . .	85
3.5	Schematic view of a Resistive Plate Chamber. . . . .	86
3.6	The muon spectrometer trigger principle . . . . .	87
3.7	Schematic view of the AliRoot framework. . . . .	90
3.8	Data processing framework. . . . .	91
4.1	$A \times \epsilon$ plot for the helicity frame . . . . .	96
4.2	Physics Selection: correlation SPD clusters - SPD tracklets . . . . .	99
4.3	Integrated invariant mass spectrum in the range $2 < p_t < 8$ GeV/ $c$ . . .	100
4.4	Invariant mass in the five bins of $\cos\theta_{HE}$ for $2 < p_t < 3$ GeV/ $c$ . . . .	102
4.5	$p_t$ and $y$ parametrizations in the MC . . . . .	104
4.6	Efficiency of the bending plane of chamber 12 . . . . .	104
4.7	Two dimensional $A \times \epsilon$ plots from realistic MC simulation . . . . .	106
4.8	$\lambda_\theta$ parameter as a function of the iteration number . . . . .	108
4.9	Fit to the corrected spectra for the first $p_t$ bin . . . . .	109
4.10	$p_t$ and $y$ inputs in the MC for systematics determination . . . . .	111
4.11	Final results on $\lambda_\theta$ and $\lambda_\phi$ . . . . .	113
4.12	Final results on $\lambda_\theta$ and $\lambda_\phi$ compared with NLO CSM and NRQCD . . . .	114
4.13	Iterative procedure extended to $\lambda_{\theta\phi}$ . . . . .	115
4.14	$\tilde{\phi}$ corrected spectra with zero-polynomial fit . . . . .	117
4.15	$p_t$ cross section for prompt and non-prompt $J/\psi$ by LHCb . . . . .	118
4.16	Difference between inclusive and prompt $\lambda_\theta$ . . . . .	120

## LIST OF FIGURES

---

B.1	Invariant mass of opposite sign muon pairs in the five bins of $ \cos\theta_{\text{HE}} $ (a) and in the four bins of $ \phi_{\text{HE}} $ (b) for $2 < p_t < 3$ GeV/c. The fit to each spectrum is plotted as a blue line. . . . .	126
B.2	Invariant mass of opposite sign muon pairs in the five bins of $ \cos\theta_{\text{CS}} $ (a) and in the four bins of $ \phi_{\text{CS}} $ (b) for $2 < p_t < 3$ GeV/c. The fit to each spectrum is plotted as a blue line. . . . .	127
B.3	Invariant mass of opposite sign muon pairs in the five bins of $ \cos\theta_{\text{HE}} $ (a) and in the four bins of $ \phi_{\text{HE}} $ (b) for $3 < p_t < 4$ GeV/c. The fit to each spectrum is plotted as a blue line. . . . .	128
B.4	Invariant mass of opposite sign muon pairs in the five bins of $ \cos\theta_{\text{CS}} $ (a) and in the four bins of $ \phi_{\text{CS}} $ (b) for $3 < p_t < 4$ GeV/c. The fit to each spectrum is plotted as a blue line. . . . .	129
B.5	Invariant mass of opposite sign muon pairs in the five bins of $ \cos\theta_{\text{HE}} $ (a) and in the four bins of $ \phi_{\text{HE}} $ (b) for $4 < p_t < 8$ GeV/c. The fit to each spectrum is plotted as a blue line. . . . .	130
B.6	Invariant mass of opposite sign muon pairs in the five bins of $ \cos\theta_{\text{CS}} $ (a) and in the four bins of $ \phi_{\text{CS}} $ (b) for $4 < p_t < 8$ GeV/c. The fit to each spectrum is plotted as a blue line. . . . .	131
C.1	Fit to the corrected spectra: $2 < p_t < 3$ GeV/c. . . . .	133
C.2	Fit to the corrected spectra: $3 < p_t < 4$ GeV/c. . . . .	134
C.3	Fit to the corrected spectra: $4 < p_t < 8$ GeV/c. . . . .	134
D.1	Check on the iterative procedure. Open symbols correspond to TEST 1, while full markers to TEST 2. Circles, squares, triangles and rhombes refer to the different starting points of the iterative procedure: START 1, START 2, START 3 and START 4 respectively (see the text for more details). . . . .	137
D.2	Test on the iterative procedure: $ \Delta\lambda_\theta  =  \lambda_{\theta,i}^{\text{HE},out} - \lambda_{\theta,i}^{\text{HE},in} $ (a) and $ \Delta\lambda_\theta  =  \lambda_{\theta,i}^{\text{HE},out} - \lambda_{\theta,i}^{\text{HE},in} $ (b) as a function of the $[\lambda_\theta^{\text{HE}}, \lambda_\phi^{\text{HE}}]$ input in the MC for the $2 < p_t < 3$ GeV/c bin. . . . .	138
D.4	$\lambda_\theta$ and $\lambda_\phi$ parameters, in the helicity (a) and Collins-Soper (b) reference frames, estimated with the default approach (black points) and without asking the invariance of the quantity $\mathcal{F}$ (red points). Only statistical errors are plotted. . . . .	139

## LIST OF FIGURES

---

D.3	Test on the iterative procedure: $ \Delta\lambda_\theta  +  \Delta\lambda_\phi $ as a function of the $[\lambda_\theta, \lambda_\phi]$ input in the MC for the helicity (a,c,e) and Collins-Soper (b,d,f) reference frames and for the three considered $p_t$ bins. Red crosses correspond to the polarization parameters measured with the default approach (only the statistical error is shown).	140
-----	---	-----

# List of Tables

1.1	Charmonia and bottomonia “conventional” states . . . . .	9
1.2	Unexpected states in the $c\bar{c}$ and $b\bar{b}$ regions . . . . .	10
1.3	Quarkonium dissociation temperatures in the screening theory framework. . . . .	43
4.1	Runs used for the analysis. . . . .	97
4.2	Summary of the systematic uncertainties on the $J/\psi$ polarization parameters estimation. . . . .	112
4.3	$\lambda_\theta$ and $\lambda_\phi$ parameters results in three $p_t$ bins and for the helicity (HE) and Collins-Soper (CS) reference frames. Statistical and systematical errors are quoted separately. . . . .	113
B.1	$\tilde{\chi}^2$ , S/B and $N_{J/\psi}$ from the fit to the invariant mass distributions of each bin in the kinematical variables. . . . .	125



## LIST OF TABLES

---

# Bibliography

- [1] J. Aubert *et al.* (E598 Collaboration). Experimental Observation of a Heavy Particle *J. Phys. Rev. Lett.*, 33:1404–1406, Dec 1974.
- [2] J. Augustin *et al.* (SLAC-SP-017 Collaboration). Discovery of a Narrow Resonance in  $e^+e^-$  Annihilation. *Phys. Rev. Lett.*, 33:1406–1408, Dec 1974.
- [3] C. Bacci *et al.* (ADONE Collaboration). Preliminary Result of Frascati (ADONE) on the Nature of a New 3.1-GeV Particle Produced in  $e^+e^-$  Annihilation. *Phys. Rev. Lett.*, 33:1408–1410, Dec 1974.
- [4] W. Braunschweig *et al.* . Observation of the two photon cascade  $3.7 \rightarrow 3.1 + \gamma\gamma$  via an intermediate state  $P_c$ . *Physics Letters B*, 57(4):407–412, 1975.
- [5] B. Richter.  $e^+e^- \rightarrow$  Hadrons. SLAC-PUB-1478, Plenary Session Report at XVII International Conference on High Energy Physics, London, Eng., Jul 1-10, 1974.
- [6] J. D. Bjorken and S. L. Glashow. Elementary Particles and SU(4). *Phys. Lett.*, 11:255–257, 1964.
- [7] S. L. Glashow, J. Iliopoulos, and L. Maiani. Weak Interactions with Lepton-Hadron Symmetry. *Phys. Rev. D*, 2:1285–1292, Oct 1970.
- [8] G. Goldhaber *et al.* . Observation in  $e^+e^-$  Annihilation of a Narrow State at 1865 MeV/ $c^2$  Decaying to  $K\pi$  and  $K\pi\pi\pi$ . *Phys. Rev. Lett.*, 37:255–259, Aug 1976.
- [9] B. Knapp *et al.* . Observation of a Narrow Antibaryon State at 2.26 GeV/ $c^2$ . *Phys. Rev. Lett.*, 37:882–885, Oct 1976.
- [10] M. L. Perl *et al.* . Evidence for Anomalous Lepton Production in  $e^+ - e^-$  Annihilation. *Phys. Rev. Lett.*, 35:1489–1492, Dec 1975.

- [11] S. W. Herb *et al.* . Observation of a Dimuon Resonance at 9.5 GeV in 400-GeV Proton-Nucleus Collisions. *Phys. Rev. Lett.*, 39:252–255, Aug 1977.
- [12] W. R. Innes *et al.* . Observation of Structure in the  $\Upsilon$  Region. *Phys. Rev. Lett.*, 39:1240–1242, Nov 1977.
- [13] K. Ueno *et al.* . Evidence for the  $\Upsilon''$  and a Search for New Narrow Resonances. *Phys. Rev. Lett.*, 42:486–489, Feb 1979.
- [14] C. Bebek *et al.* . Evidence for New-Flavor Production at the  $\Upsilon(4S)$ . *Phys. Rev. Lett.*, 46:84–87, Jan 1981.
- [15] M. Basile *et al.* . Evidence for a new particle with naked 'beauty' and for its associated production in high energy pp interactions. *Nuovo Cim. Lett.*, 31:97, 1981.
- [16] F. Abe *et al.* . Evidence for top quark production in  $p\bar{p}$  collisions at  $\sqrt{s}=1.8$  TeV. *Phys. Rev. D*, 50:2966–3026, Sep 1994.
- [17] S.-K. Choi *et al.* . Observation of a Narrow Charmoniumlike State in Exclusive  $B^\pm \rightarrow K^\pm \pi^+ \pi^- J/\psi$  Decays. *Phys. Rev. Lett.*, 91:262001, Dec 2003.
- [18] N. Brambilla *et al.* . Heavy Quarkonium Physics. arXiv:hep-ph/0412158v2.
- [19] G. Aad *et al.* (ATLAS Collaboration). Observation of a new  $\chi_b$  state in radiative transitions to  $\Upsilon(1S)$  and  $\Upsilon(2S)$  at ATLAS. *submitted to PRL*, 2011.
- [20] W.E. Caswell and G.P. Lepage. Effective lagrangians for bound state problems in QED, QCD, and other field theories. *Physics Letters B*, 167(4):437–442, 1986.
- [21] Geoffrey T. Bodwin, Eric Braaten, and G. Peter Lepage. Rigorous QCD analysis of inclusive annihilation and production of heavy quarkonium. *Phys. Rev. D*, 51:1125–1171, Feb 1995.
- [22] A. Pineda and J. Soto. Effective Field Theory for Ultrasoft Momenta in NRQCD and NRQED. arXiv:hep-ph/9707481v2.
- [23] J. Soto A. Vairo N. Brambilla, A. Pineda. Potential NRQCD: an effective theory for heavy quarkonium. arXiv:hep-ph/9907240v2.
- [24] Stefan Meinel. Bottomonium spectrum from lattice QCD with  $2 + 1$  flavors of domain wall fermions. *Phys. Rev. D*, 79:094501, May 2009.

## BIBLIOGRAPHY

---

- [25] M. B. Einhorn and S. D. Ellis. Hadronic production of the new resonances: Probing gluon distributions. *Phys. Rev. D*, 12:2007–2014, Oct 1975.
- [26] S. D. Ellis, Martin B. Einhorn, and C. Quigg. Comment on Hadronic Production of Psions. *Phys. Rev. Lett.*, 36:1263–1266, May 1976.
- [27] C. E. Carlson and R. Suaya. Hadronic production of the  $\psi/J$  meson. *Phys. Rev. D*, 14:3115–3121, Dec 1976.
- [28] P. Artoisenet, J.P. Lansberg, and F. Maltoni. Hadroproduction of  $\Upsilon$  in association with a heavy-quark pair. *Physics Letters B*, 653(1):60–66, 2007.
- [29] J. Campbell, F. Maltoni, and F. Tramontano. QCD Corrections to  $J/\psi$  and  $\Upsilon$  Production at Hadron Colliders. *Phys. Rev. Lett.*, 98:252002, Jun 2007.
- [30] P. Artoisenet, J. Campbell, J. P. Lansberg, F. Maltoni, and F. Tramontano.  $\Upsilon$  Production at Fermilab Tevatron and LHC Energies. *Phys. Rev. Lett.*, 101:152001, Oct 2008.
- [31] H. Fritzsch. Producing heavy quark flavors in hadronic collisions - A test of quantum chromodynamics. *Physics Letters B*, 67(2):217–221, 1977.
- [32] N. Brambilla *et al.* Heavy quarkonium: progress, puzzles, and opportunities. *The European Physical Journal C - Particles and Fields*, 71:1–178, 2011. 10.1140/epjc/s10052-010-1534-9.
- [33] Geoffrey T. Bodwin, Xavier Garcia i Tormo, and Jungil Lee. Factorization Theorems for Exclusive Heavy-Quarkonium Production. *Phys. Rev. Lett.*, 101:102002, Sep 2008.
- [34] Geoffrey T. Bodwin, Xavier Garcia i Tormo, and Jungil Lee. Factorization in exclusive quarkonium production. *Phys. Rev. D*, 81:114014, Jun 2010.
- [35] A. D. Martin E. W. N. Glover and W. J. Stirling. *Z. phys. c* 38 (1988) 473.
- [36] Peter Cho and Adam K. Leibovich. Color-octet quarkonia production. *Phys. Rev. D*, 53:150–162, Jan 1996.
- [37] Peter Cho and Adam K. Leibovich. Color-octet quarkonia production. II. *Phys. Rev. D*, 53:6203–6217, Jun 1996.

- [38] J. Lansberg. On the mechanisms of heavy-quarkonium hadroproduction. *The European Physical Journal C - Particles and Fields*, 61:693–703, 2009. 10.1140/epjc/s10052-008-0826-9.
- [39] T. Aaltonen *et al.* (CDF Collaboration). Production of  $\psi(2S)$  mesons in  $p\bar{p}$  collisions at 1.96 TeV. *Phys. Rev. D*, 80:031103, Aug 2009.
- [40] D. Acosta *et al.* (CDF Collaboration).  $\Upsilon$  Production and Polarization in  $p\bar{p}$  Collisions at  $\sqrt{s} = 1.8\text{TeV}$ . *Phys. Rev. Lett.*, 88:161802, Apr 2002.
- [41] F. Abe *et al.* (CDF Collaboration). Production of  $J/\psi$  Mesons from  $\chi_c$  Meson Decays in  $p\bar{p}$  Collisions at  $\sqrt{s} = 1.8\text{TeV}$ . *Phys. Rev. Lett.*, 79:578–583, Jul 1997.
- [42] T. Affolder *et al.* (CDF Collaboration). Production of  $\chi_{c1}$  and  $\chi_{c2}$  in  $p\bar{p}$  Collisions at  $\sqrt{s} = 1.8\text{TeV}$ . *Phys. Rev. Lett.*, 86:3963–3968, Apr 2001.
- [43] A. Adare *et al.* . Transverse momentum dependence of  $J/\psi$  polarization at midrapidity in  $p + p$  collisions at  $\sqrt{s} = 200\text{GeV}$ . *Phys. Rev. D*, 82:012001, Jul 2010.
- [44] B. I. Abelev *et al.* .  $J/\psi$  production at high transverse momenta in  $p + p$  and  $Cu + Cu$  collisions at  $\sqrt{s_{NN}} = 200$  GeV. *Phys. Rev. C*, 80:041902, Oct 2009.
- [45] Gouranga C. Nayak, Ming X. Liu, and Fred Cooper. Color octet contribution to high  $p_t$   $J/\psi$  production in  $pp$  collisions at  $\sqrt{s} = 500$  and 200 GeV at BNL RHIC. *Phys. Rev. D*, 68:034003, Aug 2003.
- [46] Hee Sok Chung, Chaehyun Yu, Seyong Kim, and Jungil Lee. Polarization of prompt  $J/\psi$  in proton-proton collisions at RHIC. *Phys. Rev. D*, 81:014020, Jan 2010.
- [47] J.P. Lansberg. QCD corrections to polarisation in pp collisions at RHIC. *Physics Letters B*, 695(1–4):149–156, 2011.
- [48] J. Abdallah *et al.* (DELPHI Collaboration). Study of inclusive  $J/\psi$  production in two-photon collisions at LEP II with the DELPHI detector. *Physics Letters B*, 565(0):76–86, 2003.
- [49] Michael Klasen, Bernd A. Kniehl, Luminita N. Mihaila, and Matthias Steinhauser. Evidence for the Color-Octet Mechanism from CERN LEP2  $\gamma\gamma \rightarrow J/\psi + X$  Data. *Phys. Rev. Lett.*, 89:032001, Jun 2002.

- [50] K. Abe *et al.* Observation of Double  $c\bar{c}$  Production in  $e^+e^-$  Annihilation at  $\sqrt{s} \approx 10.6$  GeV. *Phys. Rev. Lett.*, 89:142001, Sep 2002.
- [51] Kui-Yong Liu, Zhi-Guo He, and Kuang-Ta Chao. Inclusive charmonium production via double  $c\bar{c}$  in  $e^+e^-$  annihilation. *Phys. Rev. D*, 69:094027, May 2004.
- [52] K. Hagiwara, E. Kou, Z.-H. Lin, C.-F. Qiao, and G.-H. Zhu. Inclusive  $J/\psi$  production at  $e^+e^-$  colliders. *Phys. Rev. D*, 70:034013, Aug 2004.
- [53] F. Aaron *et al.* (H1 Collaboration). Inelastic production of  $J/\psi$  mesons in photoproduction and deep inelastic scattering at HERA. *The European Physical Journal C - Particles and Fields*, 68:401–420, 2010. 10.1140/epjc/s10052-010-1376-5.
- [54] P. Artoisenet, J. Campbell, F. Maltoni, and F. Tramontano.  $J/\psi$  Production at HERA. *Phys. Rev. Lett.*, 102:142001, Apr 2009.
- [55] Mathias Butenschön and Bernd A. Kniehl. Complete Next-to-Leading-Order Corrections to  $J/\psi$  Photoproduction in Nonrelativistic Quantum Chromodynamics. *Phys. Rev. Lett.*, 104:072001, Feb 2010.
- [56] K. Aamodt *et al.* (ALICE Collaboration). The ALICE experiment at the CERN LHC. *JINST*, 3:S08002, 2008.
- [57] G. Aad *et al.* (ATLAS Collaboration). The ATLAS Experiment at the CERN Large Hadron Collider. *JINST*, 3:S08003, 2008.
- [58] S. Chatrchyan *et al.* (CMS Collaboration). The CMS experiment at the CERN LHC. *JINST*, 3:S08004, 2008.
- [59] A. Augusto Alves Jr *et al.* (LHCb Collaboration). The LHCb Detector at the LHC. *JINST*, 3:S08005, 2008.
- [60] K. Aamodt *et al.* (ALICE collaboration). Rapidity and transverse momentum dependence of inclusive  $J/\psi$  production in pp collisions at  $\sqrt{s} = 7$  TeV. *Physics Letters B*, 704(5):442–455, 2011.
- [61] F. Fionda. *Studio della produzione di  $J/\psi$  in collisioni protone-protone a  $\sqrt{s} = 7$  TeV con l'apparato ALICE*. PhD thesis, Università di Bari, 2012.
- [62] B. Abelev *et al.* (ALICE Collaboration).  $J/\psi$  Polarization in pp Collisions at  $\sqrt{s} = 7$  TeV. *Phys. Rev. Lett.*, 108:082001, Feb 2012.

- [63] G. Aad *et al.* (ATLAS Collaboration). Measurement of the differential cross-sections of inclusive, prompt and non-prompt  $J/\psi$  production in proton–proton collisions at  $\sqrt{s} = 7$  TeV. *Nuclear Physics B*, 850(3):387 – 444, 2011.
- [64] G. Aad *et al.* (ATLAS Collaboration). Measurement of the  $\Upsilon(1S)$  production cross-section in pp collisions at  $\sqrt{s} = 7$  TeV in ATLAS. *Physics Letters B*, 705(1–2):9 – 27, 2011.
- [65] A.D. Frawley, T. Ullrich, and R. Vogt. Heavy flavor in heavy-ion collisions at RHIC and RHIC II. *Physics Reports*, 462(4–6):125 – 175, 2008.
- [66] S. Chatrchyan *et al.* (CMS Collaboration).  $J/\psi$  and  $\psi(2S)$  production in pp collisions at  $\sqrt{s} = 7$  TeV. 2011. arXiv:1111.1557.
- [67] V. Khachatryan *et al.* (CMS Collaboration).  $\Upsilon$  production cross section in  $pp$  collisions at  $\sqrt{s} = 7\text{TeV}$ . *Phys. Rev. D*, 83:112004, Jun 2011.
- [68] R. Aaij *et al.* (LHCb collaboration). Measurement of  $J/\psi$  production in pp collisions at  $\sqrt{s} = 7$  TeV. *The European Physical Journal C - Particles and Fields*, 71:1–17, 2011. 10.1140/epjc/s10052-011-1645-y.
- [69] P. Artoisenet. Quarkonium production at the Tevatron and the LHC. 2010. PoS(ICHEP 2010)192.
- [70] Mathias Butenschön and Bernd A. Kniehl. Reconciling  $J/\psi$  Production at HERA, RHIC, Tevatron, and LHC with Nonrelativistic QCD Factorization at Next-to-Leading Order. *Phys. Rev. Lett.*, 106:022003, Jan 2011.
- [71] Yan-Qing Ma, Kai Wang, and Kuang-Ta Chao.  $J/\psi(\psi(2S))$  Production at the Tevatron and LHC at  $O(\alpha_s^4 v^4)$  in Nonrelativistic QCD. *Phys. Rev. Lett.*, 106:042002, Jan 2011.
- [72] R. Aaij *et al.* (LHCb Collaboration). Observation of  $J/\psi$ -pair production in pp collisions at  $\sqrt{s} = 7$  TeV. *Physics Letters B*, 707(1):52 – 59, 2012.
- [73] Mathias Butenschön and Bernd A. Kniehl.  $J/\psi$  production in NRQCD: A global analysis of yield and polarization. 2012. arXiv:1201.3862v1.
- [74] F. Gelis. Some aspects of ultra-relativistic heavy ion collisions. 2007. arXiv:0711.4947.

- [75] C.Y. Wong. *Introduction to high-energy heavy-ion collisions*. World Scientific, 1994.
- [76] T. Matsui and H. Satz.  $J/\psi$  suppression by quark-gluon plasma formation. *Phys. Lett. B*, 178:416–422, 1986.
- [77] Helmut Satz. Charm and Beauty in a Hot Environment. 2006. arXiv:hep-ph/0602245.
- [78] C. Miao, A. Mocsy, and P. Petreczky. Quarkonium spectral functions with complex potential, 2010.
- [79] B. Alessandro *et al.* (NA50 Collaboration). A new measurement of  $J/\psi$  suppression in Pb-Pb collisions at 158 GeV per nucleon. *The European Physical Journal C - Particles and Fields*, 39:335–345, 2005. 10.1140/epjc/s2004-02107-9.
- [80] R. Arnaldi *et al.* .  $J/\psi$  Production in Indium-Indium Collisions at 158 GeV/Nucleon. *Phys. Rev. Lett.*, 99:132302, Sep 2007.
- [81] A. Adare *et al.* .  $J/\psi$  Production versus Centrality, Transverse Momentum, and Rapidity in AuAu Collisions at  $\sqrt{s_{NN}} = 200$  GeV. *Phys. Rev. Lett.*, 98:232301, Jun 2007.
- [82] P. Pillot (for the ALICE Collaboration).  $J/\psi$  production at forward rapidity in Pb-Pb collisions at  $\sqrt{s_{NN}} = 2.76$  TeV, measured with the ALICE detector. 2011. arXiv:1108.3795v1.
- [83] G. Aad *et al.* (ATLAS Collaboration). Measurement of the centrality dependence of  $J/\psi$  yields and observation of  $Z$  production in lead-lead collisions with the ATLAS detector at the LHC. *Physics Letters B*, 697(4):294 – 312, 2011.
- [84] S. Chatrchyan *et al.* (CMS Collaboration). Suppression of non-prompt  $J/\psi$ , prompt  $J/\psi$ , and  $\Upsilon(1S)$  in PbPb collisions at  $\sqrt{s_{NN}} = 2.76$  TeV. 2012. arXiv:1201.5069.
- [85] João Seixas Hermine Wöhri Pietro Faccioli, Carlos Lourenço. Towards the experimental clarification of quarkonium polarization. *The European Physical Journal C - Particles and Fields*, 69:657–673, 2010. 10.1140/epjc/s10052-010-1420-5.
- [86] Pietro Faccioli, Carlos Lourenço, João Seixas, and Hermine K. Wöhri. Model-independent constraints on the shape parameters of dilepton angular distributions. *Phys. Rev. D*, 83:056008, Mar 2011.



- [87] V. Devanathan. *Angular Momentum Techniques in Quantum Mechanics*. Springer, 1999.
- [88] John C. Collins and Davison E. Soper. Angular distribution of dileptons in high-energy hadron collisions. *Phys. Rev. D*, 16:2219–2225, Oct 1977.
- [89] K. Gottfried and J. Jackson. On the connection between production mechanism and decay of resonances at high energies. *Il Nuovo Cimento (1955-1965)*, 33:309–330, 1964. 10.1007/BF02750195.
- [90] T. Affolder *et al.* . Measurement of  $J/\psi$  and  $\psi(2S)$  Polarization in  $p\bar{p}$  Collisions at  $\sqrt{s} = 1.8\text{TeV}$ . *Phys. Rev. Lett.*, 85:2886–2891, Oct 2000.
- [91] A. Abulencia *et al.* Polarizations of  $J/\psi$  and  $\psi(2S)$  Mesons Produced in  $p\bar{p}$  Collisions at  $\sqrt{s} = 1.96\text{TeV}$ . *Phys. Rev. Lett.*, 99:132001, Sep 2007.
- [92] Eric Braaten, Bernd A. Kniehl, and Jungil Lee. Polarization of prompt  $J/\psi$  at the Fermilab Tevatron. *Phys. Rev. D*, 62:094005, Sep 2000.
- [93] S. P. Baranov. Highlights from the  $k_T$ -factorization approach on the quarkonium production puzzles. *Phys. Rev. D*, 66:114003, Dec 2002.
- [94] J. P. Lansberg.  $J/\psi$  production at  $\sqrt{s} = 1.96$  and 7 TeV: Color-Singlet Model, NNLO\* and polarisation. 2011. arXiv:1107.0292.
- [95] V. M. Abazov *et al.* . Measurement of the Polarization of the  $\Upsilon(1S)$  and  $\Upsilon(2S)$  States in  $p\bar{p}$  Collisions at  $\sqrt{s} = 1.96$  TeV. *Phys. Rev. Lett.*, 101:182004, Oct 2008.
- [96] Eric Braaten and Jungil Lee. Polarization of  $\Upsilon(nS)$  at the Fermilab Tevatron. *Phys. Rev. D*, 63:071501, Mar 2001.
- [97] S. Chekanov *et al.* (ZEUS Collaboration). Measurement of  $J/\psi$  helicity distributions in inelastic photoproduction at HERA. *JHEP*, 12, 2009.
- [98] M. Beneke, M. Krämer, and M. Vanttinen. Inelastic photoproduction of polarized  $J/\psi$ . *Phys. Rev. D*, 57:4258–4274, Apr 1998.
- [99] B. Aubert *et al.* (BaBar collaboration). Study of inclusive production of charmonium mesons in B decays. *Phys. Rev. D*, 67:032002, Feb 2003.
- [100] Sean Fleming, Oscar F. Hernández, Ivan Maksymyk, and Hélène Nadeau. NRQCD matrix elements in polarization of  $J/\psi$  produced from  $b$  decay. *Phys. Rev. D*, 55:4098–4104, Apr 1997.

## BIBLIOGRAPHY

---

- [101] K. Abe *et al.* . Production of Prompt Charmonia in  $e^+e^-$  Annihilation at  $\sqrt{s} \approx 10.6\text{GeV}$ . *Phys. Rev. Lett.*, 88:052001, Jan 2002.
- [102] J. Lee H. S. Song S. Baek, P. Ko. Polarized  $J/\psi$  production at CLEO. 1998. arXiv:hep-ph/9804455v1.
- [103] Eric Braaten and Yu-Qi Chen. Signature for Color-Octet Production of  $J/\psi$  in  $e^+e^-$  Annihilation. *Phys. Rev. Lett.*, 76:730–733, Jan 1996.
- [104] T. H. Chang *et al.* .  $J/\psi$  Polarization in 800-GeV p-Cu Interactions. *Phys. Rev. Lett.*, 91:211801, Nov 2003.
- [105] C. N. Brown *et al.* . Observation of Polarization in Bottomonium Production at  $\sqrt{s} = 38.8\text{ GeV}$ . *Phys. Rev. Lett.*, 86:2529–2532, Mar 2001.
- [106] R. Arnaldi (for the NA60 Collaboration).  $J/\psi$  production in p-A and A-A collisions at fixed target experiments. *Nuclear Physics A*, 830(1–4):345c – 352c, 2009.
- [107] I. Abt *et al.* (HERA-B Collaboration). Angular distributions of leptons from  $J/\psi$ 's produced in 920 GeV fixed-target proton-nucleus collisions. *The European Physical Journal C - Particles and Fields*, 60:517–524, 2009. 10.1140/epjc/s10052-009-0957-7.
- [108] B. A. Kniehl M. Butenschoen. Probing nonrelativistic QCD factorization in polarized  $J/\psi$  photoproduction at next-to-leading order. 2011. arXiv:1109.1476v2.
- [109] L. Evans and P. Bryant. LHC Machine. *JINST*, 3:S08001, 2008.
- [110] O. Adriani *et al.* (LHCf Collaboration). The LHCf detector at the CERN Large Hadron Collider . *JINST*, 3:S08006, 2008.
- [111] G. Anelli *et al.* (TOTEM Collaboration). The TOTEM Experiment at the CERN Large Hadron Collider. *JINST*, 3:S08007, 2008.
- [112] <http://www.desy.de/blobel/wwwmille.html>.
- [113] <http://aliceinfo.cern.ch/Offline>.
- [114] Pietro Cortese, Federico Carminati, Christian Wolfgang Fabjan, Lodovico Riccati, and Hans de Groot. *ALICE computing: Technical Design Report*. Technical Design Report ALICE. CERN, Geneva, 2005. CERN-LHCC-2005-018.

## BIBLIOGRAPHY

---

- [115] <http://root.cern.ch>.
- [116] J.E. Gaiser. PhD thesis, 1982.
- [117] F. Bossu *et al.* . Phenomenological extrapolation of the inclusive  $J/\psi$  cross section to proton-proton collisions at 2.76 TeV and 5.5 TeV. arXiv:1103.2394.